Alma Mater Studiorum - Università di Bologna

Doctorate in Future earth, climate change, and societal challenges

cycle XXXV

Settore Concorsuale: 04/A4 - GEOFISICA

Settore Scientifico Disciplinare: GEO/12 - OCEANOGRAFIA E FISICA DELL'ATMOSFERA

Ship performance modelling for least-CO_2 emissions routes

Presentata da

Amal Salhi

Supervisore

Dr. Gianandrea Mannarini

Coordinatrice di Dottorato

Prof. Nadia Pinardi

Co-supervisore

Prof. Nadia Pinardi

October 25, 2022

Acknowledgements

I would like to express my deepest gratitude to my supervisor Dr. Gianandrea Mannarini not only for his scientific support, but also for being exemplary in terms of professionalism, hard work and perseverance.

I am extremely grateful to my co-supervisor Prof. Nadia Pinardi for this opportunity, for believing in me, and for her scientific advice.

I am also grateful to Prof. Giovanni Coppini the director of OPA division at CMCC for his continuous support, as well as to my colleagues.

Many thanks go to my friends Mounir, Nejm, Ivano, Ivan, and especially Aisha, Antonio and Giulia, for being a family for me in Lecce.

Finally, I would like to dedicate this thesis to my wonderful family: my parents Najwa and Monsef, my brother Khaled and my sister Henda.

To my son Samuel: "This is just the beginning..."

Contents

List of Figures

List of Tables

Abstract

Decarbonization of maritime transport requires immediate action. In the short term, ship weather routing can provide greenhouse gas emission reductions, even for existing ships and without retrofitting them. Weather routing is based on making optimal use of environmental information and knowledge about vessel seakeeping and performance. Combining them at a state-of-the-art level and making use of path planning in realistic conditions can be challenging.

To address these topics in an open-source framework, this thesis led to the development of a new module called *bateau* , and to its combination with the ship routing model VISIR. *bateau* includes hull geometry and propulsion modelling for various vessel types. It has two objectives: to predict the sustained speed in a seaway and to estimate the CO_2 emission rate during the voyage. Various semi-empirical approaches are used in bateau to predict the ship hydrodynamical resistance in both head and oblique seas. Assuming that the ship sails at a constant engine load, the involuntary speed loss due to waves is estimated. Numerical experiments via *bateau* are conducted for both medium-size and large container ships, for a bulk-carrier, and a tanker. The simulations of optimal routes are performed for a feeder containership during voyages along the maritime silk road (in the North Indian Ocean and in the South China Sea). Least-CO_2 routes are compared to the least-distance ones, assessing the CO_2 savings. Analysis fields from the Copernicus Marine Service are used in the numerical experiments.

This thesis also attempts to clarify the role played by the representation of the sea state. In particular, the influence of the wave steepness parameter is assessed. For dealing with ships with a greater superstructure, the wind added resistance is also estimated. Therefore *bateau* provides a tool to represent large vessels behaviour within VISIR, contributing to the computation of routes of minimal emissions. As such, It will be part of a modern and collaborative decision support tool for maritime transport.

Introduction

Maritime transport decarbonization plays a part in the roadmap of climate change mitigation. Over the past few years, the regulatory regime has been reinforcing the efforts towards limiting GHG from shipping.

Various options for decarbonization were proposed by both the academia and the industry. Their competitiveness is based not only on the potential of reducing CO_2 emissions but also in terms of time and cost-efficiency. In the short term, ship weather routing can deliver GHG emission reductions, even for existing ships and without retrofitting them. It is based on making optimal use of environmental information and knowledge of vessel seakeeping and performance. However, combining them at a state-of-the-art level and making use of path planning in realistic conditions is challenging. To address these challenges in an open-source framework, this thesis led to the development of a new module called *bateau* to predict the performance of large ocean-ongoing vessels, and to its combination with the ship routing model VISIR to estimate the optimal routes.

The developed module *bateau* is based on resistance and propulsion parametrisation for ship performance prediction and CO_2 emissions. It is applied to various ships and sea states and aims to respond to crucial questions needed for ocean-going vessels in sailing operation at sea: what is the added resistance exerted by the regular waves on a ship in head and oblique seas? what is the consequent involuntary speed loss and sustained speed while a ship is encountering waves from arbitrary heading? and what CO_2 emissions could a ship produce when sailing in rough seas?

Upon embedment into VISIR, the latter could give suggestions about the optimal routes, thereby avoiding rough seas and minimizing voyage distance and CO_2 emissions.

Therefore, this thesis is organized as follows:

- Chapter 1

  Introduces the nexus between maritime transport as a contributor to climate change, its potential on emissions mitigation and contribution to sustainable development goals. It presents the maritime decarbonization roadmap and measurements, showing the importance of voyage optimization in reducing the carbon footprint of ships. Then green corridors are discussed and the VISIR weather routing model is first introduced;

- Chapter 2

  Dedicated to presenting the vessel seakeeping parametrizations in *bateau* . This includes the calm water resistance, the wave-added resistance in both head and oblique seas, for both wave-diffraction and ship motion contributions, and the wind-added resistance. The chapter also provides methods to compute the delivered power and the sustained speed in presence of these resistances, and to estimate the CO_2 emission rate for typical two-stroke engines;

- Chapter 3

  This builds on the theory of Chap. 2 to outline the structure of the *bateau* module: the approximations made, the chosen vessels, the parameters used, and selected numerical results. In this chapter, only numerical experiments carried out in idealized conditions are considered. The role of wave dispersion was investigated.

- Chapter 4

  Documents the embedment of *bateau* 's vessel response into VISIR. It discusses VISIR settings and the geographical domain considered for the case-studies. It then provides the results for the optimal routes in realistic environmental conditions. Using Copernicus Marine Service analysis fields, it goes beyond the wave dispersion assumptions of Chap. 3. The resulting optimal route features are set in relation with the model components of Chap. 2 and with the bateau settings of Chap. 3. Related CO_2 emission savings are also presented;

- Chapter 5 recaps the main findings of this thesis work, along with its limitations and the outlook of future research.

Chapter 1

Maritime transport and decarbonisation

Chapter 1 is dedicated to setting the thesis in its general frame, and presents its goals and structure. At the beginning, it introduces the mutual nexus between the maritime transport and climate change in various aspects Sect. 1.1; on one hand, Sect. 1.1.1 highlights the severe impacts of climate change on the whole ecosystem on Earth. In addition, it focuses on the contribution of the anthropogenic Greenhouse Gas (GHG) emissions, in particular those emitted by vessels, to causing this threat. On the other hand, Sect. 1.1.2 explains the potential of shipping decarbonization to mitigate climate change.

The Sect. 1.2 reviews the maritime transport decarbonization roadmap (Sect. 1.2.1), the related regulations (Sect. 1.2.2) and measures (Sect. 1.2.3, Subsect. 1.2.4), and initiatives (Sect. 1.2.5).

The Sect. 1.3 focuses on the voyage optimization as an option of reducing GHG emitted by vessels, especially ship weather routing (Sect. 1.3.1) and speed optimization Sect. 1.3.2.

The Sect. 1.4 describes the VISIR model for ship weather routing used in the thesis, its previous results, its structure, and the environmental fields involved.

1.1 Maritime transport and climate change nexus

1.1.1 Impact of maritime transport on climate change

"As the mitigation to climate change report concluded, we are not on track to limit warming to 1.5°C. Average annual GHG emissions during the last two decades were the highest in human history." confirming the alarming situation of the climate highlighted by the Intergovernmental Panel on Climate Change (IPCC) [IPCC, 2022c].

Climate change is one of the greatest threats to both natural and human systems [IPCC, 2018]. It has caused considerable harm to the terrestrial and marine ecosystems, and those damages are progressively irreversible (high confidence) [Hans-O. Pörtner, 2022]. Extreme events, destruction of the ecosystem, increasing heat, mean sea level rise, and other impacts of climate change affect the livelihood and the socio-economic situation in many countries.

Human-induced climate change has already contributed of roughly 1.1°C to global warming, causing unprecedented changes affecting the ocean, its coasts, and its composition [von Schuckmann et al., 2021]. The main cause of climate change is the human-driven enhancement of the natural greenhouse effect. In the period 2012 to 2019, the average global greenhouse gas (GHG) emissions per annum reached their all-time highest levels [IPCC, 2022b]. Projected global GHG emissions in 2030 linked to Nationally Determined Contributions declared before COP26, reveals that warming will likely exceed 1.5°C, and limiting warming below 2°C is reliant on intensified fast mitigation efforts [IPCC, 2022a] Fig. 1.1.

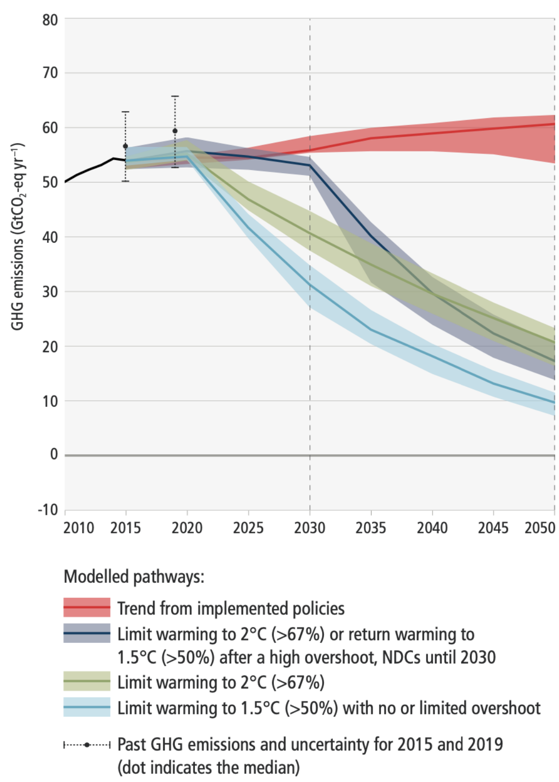

Figure 1.1: Global GHG emissions of modelled pathways[IPCC, 2022a]

CO_2 released in the atmosphere is the largest contributor to global warming. By 2020, its concentration in the atmosphere had risen to 48% above its pre-industrial level (before 1750), exceeding 417 parts per million (ppm) compared to 278ppm [NOAA, 2022]. Global CO_2 emissions currently are about 50 GT/year. Among the main causes of GHG are power generation, manufacturing, transport and land use [UN, 2022].

In 2019, direct GHG emissions from the transport sector accounted for 23% of the global energy-related CO_2 emissions, 11% coming from shipping [IPCC, 2022d], which can vary from 600 to $1,100$ $MtCO_2$ per year over the past decade as shown in Fig. 1.2 from the IPCC AR6.

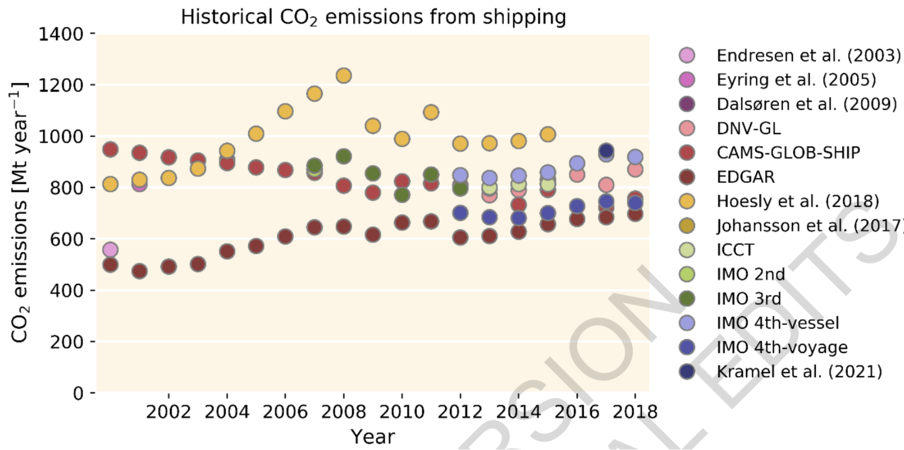

Figure 1.2: CO_2 emissions (Mt year-1) from shipping 2000–2018. Data from various inventories as shown in the key [IPCC, 2022d].

Maritime transport remains the backbone of globalized trade and the manufacturing supply chain, as about 80% of world merchandise trade by volume is carried by sea [UNCTAD, 2021]. The total volumes of international maritime trade reached an all-time high of 11 billion tons in 2018 [UNCTAD, 2019]. This growth is projected to attain an annual average rate of 3.4% during 2019 – 2024. This growth in transport volumes was accompanied by an increase in GHG emissions from shipping, against an improvement of the energy efficiency of only 1% per year since 1970 ([Lindstad, 2013]). According to the emissions inventory reported by the Fourth IMO GHG Study [IMO, 2020a], the share of shipping emissions in global anthropogenic emissions increased from 2.76% in 2012 to 2.89% in 2018, with a dominant contribution of carbon dioxide (CO_2) which constitutes 91% of shipping's climate impact, as measured by IPCC's Global Warming Potential Fig. 1.3.

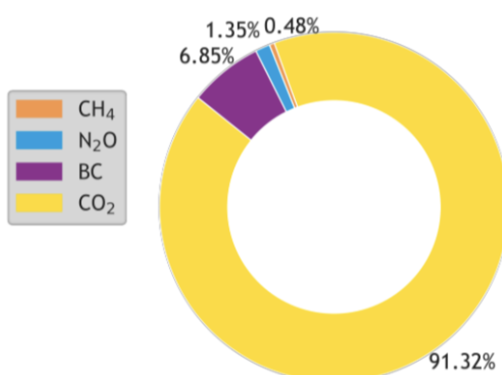

Figure 1.3: Contribution of individual species to voyage-based international greenhouse gas emissions in 2018 [IMO, 2020b]

A study conducted by [UNCTAD, 2021] shows that the most CO_2 emitters are container ships, followed by bulk carriers and tankers Fig. 1.4.

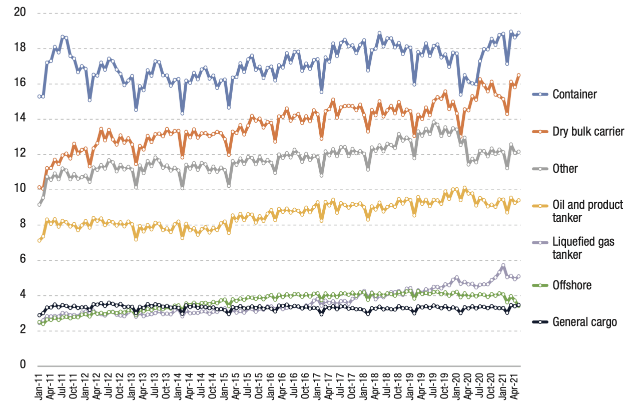

Figure 1.4: Carbon dioxide emissions by vessel type, monthly, million tons, 2011 − 2021[UNCTAD, 2021]

This was confirmed by [IMO, 2020a] stating that the contribution of the aforementioned ship types is about 75% of the total GHG emissions from international maritime shipping, and that the fleet's carbon intensity (CO_2 emissions per transport work) trend is dominated by operational drivers. It highlights the fact that the control of emissions by policies focused on technical efficiency is unlikely to be as cost-effective, or effective, as policies focused on operational efficiency. Thus, stringent operational carbon intensity regulations and measures are needed for both domestic and international shipping to reach the short-term decarbonization objectives.

1.1.2 Ocean-based transport mitigation

The ocean has a crucial role in sinking about 30% of the anthropogenic CO_2 emissions from the atmosphere [Friedlingstein et al., 2022] and regulating global temperatures by absorbing about 90% of the excess heat trapped in the atmosphere through the greenhouse effect [Cheng et al., 2021]. However, ocean health and functioning are threatened by accelerated climate change leading to an increase of the ocean heat content and sea level rise, more warming and acidification, which destroy the marine ecosystem and the economic potential of ocean activities. Hence, lowering emissions due to ocean-activities would protect ocean ecosystems and contributes to achieving the temperature stabilisation goals established in the Paris Agreement on Climate Change [UNFCCC, 2015]. Moreover, this will enhance the sustainable blue economy, and impact positively on the sustainable dimensions in terms of environment, economy, society and governance, toward reaching development goals [Hoegh-Guldberg et al., 2019]. The High-Level Panel for a Sustainable Ocean Economy [1]gives a comprehensive assessment of the mitigation potential of the ocean-based activities: maritime transport, renewable energy, seabed storage of carbon, food production (fisheries, aquaculture), and ecosystems. The contribution of the ocean-based mitigation is estimated to close the emissions gap by up to 21% in 2030 and 25% in 2050 with respect to 1.5°C and 2°C pathway [Hoegh-Guldberg et al., 2019]. The mitigation potential of ocean-based transport is

[1] : https://oceanpanel.org/

considered to reach about 0.25 to 0.5 GT CO_2e per annum in 2030, and 0.9 to 1.8 GT CO_2e per annum in 2050. However, to transform this potential into actual emission reductions requires a synergy between policy, research, and technology Fig. 1.5 [Hoegh-Guldberg et al., 2019].

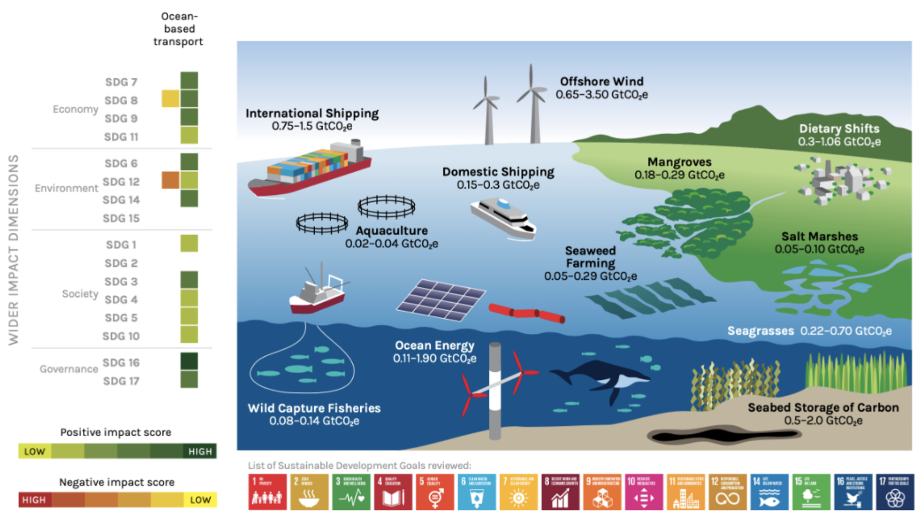

Figure 1.5: Projected ocean-based mitigation options and associated annual mitigation potential in 2050 adapted from [Hoegh-Guldberg et al., 2019]

According to the IPCC Sixth Assessment Report (AR6), limiting global warming is far from being achieved without fast and efficient interventions from all sectors to reduce emissions. This entails a transition in the energy sector by improving the energy efficiency, the deployment of alternative fuels and other new technologies [IPCC, 2022b]. Similar to other transport sectors, decarbonizing shipping still requires R&D and stringent regulations to manage and apply different solutions but also first movers and exemplary case studies. This is clear in the case of the uptake of low carbon fuels: producers of bunker fuels will not start production if there is no demand's signal from the market, nor will shipowners make significant investments on ships using low-carbon fuels before their widespread availability. This was pointed out by Lloyd's Register with their "Silk Alliance" project and mirrors the Clydebank declaration at COP26 on green corridors[2].

At a global level, maritime regulations are defined by the International Maritime Organization (IMO) which provides a forum for the agreement, adoption and implementation of international regulations. The primary international regulations for maritime environmental protection fall under The International Convention for the Prevention of Pollution from Ships (MARPOL). Regional implementation of such regulations can be stricter than MARPOL. The sixth Annex of MARPOL regulates emissions of oxides of sulphur (SO_x) by limiting the sulphur content of fuel; restricts oxides of nitrogen (NO_x) through engine NO_x controls; and aims to address greenhouse gases (GHG) through technical and operational energy efficiency measures.

Abatement of GHG emissions will affect long-term sustainable development, well-being, and

[2]https://www.lr.org/en/insights/articles/cop26-outcomes-for-shipping/

governance in the form of cobenefits and trade-offs [IPCC, 2018].Mitigation of transport emissions as a pillar of ocean-based actions has an important role and impacts towards achieving the UN Sustainable Developmental Goals (SDGs). [Hoegh-Guldberg et al., 2019] shows this impact on four dimensions: the environment, the economy, society, and governance Fig. 1.5.

What remains necessary is scaling-up the deployment of new energy efficiency technologies and overcoming market barriers and failures. Introducing encouraging policies and private initiatives would enable facing those challenges. Moreover, the use of low- and zero-carbon fuels is still at low Technology Readiness Level (TRL)([LR and UMAS, 2019]). The key priorities of readiness levels mainly concern three aspects: scaling technology, stimulating investment and ensuring sustainability. Fuel cost is a significant barrier to investment in addition to the absence of policies to close the gap. Both the technical and commercial viability of the Scalable Zero Emission Fuels (SZEF) face several other issues; e.g.high volume and safety problems especially for hydrogen and ammonia [LR, 2022c].

Reducing energy consumption is considered the lowest-cost way to abate emissions, and it depends on best practice at design and operational level. Thus, prioritizing operational measures seems a reasonable way to reach short term decarbonization levels. Research related to decarbonization presents great opportunities for the market to provide hardware, technologies, and services, and for countries with higher blue economic potential to involve it into its strategy. Deployment of operational measures is easier and more economic, feasible in short-term and should lead to significant results ([Zis and Psaraftis, 2019],[Serra and Fancello, 2020]).

1.2 Shipping decarbonization measures

The Paris Agreement is a legally binding international treaty on climate change. It was adopted by 196 Parties at COP 21 in Paris, on 12 December 2015 and entered into force on 4 November 2016. It aims to gradually reduce the use of fossil fuels and CO_2 emissions to reach net carbon neutrality by 2050 and keep global warming below 2°C by the year 2100. Decarbonization refers to the process of limiting anthropogenic carbon dioxide (CO_2) emissions, and it requires an energy transition for all sectors. The energy transition refers to the global energy sector's shift from fossil-based systems of energy production and consumption including oil, natural gas and coal to zero carbon energy sources (e.g.renewable energy sources like wind and solar). Decarbonizing shipping is a tough challenge for the maritime industry and needs to be included in their business strategy. In maritime transport, the energy transition requires the use of low and zero-carbon fuels besides other opportunities available from increased energy efficiency through technical and operational measures, and better management of energy demand. This also requires an evolution of the energy system and shipping system in terms of the timescale of development and investment as well as life cycle assessment [Smith, 2019]. Moreover, the success of deploying alternative fuels relies on the combination of regulations and business models.

1.2.1 Decarbonization pathway

More than 80% of world merchandise trade is carried by sea, and international shipping and ports provide vital linkages in the network of supply-chains and global trade. Despite the efficiency of maritime transport in terms of cost and time, it is facing a challenge to reduce its carbon footprint. In 2018, the International Maritime Organization (IMO) set its initial strategy to reduce the average carbon intensity of international shipping by at least 40% by 2030, pursuing efforts towards 70% by 2050, as compared to 2008 levels, and the total GHG emissions by at least 50% by 2050 compared to 2008 Fig. 1.6. Nonetheless, recent studies show that IMO targets are not in agreement with CO_2 reduction pathway of the Paris Agreement temperature goals, which would require a 34% reduction in emissions by 2030, and zero emissions by 2050 ([Bullock et al., 2022], [ICCT, 2021]). This gap was recognized by the 77th Marine Environment Protection Committee (MEPC) which agreed to initiate the revision of the Initial IMO Strategy on Reduction of GHG emissions from ships, which also means intensifying efforts towards decarbonization [IMO, 2021].

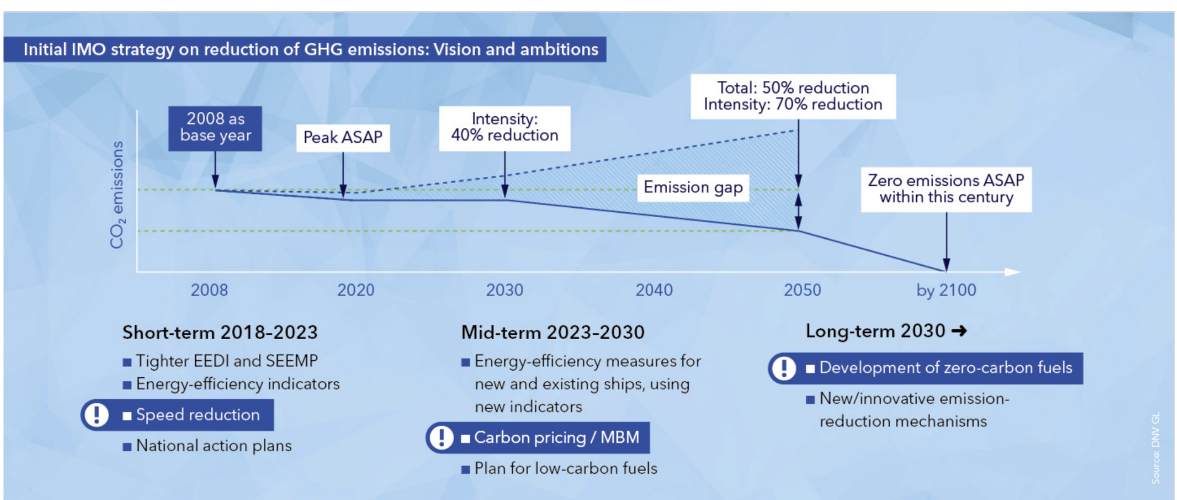

Figure 1.6: Decarbonization pathway[DNV, 2022a], EEDI:Energy Efficiency Design Index, SEEMP:Ship Energy Efficiency Management Plan, MBM:Market Based Measurements

In short-term (2018 – 2023) emissions reduction, the use of some energy efficiency indicators and technical and operational measures are prioritized. The medium-term (2023 – 2030) decarbonization pathway is based on further improving and implementing short-term measures, implementing Market Based Measurement (MBM) and providing incentives to reduce emissions. Development of policies such as carbon pricing / taxing to enable a business case for adopting low carbon could promote the energy transition of shipping [Hoegh-Guldberg et al., 2019]. The European Union (EU) is considering including shipping in its emissions trading schemes (ETS), with the details still to be agreed upon but expected to come into force in 2023, along with the Carbon Intensity Indicator (CII). The proposition is that shipowners conducting voyages within Europe, or start or end at an EU port, will have to pay for carbon permits to cover the CO_2 emitted by their vessel. Other measurements e.g. a bunker levy, or hybrid schemes, are to be agreed on and implemented by 2030. In the long-term (beyond 2030), IMO foresees more innovative technologies that need to be introduced as well as the deployment of low- and zero-carbon fuel.

1.2.2 IMO regulatory measures

In order to reach reduction goals set in its roadmap (Sect. 1.2.1), IMO has adopted technical and operational mandatory measures for new and existing vessels. Other Market Based Measurement (MBM) proposals are submitted to IMO to reduce 'in-sector' and 'out-sector' emissions from emissions. Further regulations are proposed within the European Green Deal program within the 'Fit for 55' package, as explained in this section.

Technical measures

- Energy Efficiency Design Index (EEDI)
  The EEDI is the most relevant technical measure promoting the energy efficiency of ships. It estimates the mass of CO_2 per transport work, in other terms the ratio of 'environmental impact' divided by 'the benefit for society', and it is a function of installed power, the vessel's speed, and the cargo carried. Since 1st January 2013, new ship designs need to comply with the reference level for each ship type, which is continuously tightened each five years. The EEDI stimulates industry to keep improving energy efficiency of new ships with innovative technologies.

- Energy Efficiency Existing Ship Index (EEXI)
  More recently, during the $MEPC - 76$ meeting in June 2021, amendments relating to technical and operational measures to cut the carbon intensity of international shipping were adopted. These amendments will enter into force on 1st November 2022, and include the calculation and verification of Energy Efficiency Existing Ship Index (EEXI) – retroactive EEDI requirements applied to existing ships from 1st January 2023 [IMO, 2022]. EEXI will be applied for existing vessels over $400GT$. It describes the CO_2 emissions per cargo ton and mile and "determines the standardized CO_2 emissions related to installed engine power, transport capacity and ship speed" [DNV, 2022b]. Thus, the EEXI limits the amount of CO_2 emitted per unit of transport supply [Mallouppas and Yfantis, 2021].

Operational measures

- Ship Energy Efficiency Management Plan (SEEMP)
  The SEEMP is a management plan for raising operational efficiency for new and existing ships by optimizing vessel speed, the use of weather routing, increased frequency of hull or propeller cleaning. SEEMP is specific to a ship since it considers unique factors, such as cargo, routes, dry docking schedule, as well as broader corporate or fleet level

strategies [Bradley, 2020]. Additionally, it aims to help shipping companies manage the energy efficiency of their fleet through the Energy Efficiency Operational Indicator (EEOI).The EEOI is a monitoring tool of carbon emissions during the voyage, thus enables operators to measure the fuel efficiency of an operative ship and to gauge the effect of any operational or technical change [IMO, 2009].

- IMO Data Collection System (IMO-DCS)
  Since 2019, under the IMO Data Collection System (IMO-DCS) [IMO, 2016], ships of $5,000$ GT and over must collect and report data on fuel consumption under SEEMP. These ships account for close to 85% of CO_2 emissions from international shipping. The data collected will provide a firm basis on which future decisions on additional measures will be made. The European Union (EU) has also implemented a system for monitoring, reporting, and verifying fuel consumption[EU, 2015] for ships of $5,000$ GT and over calling at ports in the European Economic Area (EEA), which will provide an overview on the operational efficiency of the ships.

- Carbon Intensity Indicator (CII)
  Another operational measure adopted during the MEPC-76 meeting in June 2021 is the introduction of a rating mechanism (A to E) linked to the operational CII which indicates the average CO_2 emissions per transport work applied to individual ships and determines the annual reduction factor needed to ensure continuous improvement of the ship's operational carbon intensity, taking effect from 1st January 2023. An enhanced Ship Energy Efficiency Management Plan (SEEMP) will include targets for operational emissions, where an approved SEEMP needs to be kept onboard from 1st January 2023. The IMO will likely review the effectiveness of the implementation of the EEXI and CII by January 2026 [IISD, 2020].

Fit for 55 Package

The European Green Deal is a programme outlined in the political guidelines of the European Commission to make Europe the first climate-neutral continent by 2050, in line with the 2015 Paris Agreement. On 14 July 2021, the European Commission launched its Fit for 55 package of legislative proposals in order to ensure the success of the European Green Deal to reduce the EU's total GHG emissions by 55% by 2030, towards full EU decarbonization by 2050. Five proposals are set out in the Commission's 'Fit for 55' package [EP, 2022]:

- European Trading System (EU-ETS)
  A revision of the European Union Emission Trading System (EU-ETS) with the aim of requiring ships to purchase CO_2 emission credits [European-Commission, 2022]. The measure would apply to all ships currently subject to reporting in the EU-MRV regulation [EU, 2015]. The CO_2 reported regards only emissions on board ships ('tank-to-wake').

- FuelEU Maritime
  The FuelEU Maritime Regulation is a proposed regulation on sustainable maritime fuels which aims to drive the shift towards low carbon maritime fuels, and is applied to all EU-ports. This regulation would account for the GHG emissions occurring during the whole supply chain of the fuel life cycle ('well-to-wake'). However, it has recently been criticised because of its limited ambition [Abbasov et al., 2022].

- Alternative Fuels Infrastructure
  The Alternative Fuels Infrastructure is proposed as a regulation that will require EU member states to ramp up the availability of the Liquified Natural Gas (LNG) by 2025 and onshore electrical power supply by 2030 in core EU ports.

- Energy Taxation Directive
  The Energy Taxation Directive has been revised to remove the tax exemption for conventional fuels used between EU ports as of 1st January 2023, and incentivise the uptake of alternative fuels.

- Renewable energy directive
  This directive sets the new EU economy-wide target of an at least 40% share of renewable energy sources in 2030, and aims to reduce GHG emissions by at least 13% by 2030 in the transport sector.

- Carbon Border Adjustment Mechanism
  This was agreed upon to take part in the European Union's 'Fit for 55' package. It aims to avoid carbon leakage and incentivise countries to put in place carbon pricing regulations in place in order to mitigate climate change. Moreover, it is developed to work in parallel with the EU-ETS, to mirror and complement its functioning on imported goods, to progressively replace the existing European Union mechanisms to deal with the risk of carbon leakage especially the free allocation of EU-ETS allowances [European-Council, 2022].

Market Based Measurements

In the medium and long-term decarbonization pathway, MBM may increasingly encourage ship operators to comply with IMO GHG regulations. MBM measures are based on economic variables and/or tax levies and they aim to encourage the shipping industry to reduce their carbon footprint on an economic basis by investing in the abatement technologies and alternative fuels, and offsetting in other sectors [Mallouppas and Yfantis, 2021].

1.2.3 Vessel retrofitting

Retrofitting the existing vessels is also a technical option, and consists of applying changes at the level of vessel design (hull optimization, bulbous bow retrofit, etc..), propulsion by using the propeller ducts or adding some energy-saving devices e.g. Pre-and post-swirl, and other engine technologies (waste-heat recovery, hybrid diesel-electric). The choice of technical options to raise the energy efficiency of ships, depends on the industry readiness and the cost-effectiveness level. Each of these technologies has been assessed for its applicability (ship categories), availability (entry into-service dates), carbon reduction potential and cost (capital and operating). As such, operational efficiency becomes more important [Bullock et al., 2020].The ship lifetime and age also play a role, whereupon retrofitting ships to accommodate engines and fuel systems for new fuel types may not be an option for older vessels. Various decarbonising options are emphasised to help in complying with regulations and reaching zero carbon emissions targets, and summarized in Fig. 1.7.

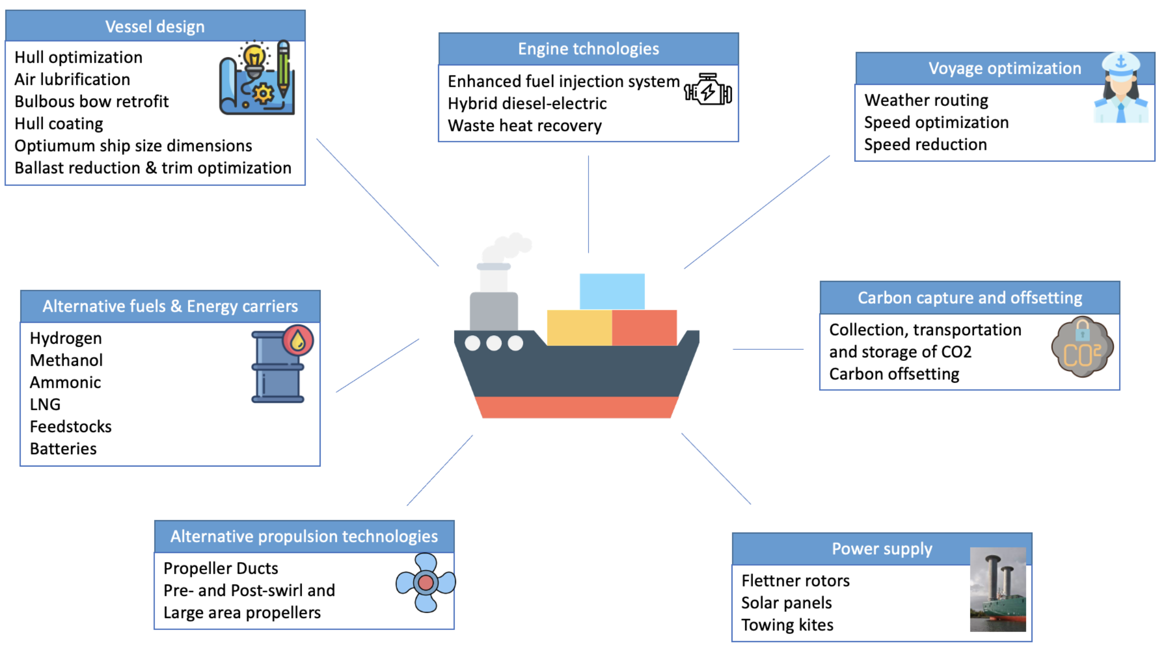

Figure 1.7: Decarbonization options

1.2.4 Alternative fuels

Feedstocks and energy carriers

The IPCC Sixth Assessment Report considered the feedstocks and the energy carriers as further options to mitigate GHG emissions from international fleets. The feedstocks could be fuels from biomass, fuels produced from renewable electricity, CO_2 capture from flue gas, and fuels produced via thermochemical processes (solar fuels). The energy carriers are the synthetic fuels (Hydrogen, Ammonia, Methane, Methanol, and synthetic hydrocarbon diesel) identified as having the highest potential for operational emissions mitigation, and the direct use of electricity stored in batteries. The Hydrogen and Ammonia when produced from renewable or coupled CCS may reduce the CO_2 emissions of up to $70 - 80\%$ compared to low-sulphur heavy fuel oil [Gilbert et al., 2018]. However, the transport and storage of these fuels are challenging and require further development of technologies and procedures for safer handling onboard and onshore of these fuels, and faster uptake [Hoegh-Guldberg et al., 2019]. The potential of emission reductions of the alternative fuel depends on its genesis; the e-Methanol produced via Hydrogen from electrolysis and carbon capture from the air reduces emissions up to 80%; however the Methanol produced from biomass increase emissions by 7.5%. The LNG is considered of a lower potential compared to the alternative fuels, although it is of higher availability and leads to lower emissions than the heavy fuel oil [Gilbert et al., 2018]. In addition to fossil and e-fuels, there is a growing interest in on-board technologies for capturing carbon, with prototype ships underway showing $65 - 90\%$ potential reduction in CO_2 emissions [JSTRA, 2020]. However, this solution is facing many challenges in designing CO_2 storage tanks for transport to shore because of its high volume, the increase of operating costs, and the limited onboard power supply [Fang et al., 2019]. The IPCC Sixth Assessment Report (AR6) [IPCC, 2022d] raised awareness on the need for a combination of the demand management solutions with new technologies, such as the use of advanced biofuels and hydrogen-based fuels for shipping. Similar to other transport sectors, decarbonisation options for shipping still require Research and development (R&D), though advanced biofuels, ammonia, and synthetic fuels are emerging as viable options (medium confidence) [IPCC, 2022d]. Improved efficiency has a limited effect on reducing the emissions from shipping, and natural gas-based fuels are likely unable to reach decarbonisation goals (high confidence). High energy density and low-carbon fuels are needed, however they have not yet reached commercial scale. Advanced biofuels could provide low carbon fuel (medium confidence), but its production depends on the current TRL of each conversion technology. Other synthetic fuels produced using low-carbon hydrogen with captured CO_2 still need demonstration at scale (low confidence). There is an increased effort to expand the deployment of low-carbon energy technologies to abate emissions from shipping(high confidence) [IPCC, 2022d]. Issues on the development of lifecycle GHG/carbon intensity guidelines for all relevant types of fuels have also been discussed. The position of the EU is that the guidelines should include a methodology that allows ship operators to compare the well-to-wake emissions of different alternative fuels [Healy, 2020]. Life cycle assessment is a technique for assessing the environmental impacts of the manufacturing stages of a specific product (here the alternative fuel), and consists of four phases under [(ISO), 1998] guidelines: Goal and scope definition, Inventory analysis, Impact assessment, and Interpretation. Its application on alternative fuels leads to three categories of life cycles: Well-to-Tank (from a fuel production to a fuel tank), Tank-to-Wake (from a fuel tank of ship to fuel consumption to operate ship), and Well-to-Wake (from a fuel production to fuel consumption to operate ship) Fig. 1.8.

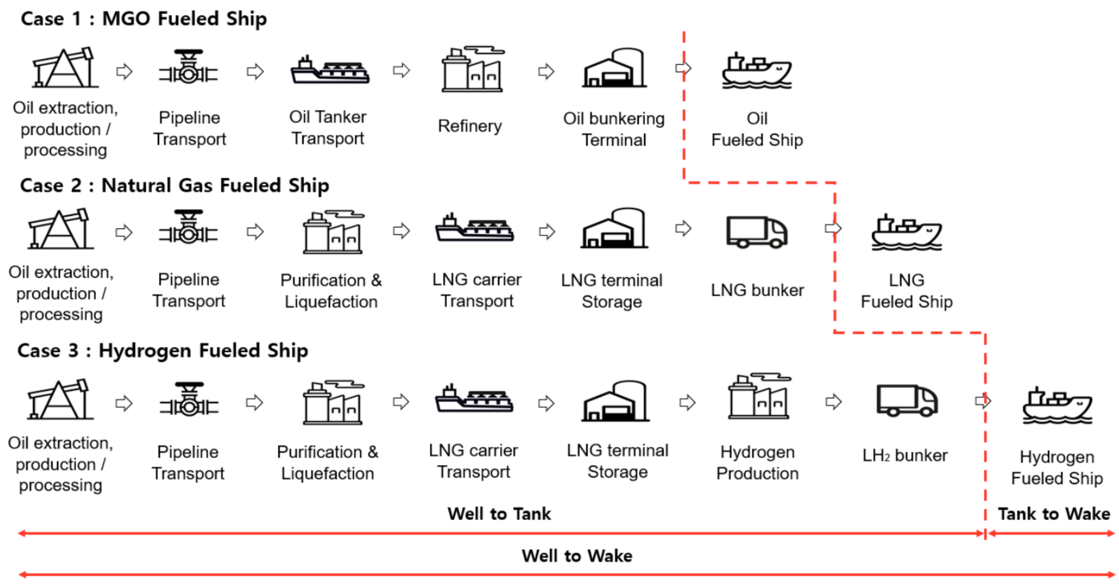

Figure 1.8: Life cycle of marine gas oil (MGO), natural gas, and hydrogen [Hwang et al., 2020]

The life cycle impact assessment for each phase considers the Global Warming Potential (GWP), the Acidification Potential, the Photochemical Ozone Creation Potential, the Eutrophication Potential, and Particulate Matter [Hwang et al., 2020]. [Xing et al., 2020] undertook a comprehensive review on countermeasures for CO_2 emissions from ships, and found that most technological and operational decarbonization options were highly context-sensitive and no individual measure in isolation could achieve the objectives of low carbon or zero carbon shipping. The paper makes the point that eco-friendly fuels and alternative power sources could be promising but their applications would significantly depend on ship types and ship routes, i.e., diversification and decentralization of ship power sources and marine fuel types are inevitable for future shipping. It was also highlighted that the main challenges in the maritime decarbonization pathway are the economic considerations and the legal framework. Shipping decarbonization and energy transition are intrinsically linked, however it is challenging to deploy them into scalable and impactful opportunities and policies. For instance, South Africa is considered a country with high potential availability of both renewables and maritime connections, and this makes a business case that could speed up maritime transport decarbonization[UMAS, 2022].

Zero-carbon fuels

There are both zero and net-zero carbon energy sources. Net-zero means that any carbon emissions created are balanced (or ‘cancelled out’) by taking the same amount out of the atmosphere. So the net-zero is reached when the amount of carbon emissions added is no more than the amount removed. Zero carbon means that no carbon emissions are being produced from a product or service (for example, a wind farm generating electricity, or a battery deploying electricity). Hydrogen and synthetic non-carbon fuels (ammonia), as well as battery power derived from zero-carbon electricity based on renewable energy could be considered as ‘zero-carbon’ fuels for reducing GHG emissions. If the emissions are offset by an equal amount of carbon stored into permanent geological sites, then the same fuels can become ‘net-zero’ fuels [Smith, 2019]. Fuels derived from biomass are also considered as ‘net-zero’, because the production of biomass absorbs CO_2 from the atmosphere in equivalent quantity to that emitted in combustion (as the biomass derived energy is still a hydrocarbon). The Coalition’s “zero carbon energy sources” describes the fuels derived from zero carbon electricity, biomass and the use of CCS[Smith, 2019]. Therefore, GHG emitted in upstream processes (e.g. land-use, harvesting, processing/refining, transport) needs to be considered and evaluated through the life cycle assessment of the alternative fuel. IMO regulations are likely applied only for operational emissions, and the fact that some zero-carbon fuels could have a significant upstream emissions put the energy transition at a risk.

1.2.5 Green Corridors

The Getting to Zero Coalition is a union and synergy effort of more than 200 organizations along the supply chain from various sectors (maritime, energy, infrastructure and finance), supported by key governments and intergovernmental organizations, and other stakeholders committed to decarbonizing shipping [Forum, 2021]. The coalition aims to get commercially viable deep sea zero emission vessels (ZEVs) operating in seaway trade lanes by 2030, endorsed by the integration of scalable net-zero-carbon fuels[3]. The Getting to Zero Coalition considers the Green Corridor as the next ’wave’ of cooperations towards decarbonization. The Green Corridor is a specific trade routes between major port hubs where zero-emission solutions are demonstrated and supported, a prioritized strategy to speed up energy transition and GHG emissions reduction. Among the important initiatives are the Lloyd’s Register in Silk Alliance and Memorandum of Understanding (MoU) between specific port authorities(e.g.‘World’s longest’ Green Shipping Corridor[4], world’s first transpacific green shipping corridor between ports in the United States and China[5])

‘World’s longest’ Green Shipping Corridor

The ports of Singapore and Rotterdam are considered two of the largest bunkering ports in the world. The Maritime and Port Authority of Singapore and the Port of Rotterdam Authority have lunched the world’s longest green corridor for shipping linking both partners. According to a MoU, this initiative is based on realizing the first sustainable vessels sailing on the route by 2027 by assembling a wide coalition of shippers, fuel suppliers and other stakeholders to jointly work towards a low- and zero-carbon alternative fuels transition, namely synthetic methane, hydrogen, as well as hydrogen-based fuels such as ammonia and methanol. The MoU is also seeking to raise the maritime efficiency and enhance safety. Moreover, it aims to digitalize the lane trade to share data of the flow of goods, which will

[3] https://www.globalmaritimeforum.org/getting-to-zero-coalition

[4] https://gcaptain.com/singapore-and-rotterdam-to-establish-worlds-longest-green-shipping-corridor/

[5] https://www.c40.org/news/la-shanghai-green-shipping-corridor/

ease the movements of vessels and cargo, and optimize just-in-time arrival of vessels among ports.

Silk Alliance

The Maritime Silk Road links the shipping trade from Southeast Asia to China, the Indian subcontinent and the Arabian Peninsula. It is one of the most important networks in maritime traffic, where the fleet crossing the North Indian Ocean (NIO) and South China Sea (SCS) is dominated by large ships e.g containerships, tankers and bulk carriers.
A bottom-up global emission inventory of shipping carried out by [Johansson et al., 2017] using the STEM model shows an important CO_2 emissions in both NIO and SCS.

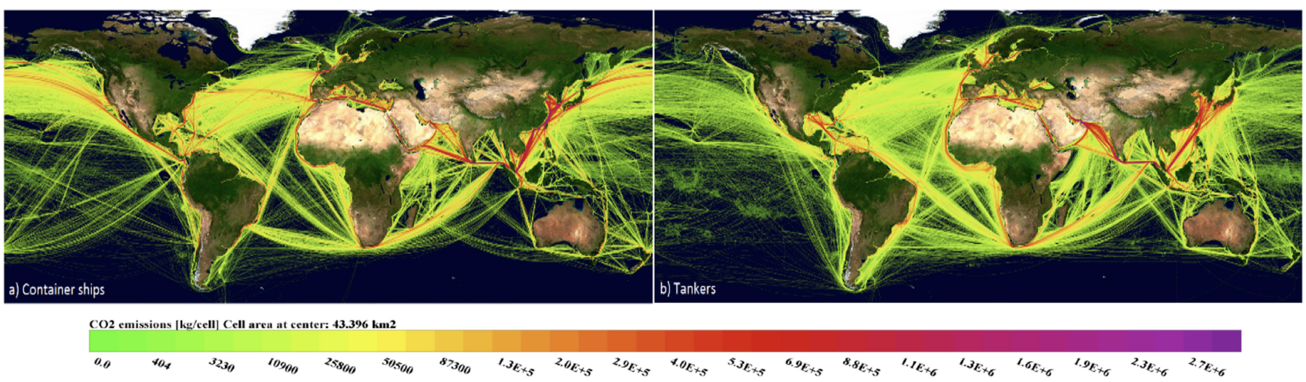

Figure 1.9: Global distribution of the CO_2 emissions for selected ship types and unidentified vessels in 2015. a) Container ships, b) tankers. Adapted from [Johansson et al., 2017]

This would suggest the need for more solutions for shipping decarbonization in the Silk Road. One of the important initiatives in the Maritime Silk Road is the 'Silk Alliance' lanched by Lloyd's Register Maritime Decarbonisation Hub in cooperation with 11 leading cross-supply chain stakeholders to develop a fleet fuel transition strategy that can enable the establishment of a highly scalable Green Corridor Cluster, starting with the intra-Asia container trade [LR, 2022a]. Ship weather routing could enhance the decarbonization potential in this area, one of the reasons for choosing the Silk Road domain to deploy a real case study in this thesis Chap. 4.

1.3 Voyage optimization

The alarming situation of climate crisis requires immediate actions to reduce CO_2 emissions. Decarbonizing shipping can contribute towards mitigating climate change if the available solutions are applied. Despite more limited emission reductions compared to radical changes in bunker fuel, most operational solutions are immediately viable. A voyage planning system based on weather routing and speed optimization can guide cost-efficient ship operations, enhance vessel safety, and reduce its carbon foot-print. This section reviews various methods used in ship weather routing algorithm in Sect. 1.3.1, followed by an overview of speed optimization in Sect. 1.3.2.

1.3.1 Ship weather routing

Ship weather routing is a decision-making process that aims at finding the optimal path and the speed through water for a voyage considering the environmental conditions encountered. The final objectives of voyage optimization could be minimizing fuel consumption, or CO_2 emissions, or operating costs, or again maximizing some safety constraints or passenger comfort [Zis et al., 2020]. However, voyage optimization by considering weather conditions is challenging as it requires the synergy expertise in naval architecture, oceanography, and software engineering. In research studies, there is a lack of open-source ship weather routing products. In the present study, we seek to fill this gap and to present the results of a real case study using VISIR model.

There are different ways to classify these systems related to weather routing, following[Fanjul et al., 2022] one can distinguish; strategic or tactical planning, global or local optimization, single or multi-objectives, deterministic or stochastic. [Zis et al., 2020] made a further review on the methodologies to solve the weather routing problem and provides a taxonomy based on various parameters (e.g. discipline, application area, etc.), and highlights the need for more benchmarking to facilitate the comparison between different approaches. [Walther et al., 2016] reviewed the optimization algorithms in ship weather routing and found that the selection of the most convenient approach depends on the requirements of optimization objectives, control variables and constraints as well as the implementation.

Various methods are used to compute optimal routes, such as the isochrone method, calculus of variations, dynamic programming, graph-search based methods (e.g. based on Dijkstra's or A* algorithm), Monte Carlo and genetic algorithms, artificial intelligence and machine learning. They are presented in more detail in the following paragraphs.

- Isochrone method

  The Isochrone method is based on computing the envelop of positions, called 'isochrones', attainable by a vessel at a given time lag after departure, and it has been used as a manual for navigation[Mannarini et al., 2016]. This method was invented by [James, 1957], then extended by [Hanssen and James, 1960] for route optimization based on weather conditions. [Hagiwara, 1989] found that the length of the isochrones changes depending on the environmental conditions, and proposed the Modified Isochrone Method to minimize either fuel, cost or time. [Lin et al., 2013] developed a three-dimensional modified isochrones method which uses the recursive forward technique and floating grid system and the great circle sailing as the reference route in the Earth's Coordinate System, and considers the effect of multi-dynamic elements on the voyage for determining the optimal route. The isopone method is yet another extension of the Modified Isochrone Method based on the use of planes of equal fuel consumption that define the outer boundary of the attainable regions in three-dimensions (i.e. geographical position and time), called 'isopones'. It enables considering different values for the ship engine power used in the optimised route. A review of the variants of the isochrone method done by [Szlapczynska and Smierzchalski, 2007] shows their weaknesses, in terms of the limitations in the form of vessel speed characteristics and in dealing with landmasses, especially near narrow straits which was addressed in the paper by screening all route portions intersecting the landmass.

- Dynamic programming
Dynamic programming consists of dividing a complex problem into sub-problems in order to solve it. This division is called 'stage' in the optimization procedure, and could be either time or a measure of voyage progress. The two-dimensional dynamic programming uses the voyage progress as the stage variable, assuming that the ship sails at a constant rate of revolutions and constant engine power. However, the three-dimensional method includes both engine power and ship sailing course as the control variables of the voyage. [Wei and Zhou, 2012] used the three-dimensional method method with a forward algorithm where the departure point of the voyage is fixed and the arrival point is flexible thus enabling a set of routes to minimize fuel consumption with different voyage duration. [Shao et al., 2012] used the same method for fuel saving.

- Pathfinding algorithms
The most commonly used pathfinding algorithms in the weather routing are Dijkstra's and A*. The Dijkstra's algorithm is a deterministic method for solving single or multi-objective optimization problems. It is a graph based method which serves to find the shortest path between two given nodes in a graph with positive edge weights (e.g. time). Dijkstra's algorithm guarantees finding the optimal path in the presence of static edge weights. Under specific assumptions, it was shown that this holds even in the presence of dynamic edge weights ([Mannarini et al., 2016], [Mannarini et al., 2019c]).
A* ("A-star") is a graph traversal and path search algorithm, and used in weather routing (e.g.[Grifoll et al., 2022]). It is considered as an extension of Dijkstra's algorithm where a heuristic is used for accelerating convergence towards the target location. However, this comes at the cost of losing the optimality ensured by Dijkstra. The A* algorithm enables finding the shortest path from a specific source to one goal (a specific-goal-directed heuristic), and not the shortest-path tree from a source to all possible targets allowed by the Dijkstra's algorithm.

- Machine learning and artificial intelligence
Machine learning is an algorithm enabling to develop a model based on training a sample of data to make predictions or decisions without being explicitly programmed to do so[Koza et al., 1996]. Ship weather routing has also attracted the artificial intelligence and machine learning research field. Artificial neural networks and other machine learning are increasingly used to predict the sailing speed and the fuel con-

sumption in a specific environmental and operational condition. [Zheng et al., 2019] embedded an artificial neural network model into these four improved particle swarm optimization algorithms to optimize the sailing speed in a case study of Norwegian waters. [Du et al., 2019] attempted to quantify the synergetic influence of sailing speed, displacement, trim, and weather and sea conditions on ship fuel efficiency using two artificial neural network models to handle ship voyage report data.

All the above-mentioned path-planning methods completely neglect the vessel performance in a seaway. However, the quality of the optimal route simulation relies on the accuracy of the ship hydrodynamics estimation, weather forecasting data, and the optimization algorithm [Lin et al., 2013]. Therefore, it is necessary to involve a vessel seakeeping modelling in the weather routing algorithm. This issue is addressed in Chap. 2 and Chap. 3 of this thesis.

1.3.2 Speed optimization

Speed optimization is considered a candidate for short-term measures to curb GHG emissions from shipping. The reason behind this is the non-linear (at least cubic) relationship between ship speed and power, and hence fuel consumption and emissions. However, some studies such as [Adland et al., 2020] confirmed that the "cubic law" is only true near the design speed of vessels, and the elasticity of fuel consumption with regards to vessel speed is substantially lower in the speed range where ships mostly operate.

Speed optimization entails a different operation to speed speed reduction or slow steaming, which is a voluntary measure to limit the speed applied in periods of depressed market conditions and/or high fuel prices especially for containerships due to their higher speeds [Psaraftis, 2019].

[IMO, 2012] defined the optimum speed as "the speed at which the fuel used per tonne mile is at a minimum level for that voyage", highlighting that it does not mean minimum speed since sailing at less than optimum speed will consume more rather than less fuel. This definition ignores the technical and commercial factors as well as the weather conditions affecting the speed. [Psaraftis, 2019] goes on to define the speed optimization as "the selection of an appropriate speed profile for the ship so as to optimize a specific objective while meeting various requirements (or constraints) on the ship's operation. The speeds that correspond to the chosen speed profile are called 'optimal speeds'."

Containerships sail at relatively higher speeds, compared to bulkers and tankers, which means more potential for speed optimization. Moreover, containerships have more powerful engines than the other types of large ships, therefore speed reduction will have a greater impact on emissions. From this perspective, speed optimization seems more relevant and feasible especially given no contractual barriers are imposed.

This is not the case for tankers and bulkers, where companies have to proceed with a "Just In Time Arrival" or "Virtual Arrival" clause in their contracts for ships sailing under voyage charter party: therefore, the shipowners and charterers can agree that the Requested Time of Arrival at the Pilot Boarding Place of the Port Authority can be accepted as the Notice Of Readiness. In addition to this, tankers and bulkers sail at relatively lower speeds than container ships and have less powerful engines, so realizing the same CO_2 savings is not expected [GloMEEP, 2020]. Therefore, speed management requires further investigation in terms of optimal speed for energy efficiency, particularly when it comes to real efficiency from speed reduction [Jimenez et al., 2022].

1.4 VISIR model

Among the measures for the decarbonization of shipping, IMO in its "initial strategy" considers voyage optimization [IMO, 2018]. This measure can apply to both existing ships and new-builds. However, to what extent emission savings from voyage optimization can amount to is still poorly assessed in the literature. This is partly due to the lack of open source, peer-reviewed models but also to lack of their extensive applications to multiple ship types and geographical domains.

The VISIR ship routing model [6] was designed and developed to contribute towards filling this gap. It is an open-source voyage planning model developed by the Euro-Mediterranean Center on Climate Change (CMCC) and University of Bologna. VISIR is considered as a single-objective deterministic model for ship weather routing. It is based on Dijkstra's algorithm, an exact graph-search method with time-dependent edge weights adapted to deal with the dynamic environmental fields. The model contains a masking procedure for coastline and sea-bottom awareness. It was deployed in the Mediterranean Sea [Mannarini et al., 2016] and in the Atlantic Ocean [Mannarini and Carelli, 2019a], for producing optimal routes for a motor and sailboat. Concerning the environmental data that can be used by VISIR, the analysis and forecast wave and current products from Copernicus Marine Service are used, with ECMWF or COSMO-ME for wind [Mannarini et al., 2015].

VISIR-1 is the first version of VISIR coded in MATLAB®, and and could account for wave fields only. VISIR-1b also considers also sea surface currents to estimate the speed over ground [Mannarini and Carelli, 2019a]. In VISIR-1a, the angular resolution of the routes was 26.6°, then improved to 7.1° in VISIR-1b, and to 14.0° or better in VISIR-2 thanks to a higher degree of connectivity of the underlying graph [Fanjul et al., 2022]. At the beginning, VISIR-1 included a parametrization of calm water and wave added resistance for motorboats. Then in VISIR-2 a ship simulator was used to estimate the involuntary speed loss, the fuel consumption and the CO_2 emissions. This, together with a further evolution of the Dijkstra algorithm, enabled computation of least-CO_2 routes for a ferry in the Adriatic Sea Fig. 1.10 [Mannarini et al., 2021]. The path planning component of VISIR was validated against both analytical benchmarks [Mannarini and Carelli, 2019a] and model inter-comparison [Mannarini et al., 2019b].

[6] https://www.visir-model.net

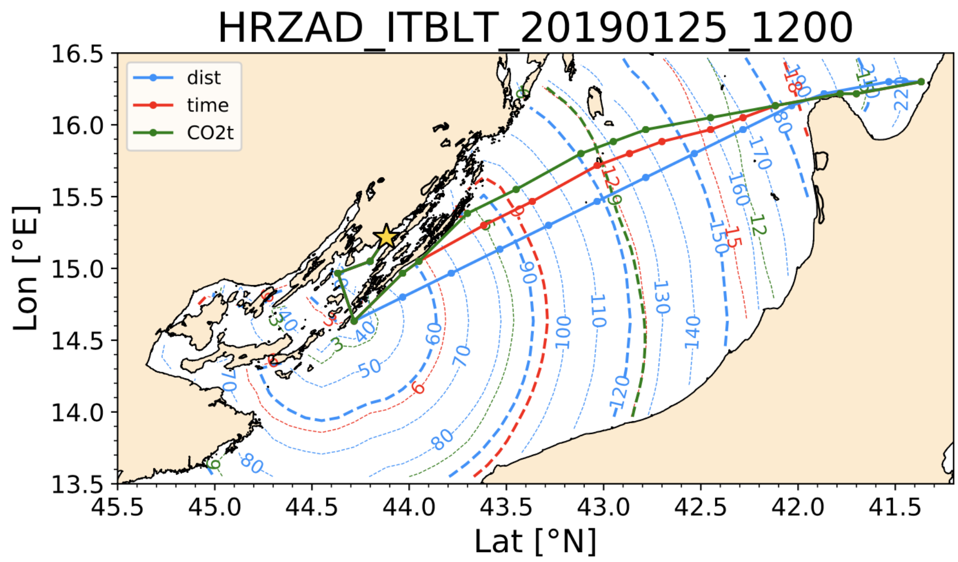

Figure 1.10: Exemplary results of route optimization. Least-distance, least-time, and least-CO2 routes are displayed respectively as cyan, red, and green lines with dots at the computed waypoint locations. The isolines corresponding to each route are displayed as dashed or dotted lines (for major or minor divisions, respectively) of the corresponding colour. The labels of the isolines are expressed in units of nautical miles, hours, or tonnes CO_2 , respectively [Mannarini et al., 2021]

VISIR-2 is a Python™ coded model. It is a complete refactor of VISIR-1 in python. It is more modular and flexible than its predecessor and includes several innovations regarding the vessel modelling, path planning, and the visualization of the results. Preliminary results obtained through VISIR-2 were published in [Mannarini et al., 2021]. VISIR-2 also powers the operational web service GUTTA-VISIR [7], which provides, on a daily basis, least-CO_2 ferry routes for the Adriatic and Ionian seas.

The VISIR model was extensively tested for its path planning component ([Mannarini et al., 2019b], [Mannarini and Carelli, 2019a]) and was engineered for powering operational systems (VISIR-NAV[8], GUTTA-VISIR). However, a featured ship modelling component is needed in VISIR. It will enable it to represent large ocean-going vessels in realistic sea states taking into account the effect of environmental conditions (e.g. waves). This is addressed within this study.

[7] https://www.gutta-visir.eu/

[8] http://www.visir-nav.com/en/join

Chapter 2

Theory of ship performance modelling

Sect. 2.1 reviews the geometrical and propulsion parameters of ship hulls, propellers, and engines. Some concepts of ship hydrodynamics are provided in Sect. 2.2. The chapter continues with the procedure of power and speed loss modelling in Sect. 2.3, and provides an estimation method for the ship's CO_2 emissions in Sect. 2.4.

2.1 Vessel parameters

The estimation of the resistances acting on the ship first of all requires a description of its geometry. In this thesis, the vessel is represented at an intermediate level between a zero-dimensional object and a fully three-dimensional digital twin of its real counterpart. Both the hull and the superstructure have to be characterized. Related parameters are introduced in Sect. 2.1.1 and Sect. 2.1.2.

The estimation of the sustained speed in a seaway requires, in addition to the resistance, also a characterization of the propulsion system. This comprises, as a minimum, both a propeller and an engine. Related parameters are introduced in Sect. 2.1.3 and Sect. 2.1.4.

2.1.1 Hull geometry

Coefficients of ship form

The coefficients of form show the relationship between the actual form of a ship and its dimensions. They include the block coefficient C_B, the midship coefficient C_M, the waterplane coefficient C_{WP}, and the prismatic coefficient C_P as shown in Fig. 2.1.

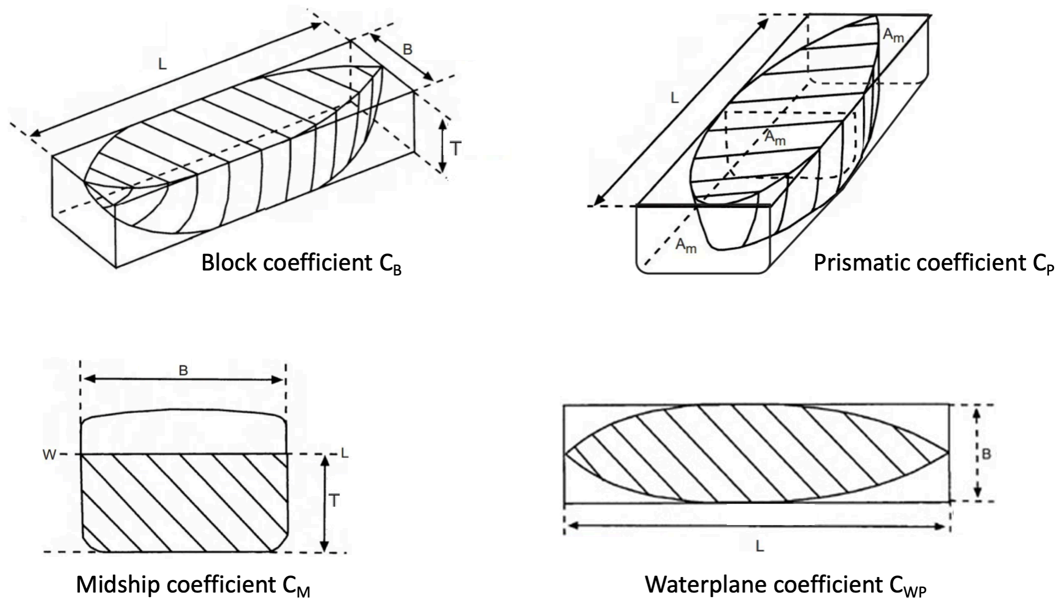

Figure 2.1: Form coefficients

- Block coefficient C_B

  The underwater hull form and its principal parameters are designed such that it displaces a prescribed volume of water $\Delta[m^3]$:

$$\Delta = L_{pp} \cdot B \cdot T \cdot C_B \tag{2.1}$$

  where L_{pp} is the length between perpendicular $[m]$, B is the beam $[m]$, T is the draught $[m]$, and C_B is the block coefficient $[-]$. C_B is an adimensional quantity determined by the fullness of the hull. [Molland et al., 2011] derived an empirical formula fitting data from vessels of various service speeds:

$$C_B = 1.23 - 2.41Fn \tag{2.2}$$

  Thus, faster vessels tend to have finer hulls.

- Midship coefficient C_M

  As seen in Fig. 2.1, the shaded portion represents the area of the midships section to the waterline WL A_M, enclosed in a rectangle having a breadth B and depth D, so that $C_M = \frac{A_M}{B \cdot D}$.

  The midship coefficient C_M can also be expressed as the ratio of C_B to the prismatic coefficient C_P:

$$C_M = \frac{C_B}{C_P} \tag{2.3}$$

  An approximation of C_M for small ships is $C_M = 0.78 + 0.21C_B$ and for large ships $C_M = 0.80 + 0.21C_B$ [Molland et al., 2011].

- Waterplane coefficient C_{WP}

  Fig. 2.1 shows the shaded area of the ship's waterplane A_{WP} and a rectangle having the same length L and breadth or beam B of the ship. The waterplane coefficient is expressed as the ratio $C_{WP} = \frac{A_{WP}}{L \cdot B}$. In the case A_{WP} is unknown, an approximation as function of C_B could be used as:

$$C_{WP} = 0.67C_B + 0.32 \tag{2.4}$$

- Prismatic coefficient C_P

  The prismatic coefficient of a ship at any draft is the ratio of the volume of displacement at that draft to the volume of a prism having the same length as the ship and the same cross-sectional area as the ship's midships area.

  In Fig. 2.1 above the shaded portion represents the volume of the ship's displacement at the draft concerned, enclosed in a prism having the same length as the ship and a cross-sectional area equal to the ship's midships area (A_M).

Angle of entrance i_E

The angle of entrance i_E determines the shape of the hull section at the fore end as shown in Fig. 2.2. Low i_E leads to a 'U' form and high i_E leads to a 'V' form. 'V' forms tend to move displacement nearer the surface and to produce more wavemaking. The effect of i_E depends on ship speed; at low speeds and with a large i_E there is high resistance, whilst at high speed a contrary effect may exist [Molland et al., 2011]. Therefore, the angle of entrance i_E is relevant for determining the ship resistance.

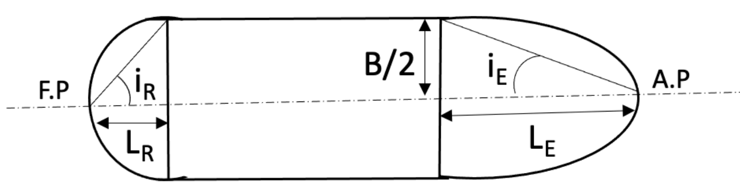

Figure 2.2: Length of entrance L_E and length of run L_R

it can be approximated as proposed by [Holtrop and Mennen, 1982] by:

$$\begin{aligned} i_E &= 1 + 89\exp(-A) \\ A &= (L/B)^{0.80856}(1 - C_{WP})^{0.30484}(1 - C_P - 0.0225lcb)^{0.6367}(L_R/B)^{0.34574}(100\Delta/L^3)^{0.16302} \end{aligned} \tag{2.5}$$

where C_{WP} is the waterplane coefficient, C_P is the prismatic coefficient, L_R is the length of run. Alternatively, the angle of entrance could simply be related to the block coefficient C_B as in Tab. 2.1.1, proposed by [Molland et al., 2011].

Table 2.1: Typical values of the angle of entrance [Molland et al., 2011]

C_B [-]	i_E [deg]
0.55	8
0.6	10
0.7	20
0.8	35

Form factor k_1

The form factor concept was introduced to consider the resistance component due to hull geometry and the viscosity of the water. The form factor is computed as suggested by [Holtrop and Mennen, 1982], or empirically as in [Shigunov, 2013] and [Feng et al., 2021]:

$$k_1 = -0.095 + \frac{25.6C_B}{(L_{pp}/B)^2\sqrt{B/T_M}} \tag{2.6}$$

where T_M is the midship draught assumed to be equal to the design draught in this study.

Wetted surface S

The wetted surface is the hull immersed area in water. It is usually estimated by hydrostatic programs. In this is not possible, [Kristensen and Bingham, 2017] give an approximation out of the analysis of 125 newer ships of various type and size.

$$S = \begin{cases} 0.99(\frac{\Delta}{T} + L_{wl}T) & \text{for bulk carriers and tankers} \\ 0.995(\frac{\Delta}{T} + 1.9L_{wl}T) & \text{for container ships (single screw)} \end{cases} \tag{2.7}$$

Waterline length L_{wl}

We can distinguish three lengths of the hull, length overall L_{oa}, L_{wl} waterline length, and L_{pp} length between perpendicular. The perpendiculars are drawn to the waterline at the points where either the after side of the rudder post or the fore-side of the stem meet the summer load line Fig. 2.3.

The L_{wl} can be approximated by:

$$L_{wl} = \begin{cases} 1.02L_{pp} & \text{for bulk carriers and tankers} \\ 1.01L_{pp} & \text{for container ships} \end{cases} \tag{2.8}$$

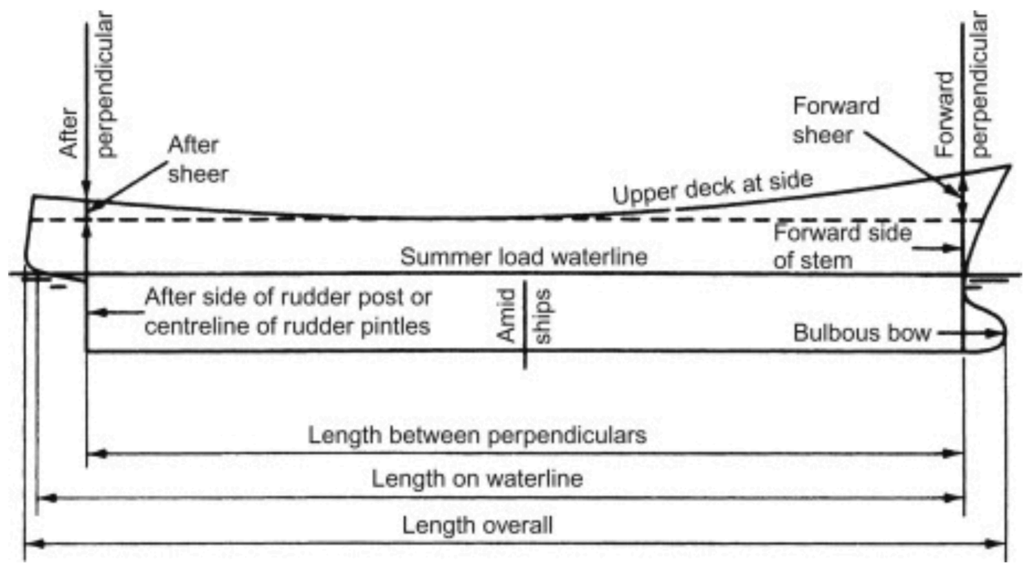

Figure 2.3: Ship lengths from [Molland et al., 2011]

Longitudinal center of buoyancy lcb

lcb is the longitudinal projection of the position of the centre of buoyancy. The centre of buoyancy is the centre of mass of the water mass displaced by the submerged part of the hull. As it is usually close to midship, lcb is expressed as the fraction of L_{wl} forward of the midship position. Results of the British Ship Research Association series [Lackenby, 1962] indicates a dependence of lcb as function of C_B for single screw ships as following [Molland et al., 2011]:

$$lcb = 20(C_B - 0.675) \tag{2.9}$$

Transverse bulb area A_{BT}

The transverse bulb area is the cross-sectional area at the forward perpendicular of the bulbous bow, as shown in the following figure:

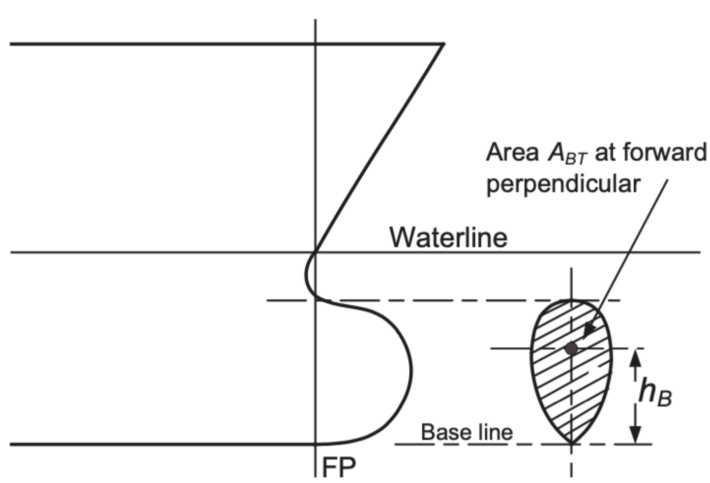

Figure 2.4: Bulbous bow definition [Carlton, 2019]

If the type of bulbous bow is not determined, [Charchalis, 2013] recommends taking the transverse sectional area of bulb as 8% of the midship area A_M.

$$A_{BT} = 0.08A_M$$
$$A_M = B \cdot T \cdot C_M \tag{2.10}$$

Center of bulb area above keel line h_B

h_B is the height of the centroid of cross-section A_{BT} from the base line Fig. 2.4. According to [Rakke, 2016], the center of bulb area above the keel line is estimated as a function of propeller diameter D_P as follows:

$$h_B = 0.4D_P \tag{2.11}$$

Transom area A_T

Transom stern is now a normal practice in modern ship design. When a ship is operating, a part of the transom is immersed. This causes a separation of the flow and a vorticity created behind the transom which means a pressure loss Fig. 2.5.

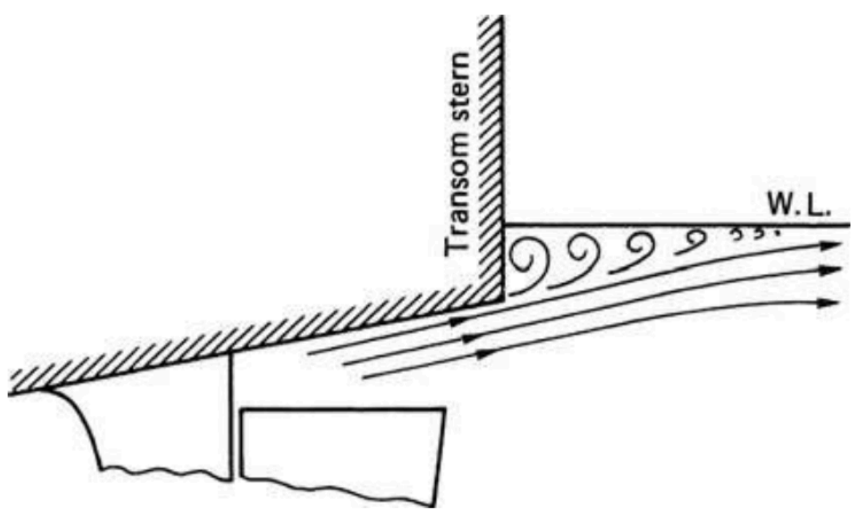

Figure 2.5: Flow around an immersed transom stern [Carlton, 2019]

This resistance depends on the area of the transom. An approximation of the latter as a function of the midship area is found in [Rakke, 2016], and reads:

$$A_T = 0.051A_M = 0.051C_M \cdot B \cdot T \tag{2.12}$$

2.1.2 Ship superstructure

The formula of wind-added resistance by [Fujiwara et al., 2005] involves all the exposed areas to wind as shown in Fig. 2.6.

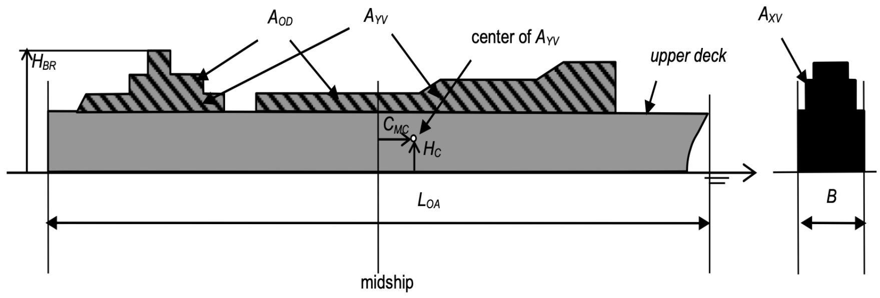

Figure 2.6: Input parameters for regression formula by [Fujiwara et al., 2005]

We assume that the lateral projected area of superstructure A_{OD} is equal to the lateral projected area above the waterline A_{YV} computed as in Eq. 2.13:

$$A_{YV} = L_{oa}(D - T + h) \tag{2.13}$$

where L_{oa} is the overall length, D is the ship depth assumed to be equal to $1.5T$, T is the draught, and h is the accommodation height.
For tankers and bulk carriers, the accommodation height h is defined by the number of floors of the superstructure. Floor height is assumed to be $3m$. An additional height of $2m$ is added for equipment on top of the ceiling. For container ships, h is estimated based on the number container tiers on deck, and includes some tiers of deckhouses extended above the container stack. The analysis made by [Kristensen and Bingham, 2017] suggests the following values for h:

$$h[m] = \begin{cases} 11 - 20.6m & \text{for feeder vessels} \\ 24.2 & \text{for panamax vessels} \\ 24.2 - 26.8 & \text{for post-panamax vessels} \end{cases} \tag{2.14}$$

The maximum transverse area or frontal area A_{XV} is expressed by [Kristensen and Bingham, 2017] as:

$$A_{XV} = B(D - T + h) \tag{2.15}$$

The height of top of superstructure (bridge, etc...) H_{BR} is estimated as following:

$$H_{BR} = D_s + h \tag{2.16}$$

The height from waterline to centre of the lateral projected area A_{YV} is also a relevant parameter and the symbol H_C is used.
The horizontal distance from midship section to centre of the lateral projected area A_{YV} is mentioned as C_{MC} and assumed to be null.

2.1.3 Propeller

The ship propeller is a device for generating thrust. It includes both a rotating hub and radiating blades which, when rotated, exert linear thrust upon water. Propellers could be classified as Fixed pitch propeller (FPP) and Controllable pitch propeller (CPP):

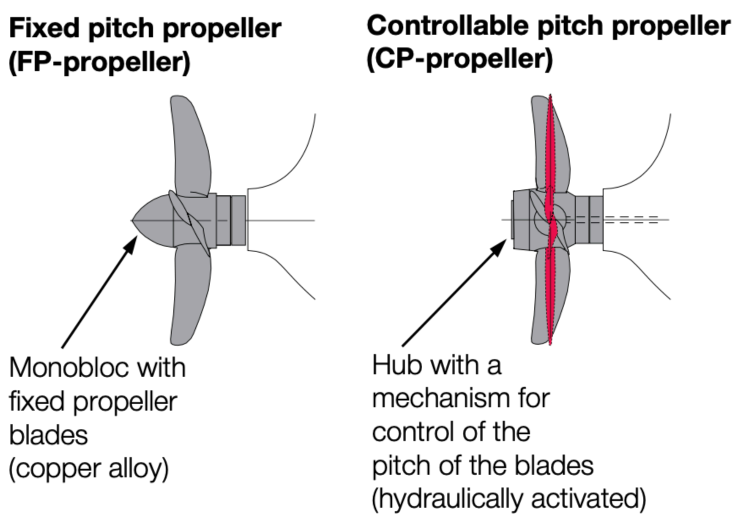

Figure 2.7: Propeller types from [MAN, 2011]

The latter have a relatively larger hub compared with the Fixed pitch propeller (FPP) since the hub must accommodate the hydraulically activated mechanism to control the pitch. This makes the CPP more expensive than FPP. The major advantage of the Controllable pitch propeller (CPP) is that it enables the engine operation at any revolution or load desired, depending on the capabilities of the propeller control system. Moreover, as it decouples the direction of thrust from the rotational direction of the engine, this ensures swift manoeuvring. For FPP, the position of blades and the propeller pitch is fixed and cannot be changed in operation. This means in rough seas the propeller performance curves (combination of power and propeller speed in rpm) will change according to physical laws.

Large ships sailing for a long distance usually use the FPP, due to the expensive cost and the lower propeller efficiency of CPP[MAN, 2011].

The main parameters for modelling the propulsion of a ship are related to the propeller open-water characteristics (POW), and the propeller design (e.g.diameter, number of blades).

Corrections due to the hull-propeller interactions

Hull-propeller interaction affects the propulsive efficiency, and includes the hull wake w and thrust t.

- Wake fraction w

  While the ship is sailing, a layer of water is formed due to the friction around the hull. Due to this boundary layer, the water locally arriving at the propeller with a velocity V_a will have an effective wake velocity $V_k = V - V_a$ relative to the vessel, directed as the ship's speed V [MAN, 2018]. V_k is expressed in dimensionless form by the mean of wake fraction coefficient expressed as:

$$w = \frac{V_k}{V} = \frac{V - V_a}{V} \tag{2.17}$$

The value of the wake fraction coefficient w depends significantly on the shape of the hull, as well as on the propeller's location and size, and considerably influences the propeller's efficiency [MAN, 2018]. In this study, the wake fraction w is computed according to [Holtrop and Mennen, 1982] formula.

- Thrust deduction fraction t

  When the hull is propelled, the rotation of the propeller causes the water in front of it to be absorbed back towards the propeller, generating a relative pressure fall at aft (with respect to the bow). Corresponding longitudinal pressure gradient leads to the loss of thrust or additional resistance F. So, that the thrust force T_h on the propeller has to overcome the total resistance R_t of the vessel and the augment of resistance or deduction of thrust F from the propeller [MAN, 2018]. The latter is expressed in dimensionless form by:

$$t = \frac{F}{T_h} = \frac{T_h - R_t}{T_h} = 1 - \frac{R_t}{T_h} \tag{2.18}$$

  In this study, the thrust deduction fraction t is computed according to [Holtrop and Mennen, 1982] formula.

Propeller open-water characteristics POW

An open-water test refers to the propeller testing without the presence of a vessel hull. Assuming a deeply submerged propeller and neglecting the effect of waves and currents, the thrust and torque coefficients K_T and K_Q, are derived as a function of the advance ratio J. They are defined as follows:

- Advance speed ratio J

  At the design stage, the propeller is tested in an open water, where the thrust is derived from accelerating the undisturbed fluid (not disturbed by the hull). However, when behind the ship, the propeller advances into turbulent water which has a forward movement, known as the wake. The relative advance speed is therefore reduced, known as the advance speed V_a. In dimensionless form, it is expressed as the advance number or the advance speed ratio J given by:

$$J = \frac{V_a}{nD_p} \tag{2.19}$$

  where n is the propeller rate of revolutions and D_p is the propeller diameter.

- Thrust coefficient K_T and torque coefficient K_Q

  K_T and K_Q are adimentional forms of thrust T_h and torque Q exerted by the propeller, thus given by:

$$K_T = \frac{T_h}{\rho n^2 D_p^4} \tag{2.20}$$

$$K_Q = \frac{Q}{\rho n^2 D_p^5} \tag{2.21}$$

The $K_T(J)$ and $K_Q(J)$ characteristic curves contain all of the information needed to determine the propeller performance at a particular operating condition [Carlton, 2019]. They are obtained by open-water tests and related to the geometrical configuration of the propeller and other hydrodynamic parameters:

$$\begin{aligned} K_T &= f\left(Re, J, P/D, A_e/A_o, Z, t/c\right) \\ K_Q &= f\left(Re, J, P/D, A_e/A_o, Z, t/c\right) \end{aligned} \tag{2.22}$$

where Re is the Reynolds number, J is the advance speed ratio, P/D is the pitch ratio, A_e/A_o is the blade area ratio, Z is the number of blades, and t/c is the ratio of the maximum propeller blade thickness to the length of the cord at a characteristic radius. Using typical propeller open-water characteristics (POW), the thrust coefficient K_T and the torque coefficient K_Q are found to be quadratic functions of the advance speed, thus can be computed as:

$$K_T(J) = a_T J^2 + b_T J + c_T \tag{2.23}$$

$$K_Q(J) = a_Q J^2 + b_Q J + c_Q \tag{2.24}$$

where T_h is the thrust and Q is the torque.

Propeller diameter D_P

[Kristensen and Bingham, 2017] gives an approximation of the propeller diameter D_P as a function of the maximum draught T (assumed to be the design draught in this study), based on statistical analysis:

$$D_P = \begin{cases} 0.395T + 1.3 & \text{for bulk carriers and tankers} \\ 0.623T - 0.16 & \text{for container ships} \\ 0.713T - 0.08 & \text{for Ro-Ro ships} \end{cases} \tag{2.25}$$

2.1.4 Main engine

According to the Fourth IMO GHG Study[IMO, 2020a], energy use for propulsion is the primary demand for energy across all ship types, with the exception of some vessels e.g. cruise ships and refrigerated bulk. This means the main engine propulsion is the principal source of fuel consumption and CO_2 emissions. The auxiliary engine used for electricity generation, and the boiler used for heat have a lower contribution to CO_2 emissions.

In this study, a real main engine is chosen based on the manufacturer manuals for each ship type [1]. Depending on ship type, size, length, beam and draught, one of the engines

[1] https://www.man-es.com/search-results?searchQuery=Propulsion+trends+in+tankers&indexCatalogue=default-site&wordsMode=AllWords&language=en

recommended by the manuals is chosen. The engine could be one-fuel fuel (usually MDO or HFO), or dual-fuel including a pilot fuel and a gas fuel (usually LNG). Then, by compiling a specific engine through the CEAS tool[2], a sheet of engine performance data is provided. The latter includes the specific fuel consumption ($SFOC$), as well as the specific maximum continuous rating brake power P_{SMCR} and rate of revolutions n_{SMCR}. The variation of the aforementioned parameters are given for each engine load. Usually the engine and the propeller are coupled which means that the rate of revolutions for both of them is the same.

2.2 Resistance modelling

This section presents the motivations behind resistance modelling in Sect. 2.2.1. An explanation of the forces and scaling laws implicated is then presented in Sect. 2.2.2. This section shows various approaches used to estimate calm water resistance in Sect. 2.2.3, wave-added resistance in Sect. 2.2.4, and wind-added resistance in Sect. 2.2.5. The process of the total ship resistance and the required vessel and environmental data are summarised in Sect. 2.2.6.

2.2.1 Motivations

A ship is constructed by a bare hull, appendages, namely rudder and propeller, and a superstructure hosting the bridge and containers. The parts involved in ocean-ship hydrodynamic interaction are the hull and appendages, whereas, the high superstructure of containerships in particular, is relevant when studying the effect of wind. In this thesis, the main parts of the ship were considered.

When a ship is sailing in the ocean, it faces a resistance caused by calm water that could be increased due to waves and wind. Therefore, the total ship resistance in regular waves, and wind is expressed by:

$$R_t = R_c + R_{aw} + R_{wind} \tag{2.26}$$

Ship resistance is involved in the dynamical balance of a vessel, thus crucial for predicting its performance. [Strom-Tejsen et al., 1973] shows that the optimal ship design relies on its performance in harsh weather and its ability to sustain sea speed, and that the added resistance of a ship in rough seas induces an increase of engine power of 15 to 30% with respect to the calm water. Usually at the design stage, the shipyards tend to add a sea margin expressed as a percentage of calm-water power to consider the effect of weather, which is a poor approximation. This is due to the fact that added resistance is not a constant, but depends greatly both on the sea state and the vessel speed, in a specific way for each hull's and wave encounter geometry (e.g. [Faltinsen, 1990],[Lloyd, 1998], [Tsujimoto et al., 2008], [Liu and Papanikolaou, 2016b], [Yang et al., 2018], [Park et al., 2019], [Lang and Mao, 2021]). Indeed, predicting the sustained speed which is essential for weather routing, needs a more reasonable estimation of the environmental effect. Thus, it is necessary to go beyond

[2] `https://www.man-es.com/marine/products/planning-tools-and-downloads/ceas-engine-calculations`

the concept of sea margin.

Besides ship routing, the knowledge of resistance may be used for safety requirements, comfort assessment, and special operational needs (e.g helicopters landings onboard)([Landrini, 2001], [Bertram, 2012]).

These considerations prompted elaborating a model that could estimate the effect of environmental factors on sailing operation of vessels Tab. 2.2.1.

Table 2.2: Environmental factors and physical process

Environmental factor	Physical process	Section
Calm water	friction, viscous pressure	Subsect. 2.1.1
Waves	reflection, radiation	Subsect. 2.1.2
Wind	longitudinal and lateral drag	Subsect. 2.1.3

2.2.2 Forces and scaling laws

Historically, the field of naval architecture relies on a combination of model testing and scaling laws, and three similarities must be fulfilled: geometrical, kinematic and dynamic. Geometric similarity is obtained when all the model dimensions are directly proportional to the ship's dimensions. This means that the model become a scaled version of the ship, and the scaling factor is the ratio of the length of the ship to the length of the model $\frac{L}{L_M}$. The Froude similarity law is applied to scale the other hull parameters [Heller, 2012].

Kinematic similarity implies that the velocity at any point in the flow of the model is proportional to the velocity at the homologous point in the hull by a constant scale factor. Thus, it maintains the same flow streamline pattern[3].

Dynamic similarity is achieved if we have the same ratio at model scale and full scale for the different force contributions present in the problem, and they are characterised by the following dependence on the physical parameters [Steen, 2014]:

$$\begin{aligned} \text{Inertia forces:} \quad & F_i \propto \rho V^2 L^2 \\ \text{Viscous forces:} \quad & F_v \propto \mu V L \\ \text{Gravitational forces:} \quad & F_g \propto \rho g L^3 \end{aligned} \tag{2.27}$$

The scale effects arise due to dissimilarities in force ratios between model and full-scale ships.

To reproduce geometrical and dynamical features correctly, similarity between only two dimensionless groups is necessary: The Froude number represents the ratio of inertial and gravitational forces and is associated with wave making, and the Reynolds number indicates the ratio of inertial and viscous forces [Terziev et al., 2022].

The dynamic similarity requirement applied on the ratio between inertia and gravity forces

[3] https://en.wikipedia.org/wiki/Kinematic_similarity/

gives the following relation:

$$\frac{F_i}{F_g} \propto \frac{\rho V^2 L^2}{\rho g L^3} = \frac{V^2}{gL} \tag{2.28}$$

Applied on model and full scale this requirement gives:

$$\begin{aligned} \frac{V_M^2}{gL_M} &= \frac{V_F^2}{gL_F} \\ \frac{V_M}{\sqrt{gL_M}} &= \frac{V_F}{\sqrt{gL_F}} = Fn \end{aligned} \tag{2.29}$$

Geometrical and kinematic similarity, and equality in Froude number Fn in model and full scale will therefore ensure similarity between inertia and gravity forces. Since surface waves are gravity waves, this implies that equality in Froude number Fn should give equality in the wave resistance coefficient.

Concerning the Reynolds number Re, an equal ratio between inertia and viscous forces will give:

$$\frac{F_i}{F_v} \propto \frac{\rho V^2 L^2}{\mu V L} = \frac{\rho V L}{\mu} = \frac{VL}{\nu} = Re \tag{2.30}$$

where μ is the dynamic viscosity and ν is the kinematic viscosity.

2.2.3 Calm water resistance

The main forces acting against the forward movement of the vessel result from the friction fluid-hull, ship waves making and breaking, besides other sources (e.g. air drag, appendages).

Viscous resistance

When a ship sails in calm water, a boundary layer of the fluid alters the virtual shape and length of the hull, the pressure distribution at the stern is changed and its forward component is reduced [Mermaid, 2022]. This force acting against the ship's movement is called form drag or viscous pressure drag.

In the forward part of the hull, pressure forces act normally to the surface. Instead, in the aft part of the hull the boundary layer reduces the forward acting component of pressure. This reduction in the forward acting component results in a net resistance force due to pressure acting on the hull. This resistance due to pressure is called "viscous pressure drag" or "form drag", and is sometimes also referred to as the normal component of viscous resistance. As seen in Fig. 2.8, the shape of a ship's hull impacts the magnitude of viscous pressure drag. Ships of short length and large beam (so low length to beam ratio) will have greater form drag than those of a larger length to beam ratio. Ships with fuller bow (e.g. bulkers and tankers) will have higher form drag than ships with fine bows (e.g. containership). The extent of the viscous resistance on a body depends on the type of flow it is undergoing. A typical flow pattern around a ship's hull, with laminar and turbulent flow, is shown in Fig. 2.8.

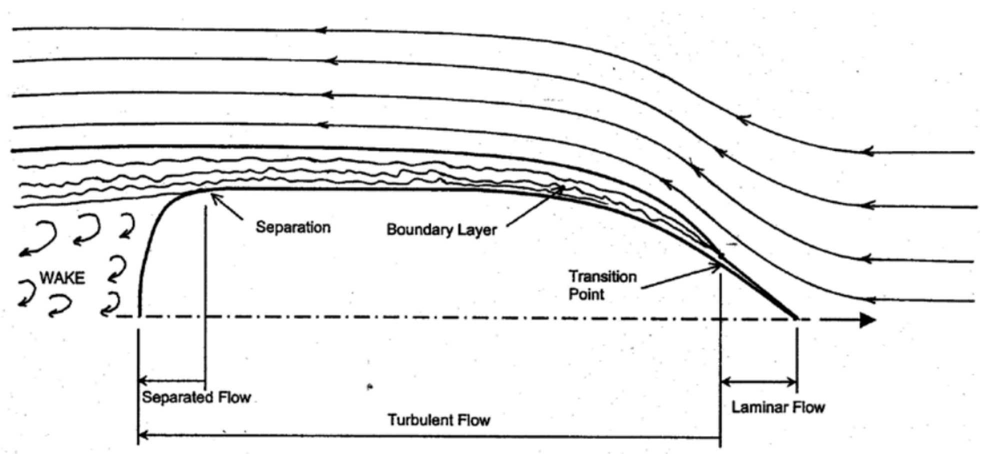

Figure 2.8: Typical water flow pattern around a ship's hull [USNA, 2020]

For a typical ship, laminar flow exists for only a very small distance along the hull. As water flows along the hull, the laminar flow begins to break down and become chaotic and well-mixed. This chaotic behavior is referred to as turbulent flow and the transition from laminar to turbulent flow occurs at the transition point shown in Fig. 2.8. Turbulent flow is characterized by the development of a layer of water along the hull moving with the ship along its direction of travel. This layer of water is called the "boundary layer." Water molecules closest to the ship are carried along with the ship at the ship's velocity. Moving away from the hull, the velocity of water particles in the boundary layer decrease, until at the outer edge of the boundary layer velocity is nearly that of the surrounding ocean. Formation of the boundary layer begins at the transition point and the thickness of the boundary layer increases along the length of the hull as the flow becomes ever more turbulent. With greater ship speed, the thickness of the boundary layer increases, and the transition point between laminar and turbulent flow moves closer to the bow, leading to an increase in frictional resistance. Mathematically, laminar and turbulent flow can be described using the Reynolds Number Re. [Newman, 1977] noted that over the range of $10^3 \leq Re \leq 3 \cdot 10^5$ the viscous flow in the boundary layer on the forebody is laminar, and beyond 10^5 the boundary-layer flow becomes turbulent.

Residual resistance

A ship moving on the surface will have a free surface (the surface of the water that is subject to zero parallel shear stress) compared to submerged hull and the resulting pressure distribution on the hull creates waves sailing on the sea surface. Waves generated by a ship are affected by its geometry and speed, and most of the energy given by the ship for making waves is transferred to water through the bow and stern parts. Indeed, two wave systems are generated by the vessel; bow and stern waves, and their interaction induces the resistance. Kelvin wave pattern, which considers the wave system formed made up of transverse waves and divergent waves, could be a reasonable representation of the actual ship wave system as being created by a number of travelling pressure points Fig. 2.9. The resulting waves carry much energy away from the ship that should be supplied to its propulsion system, so that the ship experiences it as drag. The magnitude of the wave-making resistance R_w is a function of the speed of the ship in relation to its length at the waterline. As the hull speed is related to its length and the wavelength of the wave it produces while moving through water, it is expressed as: $V[m/s] = \sqrt{\frac{L_{wl} g_0}{2\pi}}$ or $V[kn] = 1.34\sqrt{L_{wl}}[feet]$. So that if the speed-length ratio $V[kn]/\sqrt{L_{wl}}[feet]$ exceeds 1.34, R_w will increase.

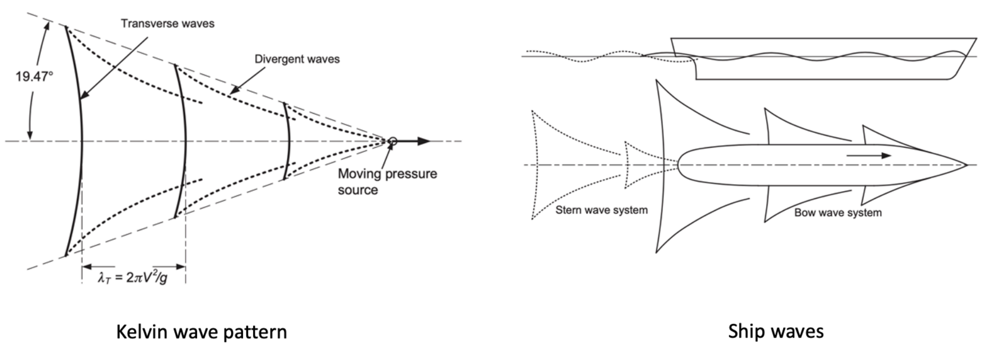

Figure 2.9: Kelvin pattern and ship waves adapted from [Molland et al., 2011]

Semi-empirical methods

To determine the calm water resistance R_c, the International Towing Tank Conference (ITTC) recommends the towing tank tests as an experimental method [ITTC, 2017d], Computational Fluid Dynamic (CFD) and potential theory for numerical computation [ITTC, 2011a], and [Holtrop and Mennen, 1982] as an empirical formula. The calm water resistance coefficient C_s depends on the speed V, and the wetted surface S of the ship, and is defined in dimentionless form by:

$$C_s = \frac{R_c}{\frac{1}{2}\rho V^2 S} \tag{2.31}$$

where R_c is the calm water resistance, ρ is the water density, and the subscript in C_s refer to still water or calm water. V is the ship speed with respect to water namely speed through water (STW), different from the speed over ground (SOG) (ship speed with respect to the ground) as explained by [Mannarini and Carelli, 2019a].

- [Holtrop and Mennen, 1982] formula

  [Holtrop and Mennen, 1982] applied multiple regression analysis based on the results of 1707 resistance measurements carried out with 147 ship models and the results of 82 trial measurements made onboard 46 new ships to elaborate an empirical formula able to predict the calm water resistance. [Holtrop, 1977] shows a survey of the parameter ranges and ship types. It was widely used in literature because of its good performance especially in the case of conventional hull (the farthest point of the bow is at the extreme front of the vessel and it then tapers down, pushing the start of the bow backwards at the waterline). The [Holtrop and Mennen, 1982] formula has been improved to cover a wider range of parameters considering ships with higher speed in [Holtrop, 1984].

  The resistance in calm water R_c calculated according to[Holtrop and Mennen, 1982] is provided by:

$$R_c = R_f(1 + k_1) + R_{app} + R_w + R_b + R_{tr} + R_a \tag{2.32}$$

R_f is the frictional resistance according to[ITTC, 1957] formula
$1 + k_1$ is the hull form factor
R_{app} is the resistance of appendages
R_w is the wave making and breaking resistance
R_b is the additional pressure resistance of bulbous bow
R_{tr} is the additional pressure resistance of immersed transom stern
R_a is the model ship correlation resistance (describing the effect of hull roughness and still-air resistance)
The viscous resistance is the dominant component of calm water resistance while the ship is sailing at low speeds, followed by the wave making resistance. At high speeds the total resistance increases as wave making resistance begins to dominate.
The viscous resistance coefficient C_v is a function of hull form, speed, and water properties. It takes into account the friction of the water on the ship as well as the influence of hull form on viscous pressure drag.

$$\begin{aligned} C_v &= \frac{R_v}{\frac{1}{2}\rho V^2 S} = C_f + k_1 C_f \\ C_f &= \frac{0.075}{(\log Re - 2)^2} \\ Re &= \frac{VL}{\nu} \end{aligned} \tag{2.33}$$

where C_f is the tangential (skin friction) component of viscous resistance, and $k_1 C_f$ is the normal (viscous pressure drag) component.

- [Kristensen and Bingham, 2017] formula
  [Kristensen and Bingham, 2017] have updated a method developed by [Guldhammer and Harvald, 1974]'s method for newer ships, to estimate the calm water resistance, and was used in several studies(e.g. [Taskar and Andersen, 2020],[Holt and Nielsen, 2021]). The empirical resistance method is based on model test results from multiple model basins to estimate residuary or residual resistance. The residuary resistance coefficient C_r is given as a function of the length-displacement ratio, prismatic coefficient C_P, and Froude number Fn. Corrections are applied based on B/T, longitudinal center of buoyancy (lcb) position and bulbous bow parameters.
  The friction resistance is calculated using the [ITTC, 1957] skin friction line as suggested by [Guldhammer and Harvald, 1974]. The skin friction arises from the friction of the water against the "skin" of the hull that is moving through it and forms a vector at each point on the surface. A skin friction line is a curve on the surface tangent to skin friction vectors.
  The residual resistance coefficient C_r and friction resistance coefficient C_f together

with the incremental resistance coefficient C_a (related to the surface roughness of the hull), and the air resistance coefficient C_{aa} give the total resistance coefficient in calm water.

$$\begin{aligned}
C_t &= C_f + C_r + C_a + C_{aa} \\
C_f &= \frac{0.075}{(\log Re - 2)^2} \\
C_r &= f(M, C_p, Fn) \\
C_a &= \max(-0.1; 0.5 \log \Delta - 0.1 \log \Delta^2) \\
C_{aa} &= f(TEU, ship_type)
\end{aligned} \tag{2.34}$$

where Δ is displacement mass of ship, and M is the length-displacement ratio. The expression for C_r provided in [Kristensen and Bingham, 2017] holds for $Fn \leq 0.33$ and $B/T = 2.5$. It reads:

$$\begin{aligned}
10^3 C_r &= E + G + H + K \\
E &= (A_0 + 1.5 Fn^{1.8} + A_1 Fn^{N_1})(0.98 + \frac{2.5}{(M-2)^4}) + (M-5)^4 (Fn - 0.1)^4 \\
A_0 &= 1.35 - 0.23M + 0.012M^2 \\
A_1 &= 0.0011 M^{9.1} \\
N_1 &= 2M - 3.7 \\
G &= \frac{B_1 B_2}{B_3} \\
B_1 &= 7 - 0.09M^2 \\
B_2 &= (5C_p - 2.5)^2 \\
B_3 &= (600(Fn - 0.315)^2 + 1)^{1.5} \\
H &= \exp\left(80(Fn - (0.04 + 0.59C_p) - 0.015(M - 5))\right) \\
K &= 180 Fn^{3.7} \exp\left(20C_p - 16\right)
\end{aligned} \tag{2.35}$$

The resistance coefficient Cr calculated according to the formulas above is given without correction in [Kristensen and Bingham, 2017]. [Guldhammer and Harvald, 1974] gives additional corrections for the position of lcb, shape or hull form, B/T deviation from 2.5 (Cr above is given a breadth-draft ratio deviation $B/T = 2.5$), and bulbous bow shape and size. [Kristensen and Bingham, 2017] does not consider the lcb correction, and includes the B/T deviation as follows:

$$\Delta Cr_{B/T} = 0.16(\frac{B}{T} - 2.5)10^{-3} \tag{2.36}$$

A hull shape correction is applied when the aft or the fore body is extremely U or V shaped, and expressed by Eq. 2.37:

$$\Delta Cr_{form}10^3 = \begin{cases} -0.1 & \text{for extreme U at fore body} \\ 0.1 & \text{for extreme U at aft body} \\ 0.1 & \text{for extreme V at fore body} \\ -0.1 & \text{for extreme V at aft body} \end{cases} \tag{2.37}$$

[Kristensen and Bingham, 2017] assumed that the bulb correction depends only on Fn, and based on the analysis of model test results of ships with bulbous bow, an approximation is elaborated for tankers and bulk carriers:

$$\Delta Cr_{bulb} = \begin{cases} \max(-0.4; -0.1 - 1.6Fn) & \text{for tanker and bulk carrier} \\ (250Fn - 90)\frac{Cr_{\text{nobulb}}}{100} & \text{for container ship} \end{cases} \tag{2.38}$$

The air resistance is due to the movement of the ship through the air and not due to wind. The added resistance due to wind will be introduced later on in Sect. 2.1.3. The air resistance coefficient C_{aa} is defined by:

$$C_{aa} = \frac{R_{air}}{\frac{1}{2}\rho_w V^2 S} \tag{2.39}$$

where R_{air} is the air resistance.

Based on the analysis of C_{aa} for several ship types, [Kristensen and Bingham, 2017] suggested the following values:

$$C_{aa} \cdot 10^3 = \begin{cases} 0.28 \cdot TEU^{-0.126} & \text{for container ships} \\ 0.07 & \text{for small, handysize and handymax tankers} \\ 0.05 & \text{for panamax, aframax, and suezmax tankers} \\ 0.04 & \text{for VLCC} \end{cases} \tag{2.40}$$

2.2.4 Wave-added resistance

Superposition principle

The linear theory can describe the wave-induced motions and loads on semi-submersible ships or other off-shore structures. Non-linear effects are considerable only in severe sea states to describe the horizontal motions of the ship. When the vessel encounters the incident regular waves of amplitude ζ_a with a small wave steepness, linear theory means that the unsteady motions and forces are proportional to ζ_a, and the wave drift force (the added resistance) is proportional to the square of ζ_a. In this case the seakeeping problem can be dealt with as the superposition of two sub-problems: diffraction and radiation:

- Diffraction

  This refers to the forces experienced by the vessel due to the incoming waves, with its hull constrained not to oscillate. These loads, commonly known as exciting loads, are composed of Froude-Krylov forces due to the pressure field of the incident wave, and diffraction forces [Faltinsen, 1990], as illustrated in Fig. 2.10.

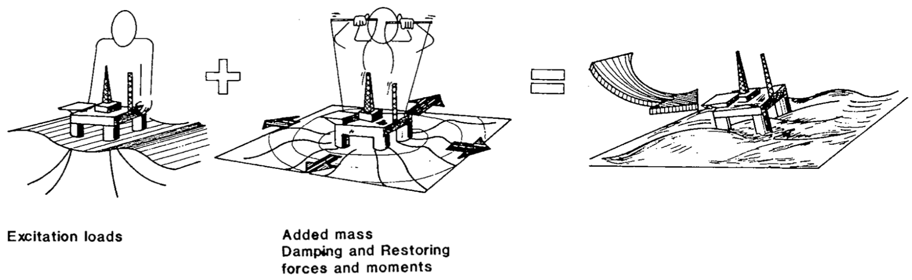

Figure 2.10: Superposition of wave excitation, added mass, damping and restoring loads [Faltinsen, 1990]

- Radiation

  The forces and moments on the hull when the ship is free to oscillate in any degree of freedom (Translational motions: surge, sway and heave. Rotational motions: roll, pitch, yaw) Fig. 2.11, with the wave excitation frequency and amplitude and without incoming waves. The hydrodynamic loads are identified as added mass, damping and restoring contributions [Faltinsen, 1990] Fig. 2.10. The added mass refers to the amount of fluid accelerated with the ship[Newman, 1977]. The restoring forces will follow from hydrostatic and mass considerations when the ship is freely floating. While, the damping means the eddy damping due to pressure variations on the hull, and wave damping due to free-surface waves [Jaouen et al., 2011].

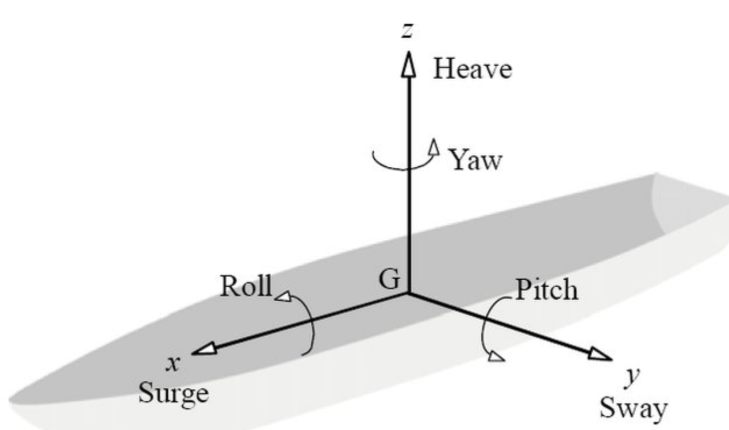

Figure 2.11: Six degrees of freedom for ship motions [Tanaka, 2018]

Due to the principle of linear superposition, the radiation and diffraction forces can be summed to give the total hydrodynamic forces. The unsteady forces due to ship motions and ocean waves induce a steady force, namely the drift force which acts as an added force exerted on the moving ship and must be overcome to keep the desired speed. Therefore, the added resistance could be defined as the time average of the longitudinal (projection along the bow-stern axis of the hull) force on a ship in waves once the calm water resistance has been subtracted ([Newman, 1977], [Söding and Shigunov, 2015]). The transverse and rotational forces are relevant only while studying the maneuvering performance of a ship in a seaway, and have lower concern in dealing with speed-power performance of a ship in rough seas [Liu and Papanikolaou, 2020].

ITTC's recommendations for estimating the added resistance due to waves are divided according to the type of approach: experimental, numerical computation and semi-empirical [ITTC, 2017a].

Experimental approach

The experimental approach was used in several studies to develop a benchmark basis to validate the results of the numerical approach.

In case of head seas, ([Gerritsma and Beukelman, 1972]; [Ström-Tejsen et al., 1973]) have measured the added resistance for various models of the Series 60. [Kashiwagi, 2013] evaluated the added resistance based on the captive model test and wave analysis using a towing tank model test for a modified blunt and slender Wigley hull. [GUO and STEEN, 2011] focussed on measuring the added resistance in short-wave for the KVLCC2 tanker. [Sadat-Hosseini et al., 2013] evaluated the added resistance using experimental fluid dynamics (EFD). In [Park et al., 2016], a series of towing-tank experiments for ship motion and added resistance at four draught values was carried out in head sea conditions, in parallel with two different seakeeping analyses (the strip method and Rankine panel method).

In oblique seas, [Fujii and Takahashi, 1975] measured the resistance in a towing tank for the S175 container ship. Recently, [Sadat-Hosseini et al., 2015] has studied experimentally (EFD) and numerically (Potential flow) the added resistance for the KCS containership at different headings. [Sprenger et al., 2016] made a series of experimental tests at MARINTEK by varying the encounter angle.[Park et al., 2019] has performed tank experiments in a SSPA seakeeping basin and estimated the added resistance by substructing the thrust in calm water from the one in waves.

Most experimental results refer to head seas conditions. The lack of experimental data on ship resistance is particularly notable in the case of arbitrary waves heading, and the reason would be that only a number of basins in the world have the convenient dimensions and the necessary technology to carry out such experiments.

Experimental tests are considered an accurate approach though they are very expensive and time consuming.

Numerical approach

There are several methods for the numerical computation of the wave-added resistance, such as potential flow, computational fluid dynamic (CFD), RANS (Reynolds-averaged Navier-Stokes), Rankine panel method, Near-field and Far-field methods.

To compute the wave drift force on a floating body (the vessel) moving with a steady forward speed, in linear regime, the Near-field method is used in the diffraction problem by integrating the second-order pressure terms on the surface of the body, e.g.[Faltinsen, 1980] who used this approach to develop an asymptotic formula in short waves (where the ratio of wave length to ship length $\lambda/L_{pp} < 0.5$).
A Far-field method is used to derive a solution for the radiation problem by applying a conservation of energy or momentum. [Maruo, 1960]) developed a formulation for the added resistance using a far-field equation for either two- or three-dimensional floating objects and the Kochin function, based on the slender-body theory. Similarly [Newman, 1977] used the far-field approach and the conservation of moments based on the slender-body approximation, to estimate the added resistance.
Recently, [Amini-Afshar and Bingham, 2021] has applied a far-field formulation in the context of the Salvesen–Tuck–Faltinsen (STF), [Salvesen et al., 1970] strip theory, and employed the Kochin function to express the wave kinematics in the far-field. The performance of this method to predict wave-added resistance is good at low speeds, but deteriorates while increasing. Generally, the Far-field method and Near-field methods usually overestimate the peak of the added resistance and notably underestimate the added resistance in short waves [Liu and Papanikolaou, 2016a]
[Wang et al., 2022] used the potential flow theory and panel method to calculate the ship motion responses and the wave added resistance of an S175 container ship sailing in head, bow and quartering waves. While they found good agreement with experimental data, the potential flow ignores the viscosity of the fluid, which could induce large errors at the peak (in the interval of intense motion).
[Park et al., 2019] has compared experimental results of added resistance to the strip methods and the 3-dimensional Rankine panel method, and found that in oblique seas the peak frequency of the motion response moves and the radiation component of the added resistance increases in short waves.
[Söding and Shigunov, 2015] has used a newly developed potential flow method, a Rankine source method, a strip method, and by RANS (Reynolds-averaged Navier-Stokes) equations solvers for ten ships, and concludes that the potential methods, Euler and RANS computations are not yet accurate enough in short waves. However, the Rankine source method seems to give reasonable results.

Semi-empirical approach

The semi-empirical approach combines ship hydrodynamic theory and experimental data. Experimental methods, and CFD simulations secondly, are the most reliable approaches for determining the resistance. However, both techniques are very costly in terms of either laboratory time or computational effort.
The prediction of wave-added resistance is increasingly needed for evaluating ship performance in rough seas. The semi-empirical approach is classified as having high practicality

[ITTC, 2017a] to catch the physical phenomena of added resistance, using a simplified formula with the minimum of vessel parameters.

Following the presentation made at the beginning of this subsection, the wave resistance is decomposed into: the added resistance in short waves due to wave diffraction of the incident waves on the ship hull, and added resistance induced by wave radiation due to ship motions [Ström-Tejsen et al., 1973].

$$R_{aw} = R_{awr} + R_{awm} \tag{2.41}$$

The energy distribution among these two components is dependent on the ratio of incident wave length to ship length λ/L Fig. 2.12. For wave lengths up to half of the ship's length, the main contributor to resistance is the reflection of incident waves at the ship's hull. In the case of wave length being around ship length, the ship's heave and pitch motion mainly account for a larger share of the wave-added resistance.

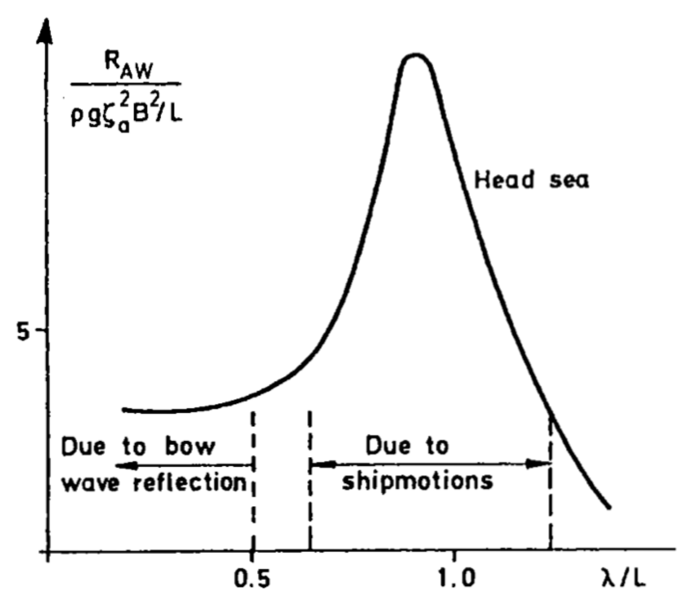

Figure 2.12: Typical wave length dependence of added resistance of a ship at moderate speed at head seas [Faltinsen, 1990]

- Faltinsen formula for oblique short waves

  Due to the increasing sizes of the ships, the region of smaller values of the λ/L ratio is gaining increasing attention. This makes the accurate prediction of the added resistance in short waves more necessary today. [Faltinsen, 1980] proposed an asymptotic formula for the added resistance of wall-sided hull forms in short waves of arbitrary heading, using the Near-Field method by integrating the pressure over the hull surface using an approximate velocity potential near the bow. He found that the limit of short wave-added resistance can be expressed as Eq. 2.42:

$$\begin{aligned} R_{awr-Fal} &= \int_L \bar{F}_e \sin i_E dl \\ \bar{F}_e &= \frac{1}{2}\rho g_0 \zeta_a^2 \left[\sin^2(i_E - \alpha) + \frac{2\omega V}{g_0}(1 - \cos i_E \cos(i_E - \alpha))\right] \end{aligned} \tag{2.42}$$

where $\zeta_a = H_s/2$ is the wave amplitude, g_0 is the gravitational acceleration, $\bar{F}_e$ is the force per unit length, i_E is the slope of segment of the ship's waterline or the angle of entrance, ω is the circular wave frequency, and α is the wave heading angle.

In reference to Fig. 2.13, the integration is performed on the non-shaded part of the hull.

Since this formula is based on the assumption of vertical side at the waterplane, it works well for fuller hull form (U-shaped transverse section) e.g for bulkers and tankers, but fails in the case of more V-shaped sections such as those of hull containerships [Liu et al., 2015]. [Yang et al., 2018] modified the [Faltinsen, 1980] formula to consider the finite draught of ships, the local steady flow velocity, and the shape above the waterline.

- NMRI (National Maritime Research Institute) formula for oblique short waves

  NMRI's empirical formula was initially proposed by [Fujii and Takahashi, 1975] for diffraction dominated wave added resistance based on the theoretical solutions from [Ursell, 1947] by adopting some complementary coefficients for the drifting force formula of a fixed vertical cylinder. The same as [Faltinsen, 1980], [Fujii and Takahashi, 1975] formula give good prediction for blunt hulls, however poor results are obtained for slender hull [Seo et al., 2014].

  [Tsujimoto et al., 2008] made a further correction to the [Fujii and Takahashi, 1975] formula to estimate the added resistance for a fine or slender and high-speed ship in oblique seas. The NMRI formula examines the effect of draft and frequency (α_T), and comprises the bluntness coefficient B_f determined from the hull shape's above the waterline and the incident wave direction, and the effect of advance speed $(1 + \alpha_U)$ accordingly. The added resistance due to diffraction takes the following form:

$$\begin{aligned} R_{awr} &= \frac{1}{2}\rho g_0 \zeta_a^2 B B_f \alpha_T (1+\alpha_U) \\ B_f &= \frac{1}{B}\left[\int_I \sin^2(\alpha + i_E)\sin(i_E)dl + \int_{II} \sin^2(\alpha - i_E)\sin(i_E)dl\right] \\ \alpha_T &= \frac{\pi^2 I_1^2(kT)}{\pi^2 I_1^2(kT) + K_1^2(kT)} \\ C_U &= \max(-310B_f + 68, 10) \\ 1+\alpha_U &= 1 + C_U\sqrt{F_n} \end{aligned} \tag{2.43}$$

  where k is the wave number of regular waves, T is the draught, I_1 and K_1 are the first order modified Bessel functions of the first and second kinds, respectively. The integration is performed over the non-shaded port part (I) and (II) the non-shaded starboard part Fig. 2.13.

- STA2 for bow seas

  STAwave-1 is a simplified correction method for ships with limited heave and pitch during the speed runs. It was developed by the Sea Trial Analysis-Joint Industry

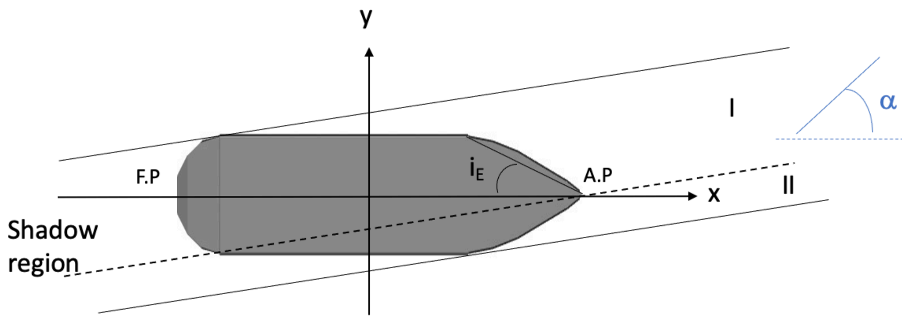

Figure 2.13: Sketch of coordinate system for wave reflection

Project (STA-JIP), to estimate the added resistance in short waves and restricted to waves at the bow sector. A further empirical correction was made to approximate the transfer function considering both reflection and radiation, and was called STAwave-2[ITTC, 2017c]. It is valid for bow seas ($|\alpha| \leq 45°$). The following restrictions hold; $50m \leq L_{pp} \leq 400m$, $4 < \frac{L_{pp}}{B} < 9$, $2.2 < \frac{L_{pp}}{T} < 9$, $0.1 < Fn < 0.3$, $0.39 < C_B < 0.9$. The wave-added resistance reads:

$$\begin{aligned}
R_{aw} &= R_{awr} + R_{awm} \\
R_{awr} &= \frac{1}{2}\rho g_0 \zeta_a^2 B \alpha_T \left[0.692(\frac{V}{\sqrt{T g_0}})^{0.769} + 1.81 C_B^{6.95}\right] \\
R_{awm} &= 4\rho g \zeta_a^2 \frac{B^2}{L_{pp}} \bar{\omega}^{b_1} exp[\frac{b_1}{d_1}(1 - \bar{\omega}^{d_1})] a_1 a_2 \\
a_1 &= 60.3 C_B^{1.34} \\
a_2 &= F_n^{1.5 C_B} \exp(-3.5 Fr) \\
b_1 &= \begin{cases} 11.0 & \text{for } \bar{\omega} < 1 \\ -8.5 & \text{elsewhere} \end{cases} \\
d_1 &= \begin{cases} 14.0 & \text{for } \bar{\omega} < 1 \\ -566[\frac{L_{pp}}{B}]^{-2.66} & \text{elsewhere} \end{cases}
\end{aligned} \tag{2.44}$$

where the draught coefficient α_T is the same as in Eq. 2.43. The added resistance in long waves R_{awm} is based on the semi-empirical method proposed by [Jinkine and Ferdinande, 1974]. It was derived from experimental data of fast cargo ships with fine hull form, and takes the following form:

$$\begin{aligned}
R_{awm} &= 4\rho g_0 \zeta_a^2 B^2/L_{pp} r_{aw} \\
r_{aw} &= a_1 a_2 \bar{\omega}^{b_1} \exp\left[\frac{b_1}{d_1}(1-\bar{\omega}^{d_1})\right] \\
a_1 &= 900\left(\frac{k_{yy}}{L_{pp}}\right)^2 \\
a_2 &= Fn^{1.5}\exp(-3.5Fn) \\
\bar{\omega} &= \sqrt{\frac{L_{pp}}{g}}\sqrt[3]{\frac{k_{yy}}{L_{pp}}}Fn^{0.143}\omega/1.17 \\
b_1 &= \begin{cases} 11.0 & \text{for } \bar{\omega} < 1 \\ -8.5 & \text{elsewhere} \end{cases} \\
d_1 &= \begin{cases} 14.0 & \text{for } \bar{\omega} < 1 \\ -14.0 & \text{elsewhere} \end{cases}
\end{aligned} \tag{2.45}$$

where a_1 is the amplitude factor, a_2 is the speed correction factor, b_1 and d_1 are the slope adjustment factors, and $\bar{\omega}$ is the ocean wave frequency factor.

- NTUA (National Technical University of Athens) formula in head seas

  [Liu and Papanikolaou, 2016b] from NTUA gave an estimation of the wave-added resistance due to reflection based on the [Faltinsen, 1980] formula (e.g. simplifying B_f, approximation the flare angle effect).

  The wave-added resistance due to motions in NTUA formula is based on modifying the [Jinkine and Ferdinande, 1974] formula. [Liu and Papanikolaou, 2016a] further tuned a_1 by fitting it to the available experimental data to adjust it for slender ships. The speed correction factor a_2 has been extended to the speed range $Fn \in [0, 0.3]$, and the resonance position was modified accordingly considering the effect of the longitudinal radius of gyration k_{yy} (square root of the ratio of total rotational inertia to mass) and ship speed. The slope adjustment coefficients (b_1 and d_1) were also calibrated with respect to the block coefficient and the frequency term.

  [Liu and Papanikolaou, 2016b] distinguished two Fn regimes. At higher Fn the formula is less accurate in fitting observations. This happens especially when k_{yy} differs from 0.25 and for reduced wavelength $\lambda/L_{pp} < 0.3$. In particular, this is noted for the HSVA cruise, KVLCC2 tanker and DTC container ship[Lang and Mao, 2020]. It is also observed that the resonance frequency drifts across $\lambda/L_{pp} = 1$ position as Fn increases. However, this is affected by k_{yy} value as well.

  The NTUA formula reads:

Table 2.3: NTUA Method

$$R_{aw} = R_{awr} + R_{awm}$$

$$R_{awr} = \frac{2.25}{2}\rho g B \zeta_a^2 \alpha_T \sin^2 E \left(1 + 5\sqrt{\frac{L_{pp}}{\lambda}}Fn\right)\left(\frac{0.87}{C_B}\right)^{1+4\sqrt{Fn}}$$

$$R_{awm} = 4\rho g \zeta_a^2 B^2/L_{pp}\bar{\omega}^{b_1} exp[\frac{b_1}{d_1}(1-\bar{\omega}^{d_1})]a_1 a_2$$

$$\alpha_T = \frac{\pi^2 I_1^2(k_e T)}{\pi^2 I_1^2(k_e T) + K_1^2(k_e T)}$$

$$E = \arctan B/2L_E$$

$$a_1 = 60.3 C_B^{1.34}(\frac{0.87}{C_B})^{1+Fn}$$

$$a_2 = \begin{cases} 0.0072 + 0.1676Fn & \text{for } Fn < 0.12 \\ Fn^{1.5}\exp(-3.5Fn) & \text{for } Fn \geq 0.12 \end{cases}$$

$$\bar{\omega} = \begin{cases} \frac{\sqrt{L_{pp}/g}\sqrt[3]{k_{yy}}0.05^{0.0143}}{1.17}\omega & \text{for } Fn < 0.05 \\ \frac{\sqrt{L_{pp}/g}\sqrt[3]{k_{yy}}Fn^{0.0143}}{1.17}\omega & \text{for } Fn \geq 0.05 \end{cases}$$

$$b_1 = \begin{cases} 11.0 & \text{for } \bar{\omega} < 1 \\ -8.5 & \text{elsewhere} \end{cases}$$

$$d_1 = \begin{cases} 14.0 & \text{for } \bar{\omega} < 1, C_B \leq 0.75 \\ -566[\frac{L_{pp}}{B}]^{-2.66}.6 & \text{for } \bar{\omega} \geq 1, C_B \leq 0.75 \\ 566[\frac{L_{pp}}{B}]^{-2.66} & \text{for } \bar{\omega} < 1, C_B > 0.75 \\ -566[\frac{L_{pp}}{B}]^{-2.66}.6 & \text{for } \bar{\omega} \geq 1, C_B > 0.75 \end{cases}$$

- CTH (Chalmers Tekniska Högskola) formula in head and oblique seas

  [Lang and Mao, 2020] from CTH has further tuned the NMRI semi-empirical model in short waves. A wave length correction factor depending on λ/L_{pp} ratio was introduced, and the draft coefficient α_T was modified by replacing the adimensional wave number k by the encountered one k_e. The latter adjustments were done to improve the accuracy of the formula in the very short waves ($\lambda/L_{pp} < 0.3$).

  The amplitude factor a_1 was modified into a continuous function of both C_B and Fn. The speed correction a_2 was extended to the speed span of $0 \leq Fn \leq 0.3$ considering the variation of k_{yy} depending on different types of ship. The $\bar{\omega}$ modified frequency takes into account geometrical parameters and Fn.

  The CTH method in head seas is as follows:

Table 2.4: CTH Method

$$R_{aw} = R_{awr} + R_{awm}$$

$$R_{awr} = \frac{1}{2}\rho g \zeta_a^2 B B_f \alpha_T (1+\alpha_U) \left(\frac{0.19}{C_B}\right) \left(\frac{\lambda}{L_{pp}}\right)^{Fn-1.11}$$

$$B_f = 2.25 \sin^2 E \ where \ E = \arctan B/2L_E$$

$$1+\alpha_U = 1 + C_U Fn \ where \ C_U = \max(-310B_f + 68.10)$$

$$\alpha_T = 1 - e^{-2k_e T} \ where \ k_e = k(1+\Omega\cos\beta)^2 \ and \ \Omega = \frac{\omega V}{g}$$

$$R_{awm} = 4\rho g \zeta_a^2 B^2 / L_{pp} \bar{\omega}^{b_1} exp[\frac{b_1}{d_1}(1-\bar{\omega}^{d_1})] a_1 a_2$$

$$a_1 = 60.3 C_B^{1.34} \left(\frac{1}{C_B}\right)^{1+Fn}$$

$$a_2 = \begin{cases} 0.0072 + 0.24Fn & \text{for } Fn < 0.12 \\ Fn^{-1.05C_B+2.3} \exp((-2 - \lceil \frac{k_{yy}}{0.25} \rceil - \lfloor \frac{k_{yy}}{0.25} \rfloor) Fn) & \text{for } Fn \geq 0.12 \end{cases}$$

$$\bar{\omega} = \begin{cases} \frac{\sqrt{L_{pp}/g} \sqrt[c_1]{k_{yy}} 0.05^{0.0143}}{1.09 + \lceil \frac{k_{yy}}{0.25} \rceil 0.08} \omega & \text{for } Fn < 0.05 \\ \frac{\sqrt{L_{pp}/g} \sqrt[c_1]{k_{yy}} Fn^{0.0143}}{1.09 + \lceil \frac{k_{yy}}{0.25} \rceil 0.08} \omega & \text{for } Fn \geq 0.05 \end{cases}$$

$$where \ c_1 = 0.4567 \frac{C_B}{k_{yy}} + 1.689$$

$$b_1 = \begin{cases} (19.77 \frac{C_B}{k_{yy}} - 36.39) / \lceil \frac{k_{yy}}{0.25} \rceil & \text{for } \bar{\omega} < 1, C_B < 0.75 \\ 11 / \lceil \frac{k_{yy}}{0.25} \rceil & \text{for } \bar{\omega} < 1, C_B \geq 0.75 \\ -12.5 / \lceil \frac{k_{yy}}{0.25} \rceil & \text{for } \bar{\omega} \geq 1, C_B < 0.75 \\ -5.5 / \lceil \frac{k_{yy}}{0.25} \rceil & \text{for } \bar{\omega} \geq 1, C_B \geq 0.75 \end{cases}$$

$$d_1 = \begin{cases} 14 & \text{for } \bar{\omega} < 1, C_B < 0.75 \\ 566 \left(\frac{L_{pp}}{B}\right)^{-2.66} .2 & \text{for } \bar{\omega} < 1, C_B \geq 0.75 \\ -566 \left(\frac{L_{pp}}{B}\right)^{-2.66} .6 & \text{elswhere} \end{cases}$$

Recently [Lang and Mao, 2021] proposed a model for speed loss prediction based on an extension of the CTH method to oblique seas. The new formula aims to capture the trend of wave-added resistance seen in the experimental studies (e.g. by [Valanto and Hong, 2015]). To this end a $cos\alpha$ factor is introduced which is mixed with the Fn. An angle-dependent correction factor $C_\omega(\alpha)$ is introduced for dealing with the location of the resonance. Finally, for the wave-added resistance due to motions R_{awm}, an exponential factor depending on wave angle of attack and Fn is introduced. The CTH formula in oblique seas reads:

$$\begin{aligned} R_{aw}(\omega|V,\alpha) &= R_{awr}(\omega|V,\alpha) + R_{awm}(\omega|V,\alpha) \\ R_{awr}(\omega|V,\alpha) &= \begin{cases} R_{awr}(\omega|V,0) \cdot Fn^{(\lfloor \cos\alpha \rfloor - \lceil \cos\alpha \rceil) Fn} \cos\alpha & \text{for } 0 \leq \alpha \leq \frac{\pi}{2} \\ R_{awr}(\omega|V,0) \cdot Fn^{-1.5(\lfloor \cos\alpha \rfloor - \lceil \cos\alpha \rceil) Fn} \cos\alpha & \text{for } \frac{\pi}{2} < \alpha \leq \pi \end{cases} \\ R_{awm}(\omega|V,\alpha) &= R_{awm}(\omega|V,0) \cdot e^{-(\frac{\alpha}{\pi})^{4\sqrt{Fn}}} + \rho g_0 \zeta^2 B^2 / Lpp \left[\frac{\lambda}{B} \cdot \max(\cos\alpha, 0.45)\right]^{-6Fn} \sin\alpha \end{aligned} \quad (2.46)$$

where $R_{awr}(\omega|V,0)$ and $R_{awm}(\omega|V,0)$ refer to wave-added resistance due to reflection and motions and head seas mentioned in Tab. 2.4.

$$\bar{\omega}(\alpha) = \bar{\omega}(0)C_{\omega}(\alpha) \tag{2.47}$$

C_{ω} is provided by the following table as a function of the angle of attack α.

Table 2.5: Encountered frequency correction factor for various heading angles[Lang and Mao, 2021]

α	0	30	45	60	90	120	135	150	180
$C_{\omega}(\alpha)$	1	0.925	0.9	0.8	0.75	0.7	0.7	0.7	0.6

When a vessel sails it encounters waves from different angles. In this study, the waves coming at 0° are defined as the head seas and at 180° as following seas.

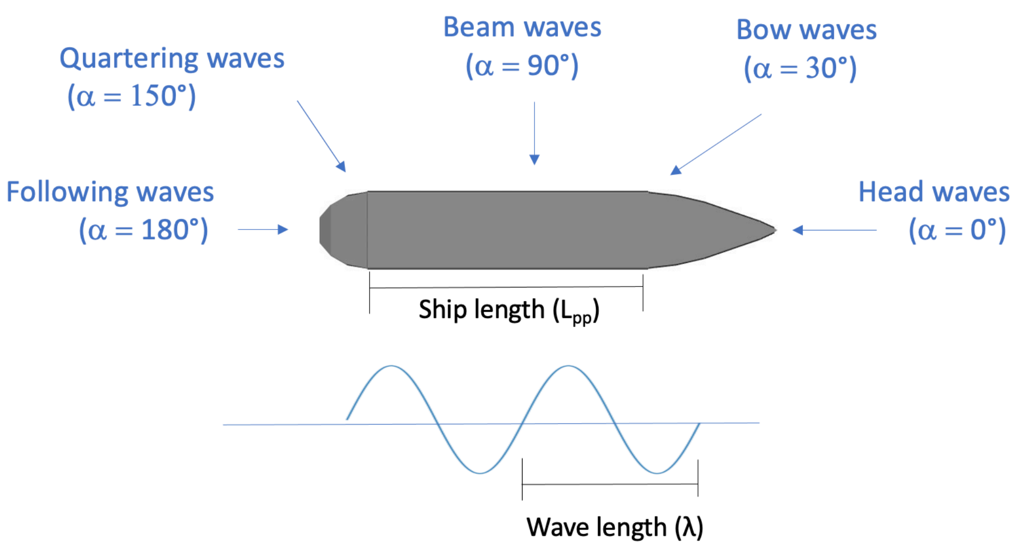

Figure 2.14: Geometry of ship-waves interaction

2.2.5 Wind-added resistance

According to [ITTC, 2017e], the added resistance due to wind is computed as:

$$R_{wind} = \frac{1}{2}\rho C_{wind}(\psi_{WR})A_{XV}V_{WR}^2 \tag{2.48}$$

where C_{wind} is the wind drag coefficient as a function of the apparent wind angle ψ_{WR}, A_{XV} is the frontal or the maximum transverse area of the ship, and V_{WR} is the magnitude of apparent wind speed. The relative wind vector is given by:

$$\mathbf{V_{WR}} = \mathbf{V_{wind}} - \mathbf{V} \tag{2.49}$$

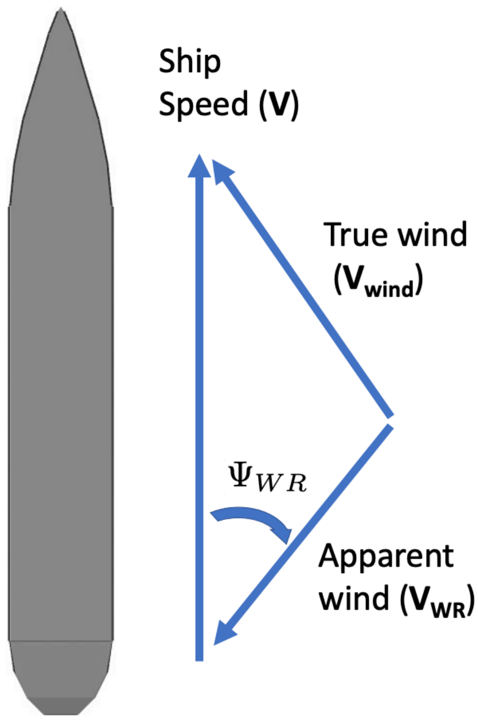

Figure 2.15: Apparent wind speed

To estimate the wind drag coefficient, it is possible to use various methods such as wind tunnel tests, viscous flow CFD simulations, or an empirical formula [ITTC, 2017b]. A general regression formula to estimate longitudinal and lateral wind forces based on model tests in wind tunnels for various ships has been developed by [Fujiwara et al., 2005] as follows:

For $\psi_{WR} \neq 90°$:

$$\begin{aligned} C_{wind} = C_{LF} \cos\psi_{WR} + C_{XLI}(\sin\psi_{WR} - \frac{1}{2}\sin\psi_{WR}\cos\psi_{WR}^2)\sin\psi_{WR}\cos\psi_{WR} \\ + C_{ALF}\sin\psi_{WR}\cos{\psi_{WR}}^3 \end{aligned} \tag{2.50}$$

For $0 \leq \psi_{WR} < 90°$:

$$\begin{aligned} C_{LF} &= \beta_{01} + \beta_{11}\frac{A_{YV}}{L_{oa}B} + \beta_{12}\frac{C_{MC}}{L_{oa}} \\ C_{XLI} &= \delta_{10} + \delta_{11}\frac{A_{YV}}{L_{oa}h_{BR}} + \delta_{12}\frac{A_{XV}}{Bh_{BR}} \\ C_{ALF} &= \epsilon_{10} + \epsilon_{11}\frac{A_{OD}}{L_{YV}} + \epsilon_{12}\frac{B}{L_{oa}} \end{aligned} \tag{2.51}$$

For $90 \leq \psi_{WR} < 180°$:

$$\begin{aligned} C_{LF} &= \beta_{20} + \beta_{21}\frac{B}{L_{oa}} + \beta_{12}\frac{H_C}{L_{oa}} + \beta_{23}\frac{A_{OD}}{L_{oa}^2} + \beta_{24}\frac{A_{XV}}{B^2} \\ C_{XLI} &= \delta_{20} + \delta_{21}\frac{A_{YV}}{L_{oa}h_{BR}} + \delta_{22}\frac{A_{XV}}{A_{YV}} + \delta_{23}\frac{B}{L_{OA}} + \delta_{24}\frac{A_{XV}}{BH_{BR}} \\ C_{ALF} &= \epsilon_{20} + \epsilon_{21}\frac{A_{OD}}{L_{YV}} \end{aligned} \tag{2.52}$$

For $\psi_{WR} = 90°$:

$$C_{wind} = \frac{1}{2}(C_{wind|\psi_{WR}=90-\mu} + C_{wind|\psi_{WR}=90+\mu}) \tag{2.53}$$

The cross-sectional areas A_{OD}, A_{YV}, and A_{XV} used in the formulas above are illustrated Fig. 2.6. In particular, A_{OD} is the lateral projected area of superstructures etc. on deck, C_{MC} is the horizontal distance from midship section to centre of lateral projected area A_{YV}, h_{BR} is the height of top of superstructure (bridge etc.), h_C is the height from waterline to centre of lateral projected area A_{YV}, and μ is the smoothing range equal to 10°.
Non-dimensional parameters used in this formula are in Tab. 2.2.5.

Table 2.6: Non-dimensional parameters used in [Fujiwara et al., 2005] regression formula

	i	j				
		0	1	2	3	4
β_{ij}	1	0.922	-0.507	-1.162	-	-
	2	-0.018	5.091	-10.367	3.011	0.341
δ_{ij}	1	-0.458	-3.245	2.313	-	-
	2	1.901	-12.727	-24.407	40.31	5.481
ϵ_{ij}	1	0.585	0.906	-3.239	-	-
	2	0.314	1.117	-	-	-

2.2.6 Total ship resistance

As shown in Eq. 2.26, the total resistance is formed from the calm water resistance and the additional resistance due to waves and wind. The required ship parameters and environmental variables for the ship resistance prediction are summarised in Fig. 2.16:

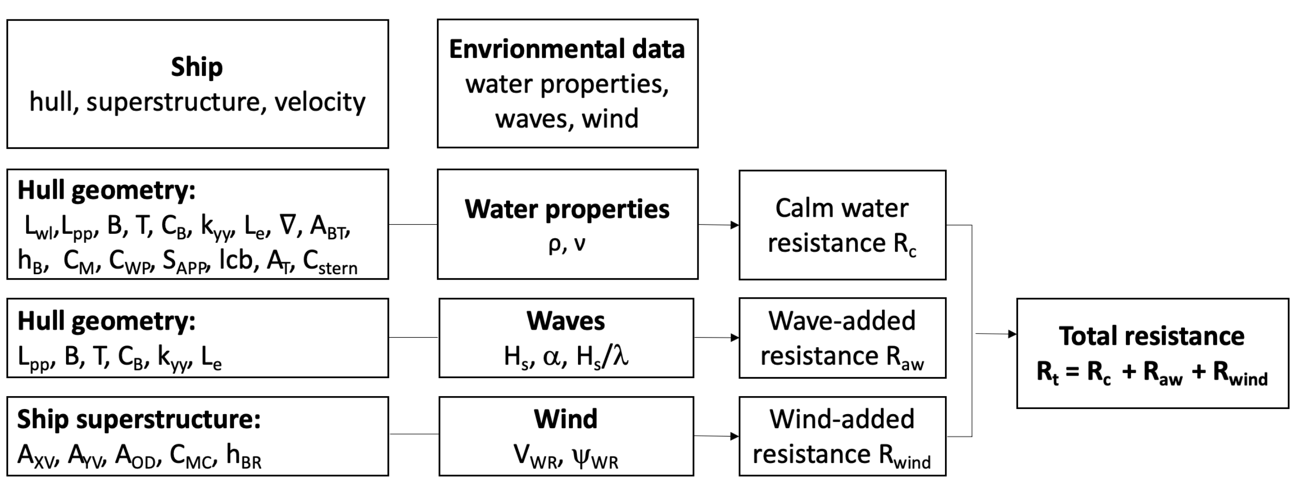

Figure 2.16: Process ship resistance computation

Thus, a total of more than 20 static parameters and two dynamic vector fields (wave and wind) is needed for estimating the total resistance. The dynamic fields depend on both two spatial coordinates and time.

2.3 Power and speed loss modelling

The estimation of the delivered power is a key component in computing the sustained speed. The latter is essential for a voyage planning algorithm, in particular ship routing. In other research areas, the goal is rather to explore hull and propulsion parameters to obtain a superior performance [Diez and Peri, 2010].

Here instead, they are part of a given configuration used to assess the speed sustained by a specific ship. This will then be used in the *bateau* module for providing inputs to the weather routing model VISIR in Chap. 4. Various methods of computing the required power in rough seas are explained in Sect. 2.2.1, and the procedure of estimating the relative speed loss is presented in Sect. 2.2.2.

2.3.1 Power prediction

At low Froude numbers the resistance is expected to increase proportionaly to the speed squared. This holds for the calm water resistance in Eq. 2.31. As the power is the product of force and velocity of the body it acts upon, the required power and fuel consumption become proportional to the cubic of the speed, $P \propto V^3$ which is defined as the propeller law. However, the total resistance includes other terms than R_c Eq. 2.26, thus deviations from the propeller law are expected for instance in rough seas [MAN, 2018]. Therefore, a better estimation of power is required.

[ITTC, 2014] made a summary of power prediction methods. The Torque and Revolution Method (QNM) and Thrust and Revolution Method (TRM) which requires a self-propulsion test to measure the increase in propeller torque, thrust and rate of revolutions. The Resistance and Thrust Identity Method (RTIM) is used in this study and requires only the added resistance to predict the power increase.

In [MAN, 2018] and [ISO, 2015], the recommended method is called Direct Power Method (DPM) and is similar to RTIM. The main advantage of the DPM and RTIM methods is that they allow considering the effect of environmental conditions and requires only the added resistance which could be estimated.

The common assumptions for the mentioned methods for computing the main engine power (DPM and RTIM) is that the propeller characteristics and the self-propulsion factors such as the wake fraction factor $(1 - w)$ and the thrust deduction factor $(1 - t)$ in waves is identical to those in still water or calm water.

Direct Power Method DPM

There is a whole energy transmission and propulsion chain from the brake power to the delivered power and the effective power. The work done in moving a ship work is given by the scalar product of force and displacement $R_t V$ (effective power P_E)[Lewis, 1988].

- Open-water efficiency η_O

  In rough seas, waves exert an additional resistance on the hull and affect the functioning of the propeller compared to calm water conditions. The usual measure of propeller performance is determined by the open-water efficiency η_O [Carlton, 2019]. It depends on the advance speed V_a, the thrust force T_h, the torque Q, the rate of revolutions n and other parameters regarding the propeller design:

$$\eta_O = \frac{T_h V_a}{Q 2\pi n} = \frac{K_T}{K_Q}\frac{J}{2\pi} \tag{2.54}$$

In this study, η_O is computed for a specific operational conditions to show the effect of waves on the propeller performance. Starting by computing the ship resistance R_t which is equal to R_c in the case of calm water, an additional resistance R_{aw} in waves and R_{wind} in wind. Then the thrust T_h is estimated from Eq. 2.18, and the propeller load factor $\tau = K_T/J^2$ in operating conditions is given by:

$$\tau = \frac{T_h}{\rho D_p^2 V^2 (1-w)^2} = \frac{R_t}{(1-t)(1-w)^2 \rho V^2 D_p^2} \tag{2.55}$$

To compute the propeller open-water efficiency η_O in waves as in [Kim and Roh, 2020], the advance speed coefficient J is then computed by solving the following equation:

$$\tau - \frac{a_T J^2 + b_T J + c_T}{J^2} = 0 \tag{2.56}$$

The coefficients a_T , b_T, and c_T are interpolated from Eq. 2.23, where $J = V_{SMCR}(1 - w)/(n_{SMCR} D_p)$. V_{SMCR} and n_{SMCR} are the speed and the rate of revolutions at specified maximum continuous rating given by the engine sheet provided by the CEAS tool[4].

Once J is estimated, the dimentionless thrust and torque $K_T(J)$ and $K_Q(J)$ are computed and deployed into Eq. 2.54 to predict the propeller efficiency η_O in specific operating and environmental conditions.

- Relative rotative efficiency η_R

The relative rotative efficiency is the ratio between the absorbed power in open water and in wake behind the hull at the advanced speed V_a. It is normally between 1 and 1.07 for a ship with a single propeller [MAN, 2018]. An approximation given by [Holtrop and Mennen, 1982] for hulls with conventional stern reads:

$$\eta_R = 0.9922 - 0.05908 A_e/A_o + 0.07424(C_P - 0.225 lcb) \tag{2.57}$$

where A_e/A_o is the blade area ratio. For single-screw ships with open stern, $\eta_R = 0.98$. For twin-screw ships, η_R is expressed as:

$$\eta_R = 0.9737 + 0.111(C_P - 0.225 lcb) - 0.06325 P/D \tag{2.58}$$

where P/D is the pitch ratio.

[4] https://www.man-es.com/marine/products/planning-tools-and-downloads/ceas-engine-calculations

- Hull efficiency η_H

  When the propeller advances in water, not all the thrust power P_T delivered by the propeller can be converted into power available for towing (called also effective power) P_E. Therefore, a hull efficiency η_H is introduced, which is defined by:

$$\eta_H = \frac{P_E}{P_T} = \frac{R_t V}{T V_a} = \frac{\frac{R_t}{T}}{\frac{V_a}{V}} = \frac{1-t}{1-w} \tag{2.59}$$

- Propulsive efficiency η_P

  The propeller transforms the brake power P_B delivered by the main engine via the shaft into thrust force T_h to propel the ship. The propulsive efficiency η_P is expressed as the product of hull efficiency η_H, propeller open-water efficiency η_O, and the relative rotative efficiency η_R:

$$\eta_P = \eta_H \eta_R \eta_O \tag{2.60}$$

  The process and the required inputs of the computation of η_P are summarised in the following diagram:

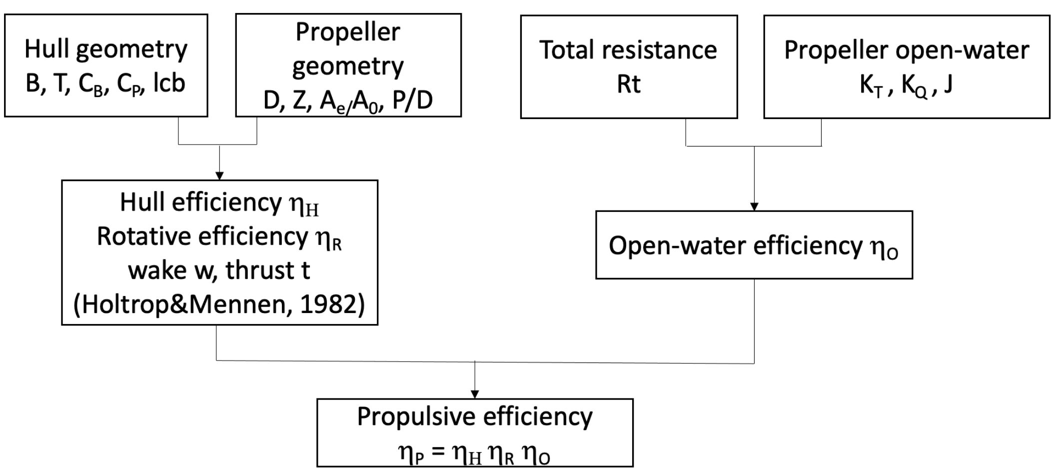

Figure 2.17: Process of the propulsive efficiency η_P estimation

  So, the power delivered to the propeller is determined as:

$$P_D = \frac{P_E}{\eta_P} \tag{2.61}$$

  where the effective power is $P_E = R_t V$.

Resistance and Thrust Identity Method (RTIM)

The same as the DPM method, for the Resistance and Thrust Identity Method (RTIM) in [ITTC, 2011b], the power in rough seas is computed assuming that the thrust deduction fraction t and the wake fraction w are the same in calm water and in waves.

Once the ship resistance R_t is determined, the thrust T is computed as in Eq. 2.18. Then the load factor is given as function of the thrust as:

$$\tau = K_T / J^2 = \frac{T}{\rho D_p^2 V^2 (1-w)^2} \tag{2.62}$$

The advance speed coefficient J is obtained as in Eq. 2.56. Based of the calculated J, torque and power coefficients (K_Q and K_P) are determined as:

$$K_Q = a_Q J^2 + b_Q J + c_Q \tag{2.63}$$

$$K_P = \frac{K_Q}{J^3} \tag{2.64}$$

Knowing that the delivered power is $P_D = 2\pi n_s Q$, and that torque Q is given by:

$$Q = K_Q \rho n^2 D_p^5 = K_P J^3 \rho n^2 D_p^5 \tag{2.65}$$

Upon replacing the advance speed $J = V_a/(nD_p)$ and Q by Eq. 2.65, the delivered power is obtained by:

$$P_D = 2\pi K_P \rho (1-w)^3 V^3 D_p^2 \tag{2.66}$$

2.3.2 Sustained speed and relative speed loss

Forward speed is a relevant factor for large vessels, influencing its operational efficiency. In rough seas, ship speed can be reduced either voluntarily or involuntarily. Voluntary speed loss refers to the speed loss when the ship master decide to lower the speed while perceiving a risk, such as excessive slamming, dangerous rolling motions or broaching. The involuntary speed loss refers to the speed loss as a result of added resistance due to waves and wind, and changes in the propeller efficiency due to waves [Faltinsen, 1990]. Its prediction is particularly essential for ship weather routing.

To take into account the effect of the environmental conditions on ship performance, IMO makes use of a so-called weather factor f_w as the ratio between sustained speed in rough seas V_w and in calm water V_0:

$$f_w = \frac{V_w}{V_0} \tag{2.67}$$

The weather factor f_w is related to the relative speed loss RSL by:

$$RSL = \frac{V_0 - V_w}{V_0} = 1 - f_w \tag{2.68}$$

The ITTC-Procedure [ITTC, 2017b] set an overall process to find f_w from a balance between power delivered to and dissipated at the propeller using the speed-power curve as shown in Fig. 2.18.

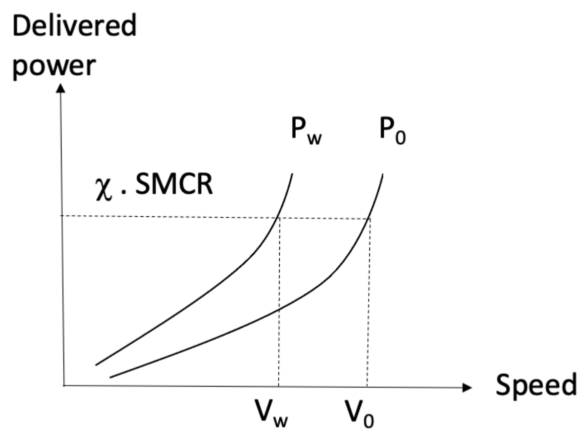

Figure 2.18: Speed-power curve. P_0 and P_w are the curves of delivered power respectively in calm water and in rough seas. V_0 and V_w are the sustained speeds respectively in calm water and in rough seas. $\chi \cdot SMCR$ is the fixed power assumed for sailing. χ is the engine load and $SMCR$ is the specified maximum continuous rating brake power for continuous operation of the engine

Fixed delivered power for sailing

This Speed-power procedure considers that ship is sailing at fixed power P'_D expressed by:

$$P'_D = P_B \cdot \eta_S$$
$$P_B = \chi \cdot SMCR \tag{2.69}$$

where P_B is the brake power developed by the engine at the crank-shaft coupling and transmitted along the shaft to the propeller. χ is the engine load and $SMCR$ is the specified maximum continuous rating brake power for continuous operation of the engine.

η_S is the shaft efficiency determining the loss of power due to the gearing and shaft resistance. It is usually less than 2% and should be stated by the manufacturer. In this study, for simplicity a shaft efficiency $\eta_S = 100\%$ is assumed. Thus, the fixed delivered power is given by:

$$P'_D = \chi \cdot SMCR \tag{2.70}$$

In this work, a real engine is chosen based on to the size and the hull geometry of the ship as explained in Sect. 2.1.4. The CEAS tool[5] is used to compile the engine parameters providing the engine performance data and the specific fuel oil consumption.

In other studies, the minimum power line [Shigunov, 2013] is used and calculated as follows:

$$MCR_{min} = a \cdot DWT + b \tag{2.71}$$

where DWT is the deadweight of the ship in metric tons; and a and b are the parameters given for tankers, bulk carriers and combination carriers in Tab. 2.3.2.

[5]https://www.man-es.com/marine/products/planning-tools-and-downloads/ceas-engine-calculations

Table 2.7: Parameters a and b for determining of the minimum power line values for the different ship types[Shigunov, 2013]

Ship type	a	b
Bulk carrier whose DWT is less than 145,000	0.0763	3374.3
Bulk carrier whose DWT is 145,000 and over	0.0490	7329.0
Tanker and Combination carrier	0.0652	5960.2

Power balance

The required delivered power in this study is computed through Eq. 2.61 if DPM method is used or by Eq. 2.66 if RTIM method is used. It's determined by:

$$P_D = \begin{cases} P_E/\eta_P & \text{for DPM} \\ 2\pi K_P \rho (1-w)^3 V^3 D_p^2 & \text{for RTIM} \end{cases} \tag{2.72}$$

Since the energy is conserved during the transmission chain from the engine to the propeller, the power balance apply:

$$P'_D - P_D = 0 \tag{2.73}$$

Solving this non-linear equation will deliver either the sustained speed V_w in waves or V_0 in calm water.

2.4 CO_2 emissions modelling

CO_2 is the largest contributor to emissions coming from shipping. The main engine used for propulsion, is the principal emitter of CO_2 emissions compared to the auxiliary engine and the boiler, as explained is Sect. 2.1.4.

The CO_2 emission rate is computed as in [Mannarini et al., 2021]:

$$\frac{dCO_2}{dt} = P_B \cdot \mathrm{SFOC} \cdot E_f \tag{2.74}$$

where E_f is the mass-based emission factor per fuel type as shown in this table:

Table 2.8: Different fuel-based emission factors E_f [IMO, 2020b]

Fuel Type	E_f (g/g)
HFO	3.114
MDO	3.206
LNG	2.750
Methanol	1.375
LSHFO 1.0%	3.114

The specific fuel oil consumption (SFOC) and the engine brake power P_B are taken from the corresponding engine sheet from the CEAS tool. The fuel consumption of main engines used in propulsion is the product of SFOC and P_B. The relative SFOC curves are provided by the engine manufacturer(e.g, MAN and Wärtsilä) as a non-linear function of engine load, with a minimum at as specific value approximately from 70 to 80% engine load, the optimal regime in term of fuel consumption and performance.

Some models in literature, such as STEAM2 in [Jalkanen et al., 2012] assumed a parabolic function for all engines, and used a regression analysis of SFOC-measurement data from Wärtsilä to derive a second degree polynomial equation for the relative SFOC. The absolute fuel consumption is estimated from:

$$\begin{aligned} SFOC &= SFOC_r \cdot SFOC_b \\ SFOC_r &= 0.455\chi^2 - 0.71\chi + 1.28 \end{aligned} \tag{2.75}$$

where $SFOC_b$ is the lowest SFOC for a given engine, given by [IMO, 2020a] as function of engine type and age. $SFOC_r$ is the relative SFOC depending on the engine load χ.

The emissions are commonly are estimated using a fuel-based emission factor Tab. 2.4 which relate the quantity of emitted species (e.g.CO_2 , sulfur oxides (SO_x) and BC) to the amount of burned fuel [IMO, 2020b]. Instead, an energy-based emission factor is needed to estimate emissions of other pollutants (e.g nitrogen oxides (NO_x), methane (CH_4), carbon monoxide (CO), nitrous oxide (N2O), particulate matter (PM2.5 and PM10),and non-methane volatile organic compounds (NMVOC)) depending on the engine power output.

Chapter 3

Numerical experiments using the new module *bateau*

Chapter 3 is dedicated to presenting the new module *bateau* developed on the theory of ship resistance and performance explained in Chap. 2. Numerical experiments were performed in regular waves, to investigate the impact of waves and wind on ship speed. This includes a preliminary investigation on the role played by wave steepness.

The concept and overall structure of *bateau* are presented in Sect. 3.1. The database of studied ships and their characteristics in term of hull geometry and propulsion system are shown in Sect. 3.2. The results of *bateau* numerical experiments in idealized conditions regarding ship resistance are detailed in Sect. 3.3, and sustained speed in head and oblique seas in Sect. 3.4. Sect. 3.5 details the outcome of the CO_2 rate estimation.

3.1 Module concept and structure

The VISIR model was extensively tested for its path planning component ([Mannarini and Carelli, 2019a], [Mannarini et al., 2019b]) and was engineered for powering operational systems (VISIR-NAV[1], GUTTA-VISIR[2]). However, it was lacking in a featured ship modeling component. It could either work with a simplified vessel parametrization [Mannarini et al., 2016] or via representation of seakeeping and emissions from a ship simulator [Mannarini et al., 2021].

The new *bateau* module was developed with the aim of filling this gap, and in particular to add a capacity to represent large ocean-going vessels in realistic sea states. This includes accounting for both the wave height and the relative direction of waves. To achieve the former feature, a search for parametrizations of wave-added resistance in oblique sea was needed. *bateau* is built based on the theory of ship hydrodynamics and performance in rough seas and wind presented in Chap. 2. The module includes the main parts of the ship, hull and propulsion system.

[1]https://www.youtube.com/watch?v=cEf_hw9ERbE

[2]https://www.gutta-visir.eu/

The two final objectives of *bateau* are: estimating the sustained speed of a vessel in a seaway and the corresponding CO_2 emission rate.

The first part of *bateau* was developed to predict the added resistance due to waves and wind through a semi-empirical approach. The total resistance together with the propeller open-water characteristics allows estimating the required delivered power in calm water and in rough seas. Assuming that the ship is sailing at constant power, the power balance delivers an estimation of the involuntary speed loss and the subsequent sustained speed.

The second part corresponds to the computation of the CO_2 emission rate using the engine performance data, as a function of the specific fuel consumption and main engine power.

An overview on *bateau* input parameters and output functions are set out in the following diagram. The information on how they interface to the model VISIR is deferred to Chap. 4.

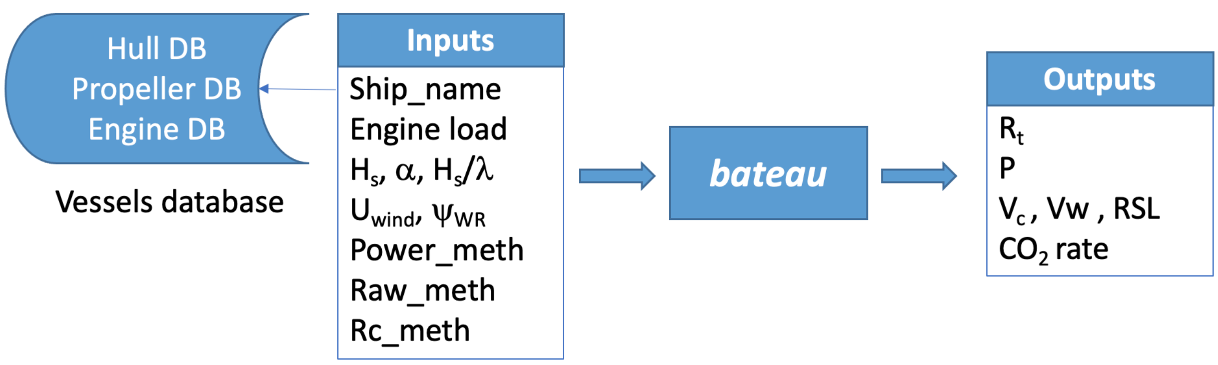

Figure 3.1: *bateau* inputs-outputs

3.2 Vessels database

The *bateau* database includes several large ocean-going ships for which hull, propeller and engine data are available in the literature. So far, a total of thirteen vessels have been considered. They were: S.A. Van Der Stel cargo ship [Alexandersson, 2009], Feeder container ship[3], KCS container ship[4], DTC (Duisburg Test Case) container ship [Moctar et al., 2012], S175 container ship [Fujii and Takahashi, 1975], 66k DWT bulk [Yu et al., 2017], Bulk carrier[Yamamoto, 1986], the tanker KVLCC2[5], S-VLCC tanker[Park et al., 2019], HSVA cruise ship [Valanto and Hong, 2015], and two models of Series 60 [Strom-Tejsen et al., 1973]. Another ship, the c2591 bulk carrier, was provided by the Institute of Marine Engineering (CNR-INM) in Rome.

The main geometry parameters of the studied ships are listed in Tab. 3.1.

[3] https://products.damen.com/en/ranges/container-feeder/container-feeder-800

[4] http://www.simman2008.dk/kcs/container.html

[5] http://www.simman2008.dk/kvlcc/kvlcc2/kvlcc2_geometry.html

Table 3.1: Main particulars of the studied ships

	Ship	$L_{pp}[m]$	$B[m]$	$T[m]$	$C_B[-]$	$L_E[m]$	$k_{yy}[-]$
S01	S.A. Van Der Stel cargo ship	153	22.8	9.1	0.563	61.0	0.22
S02	DTC container ship	355	51.0	14.5	0.661	112.0	0.27
S03	KCS container ship	230	32.2	10.8	0.6505	-	0.25
S04	S175 container ship	175	25.4	9.5	0.572	59.1	0.24
S05	Feeder container ship	120	21.0	7.3	0.6757	30.0	0.25
S06	Bulk carrier	285	50.0	18.5	0.829	51.0	0.25
S07	66k DWT bulk	192	36.0	11.2	0.822	-	0.25
S08	c2591 bulk carrier	196	32.3	12.9	0.8254	49.0	0.25
S09	S-VLCC tanker	323	60.0	21.0	0.811	60.0	0.25
S10	KVLCC2 tanker	320	58.0	20.8	0.8098	60.0	0.25
S11	HSVA cruise	220	32.2	7.2	0.654	72.4	0.26
S12	S60 model 4210	122	16.3	6.5	0.6	52.0	0.25
S13	S60 model 4211	122	16.8	6.7	0.65	46.5	0.25

Four ships were studied to compute the sustained speed in rough seas V_w and the relative speed loss. Their propeller parameters and the selected engine data are given in Tab. 3.2:

Table 3.2: Propeller and engine data of ships for which sustained speed is computed in this thesis

	Propeller				Engine		
	D_p	Z	A_e/A_o	P/D	name	MCR	V_{SMCR}
units	m	-	$-$	-	-	kW	kn
S02	8.9	4	0.800	0.959	10G95ME-C10.5	68,700	23.0
S05	5.1	4	0.520	0.765	5S35ME-C9.7	4,350	16.0
S08	6.5	4	0.425	0.716	8G50ME-C9.6	13,760	14.5
S10	9.9	4	0.431	0.721	7G80ME-C10.5	32,970	15.0

3.3 Ship resistance in idealised metocean conditions

This section presents the outcome of *bateau* numerical experiments. To simplify the experiments, an idealised environmental conditions was set. For VISIR-*bateau* simulation instead, a realistic conditions from data assimilative model outputs (CMEMS) are used.

In Sect. 3.3.1, the calm water resistance estimations for various ships are shown. In Sect. 3.3.2, the numerical results of wave-added resistance R_{aw} at a fixed wave steepness H_s/λ are compared to available experimental data in the literature, in both head and oblique seas. This section also includes a sensitivity study to investigate the effect of increasing forward speed,

and variation of steepness on the wave-added resistance R_{aw}.
The prediction of the added resistance due to wind is presented in Sect. 3.3.3 highlighting the combined effect of ship speed, wind speed and direction, and ship superstructure.

3.3.1 Calm water resistance

The parametrization of the calm water resistance R_c is based on the theory explained in Sect. 2.2.1. For all numerical tests, standard water conditions, i.e. temperature $T_r = 15°C$ and kinematic viscosity $\mu = 1.1386 \cdot 10^6\ m^2/s$ were assumed.
First experiments were done for four container ships, two bulkers and a tanker, using both [Holtrop and Mennen, 1982] and [Kristensen and Bingham, 2017] formulas for R_c computation. Fig. 3.2 shows that blunt hulls have higher R_c than the slender ones. For the same ship type, e.g. containerships, R_c decreases from larger hull to small ones (in term of length L_{pp}, beam B, draught T as shown in Tab. 3.1). This is because R_c is proportional to the speed and the wetted surface which depend on the main dimensions of the hull Eq. 2.31.
Some fluctuations are noted for both bulkers, namely the curves made by wave making resistance due to waves interference: this is due to the interaction of both bow and stern wave systems moving with the ship with the same lengths[6]. This is seen particularly for bulkers as they usually sail at lower speed compared to tankers and containerships.
On testing both resistance estimation methods mentioned, it appears that the [Holtrop and Mennen, 1982] gives a relatively higher estimation of the calm water resistance than the [Kristensen and Bingham, 2017] formula.

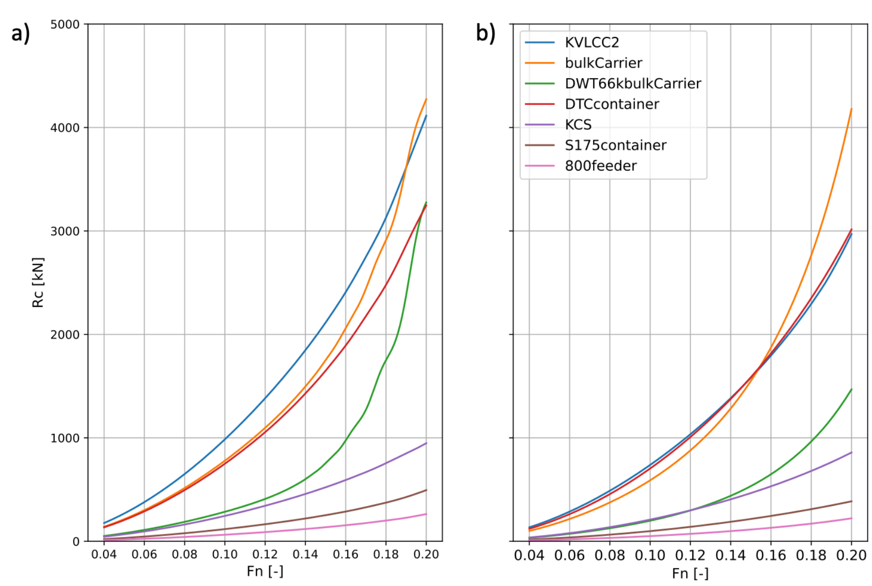

Figure 3.2: Calm water resistance for several vessels, according to [Holtrop and Mennen, 1982] (panel a) and [Kristensen and Bingham, 2017] (panel b)

Fig. 3.2 shows that the KVLCC2 tanker has the highest R_c compared to the other ships. It was used in further tests to investigate the contribution of the main R_c components. [Holtrop and Mennen, 1982] formula was used to compute the calm water resistance R_c for

[6] https://www.mermaid-consultants.com/ship-wave-making-resistance.html

the KVLCC2 tanker. Fig. 3.3 shows that the viscous resistance $R_v = R_f(1+k_1)$ is the dominant component in the calm water resistance R_c. R_v contributes about 80% of R_c for lower speed than the designed one ($Fn < 0.142$). Then, it drops against a rise of the wave making and breaking resistance R_w.

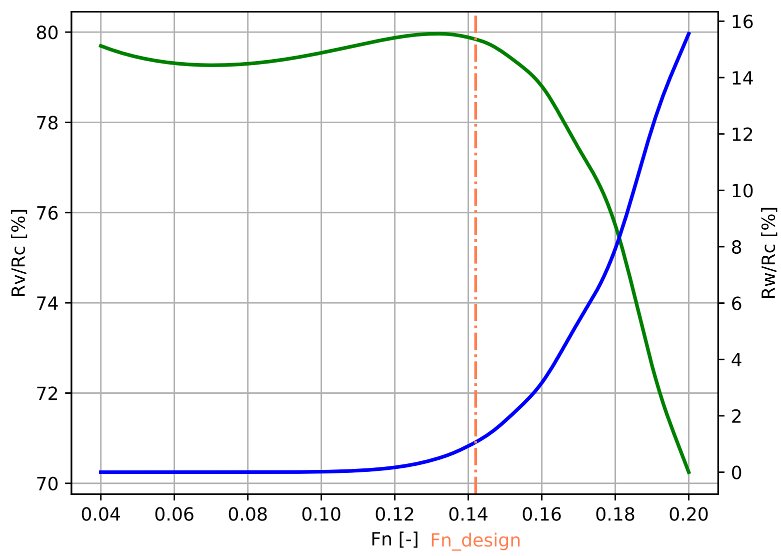

Figure 3.3: Contribution of viscous resistance R_v and wave making and breaking resistance R_w to the calm water resistance R_c as in the [Holtrop and Mennen, 1982] formula for the tanker KVLCC2. The former resistance component is the green line and the latter is the blue one. The vertical line refers to the design speed.

3.3.2 Wave-added resistance

On oceans, the natural seaway is irregular and multidirectional [Molland, 2008]. It is composed of a mixture of waves of different height, length, and direction. An irregular wave pattern is the sum of regular partial sinusoidal waves having a relatively small steepness, also for a severe sea [Molland, 2008]. Thus, a representation for a random sea could be done through the spectral approach of the sum of regular waves.

Unfortunately, the Copernicus Marine System does not provide the wave spectra in the global domain. The latter is still not be ingested by VISIR. Moreover, *bateau* already includes a wealth of ship parameters (e.g.hull geometry and propulsion system), and computational models (e.g.for resistance, power and sustained speed) to make regular waves not so straightforward.

Therefore, in this study the numerical experiments of wave-added resistance were performed in regular waves at fixed steepness. Assuming the deep-water approximation of the wave dispersion relation, the wavelength λ is expressed as:

$$\lambda[m] = \frac{g_0}{2\pi} T_W^2 \approx 1.56 T_W[s]^2 \tag{3.1}$$

where T_W is the wave spectrum peak period [Mannarini et al., 2016].

Then, assuming a fully developed sea (Pierson–Moskowitz spectrum), the wave steepness can be estimated as:

$$H_s/\lambda = \frac{2\pi}{g_0} \frac{H_s}{T_W^2} = \frac{8\pi}{24.17^2} \approx 1/23 \tag{3.2}$$

Unfortunately, the wave steepness in almost papers dealing with ship resistance is not mentioned and nor is its effect considered.

Numerical results vs experimental measurements

Numerical simulations are performed to estimate the wave-added resistance using various semi-empirical formula in both head and oblique seas, with $H_s/\lambda = 1/23$, and compared to observations as shown in Fig. 3.4 and Fig. 3.5.

To make different vessels more comparable to each other, all panels refer to the normalized wave-added resistance defined as:

$$C_{aw} = \frac{R_{aw}}{\rho g \zeta_a^2 B^2 / L_{pp}} \tag{3.3}$$

where ζ_a is the wave amplitude, B is the beam, L_{pp} is ship length between perpendiculars.

Seakeeping experimental tests are useful to understand the vessels behaviour in the actual sea state and to validate numerical and empirical tools. A database of available towing tank measurements found in the literature, is presented in Tab. 3.3.

Table 3.3: Available observational data of wave-added resistance

	Hull	Fn	α [deg]	Reference
S01	Van Der Stel	0.15	0	[Alexandersson, 2009]
S02	DTC	0.052	0, 30,60	[Sprenger et al., 2017]
			120, 150, 180	
		0.139	0	[Sprenger et al., 2017]
S03	KCS	0.26	0	[Simonsen et al., 2013]
S04	S175	0.15	0, 30,60, 90	[Fujii and Takahashi, 1975]
			120, 150, 180	
		0.2	0	[Nakamura, 1975]
S06	Bulk carrier	0.13	0	[Yamamoto, 1986]
S07	DWT66kbulkCarrier	0.17	0	[Yu et al., 2017]
S08	S-VLCCtanker	0.137	0	[Park et al., 2019]
S09	KVLCC2	0.142	0	[Hwang, 2013]
				[Sadat-Hosseini et al., 2013]
S10	HSVA	0.233	0, 30,60, 90	[Valanto and Hong, 2015]
			120, 150, 180	
S11	S60 model 4210	0.266, 0.283	0	[Strom-Tejsen et al., 1973]
S12	S60 model 4211	0.237, 0.254	0	[Strom-Tejsen et al., 1973]

Head seas

Numerical tests were performed using STA2, NTUA and CTH in head seas, mentioned previously in Sect. 2.2.2, as well as the NMRI method and [Faltinsen, 1980] to show the asymptotic limit in short head waves.

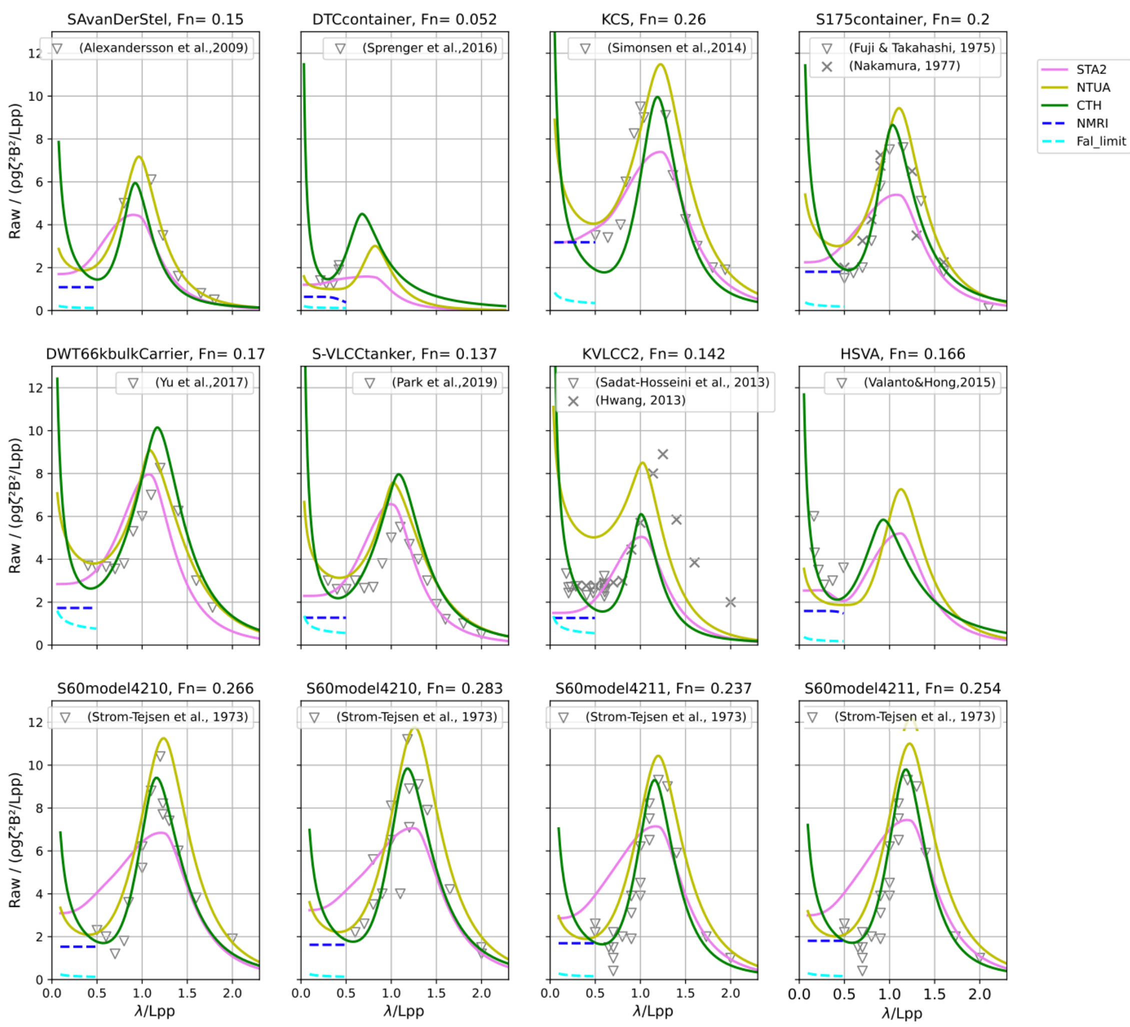

Figure 3.4: Normalized added resistance in head seas vs benchmarking for various hulls. References for observational data are given in legend of each panel, and line colours refer to the various methods, as in legend of upper-right panel. NMRI refers to [Tsujimoto et al., 2008] formula. Fal_limit refers to [Faltinsen, 1980] formula.

In very short waves $\lambda/L_{pp} < 0.3$, the normalized added resistance $C_{aw}$is nearly a constant, in the case of the asymptotic formula of [Faltinsen, 1980] (Fal_limit) and STA2. However, It can reach a large magnitude and variance when using NTUA and CTH formulae. This feature could be due to either wave breaking effects at the bow or to relatively high wave steepness. Experimental data are very scarce in this region because of the difficulty of both generating waves of small amplitude and measuring small forces. This is especially challenging if the vessel model size is also small.

[Park et al., 2015] studied the sources of uncertainty of experimental added resistance and summarised them into: basic instruments, mass distribution, calibration, measurement and data reduction equation uncertainty.

Moreover, the incident wave amplitude ζ_a could not be kept spatially nor temporally constant during the runs or even one run of experiments, which also means that wave steepness H_s/λ varies accordingly. This spatio-temporal uncertainty of ζ_a, besides the proportionality of the added resistance to the squared wave amplitude, leads to large scatter and uncertainty of R_{aw} [Mittendorf et al., 2022].

The wave-added resistance C_{aw} reaches its peak when the wave length λ is around or equal to the ship length L_{pp}. [Faltinsen, 1990] confirmed this resonance position at moderate speed. For larger wavelengths than the ship's length, the C_{aw} decreases approaching to zero for wavelengths twice the ship's length. In this range of wavelengths radiation is dominant, and nonlinear effects are moderate. Instead, in short waves nonlinear effects are significant, and diffraction is dominant.

Fig. 3.4 shows that wave-added resistance due to diffraction in head seas is generally underestimated by the [Faltinsen, 1980] (Fal_limit) and [Tsujimoto et al., 2008] formulae (NMRI). The STA2 method seems problematic in the region $0.5 \leq \lambda/L_{pp} \leq 1$ where there is transition from diffraction dominance to radiation dominance.

Quantitatively, we can conclude that the capacity of each semi-empirical formula in reproducing observations is rather variable. It depends on specific hull geometry, ship speed, and sea state.

Oblique seas

Numerical experiments of R_{aw} were also performed in oblique seas using CTH formula Eq. 2.46. The latter is the unique formula mentioned in Sect. 2.2.2 providing the total R_{aw} as function of the wave angle of attack. Towing tank experiments for arbitrary heading is rarely performed since not all basins have the suitable dimensions and equipments to generate non-bow waves.

From Fig. 3.5 it can be seen that in oblique seas the resistance curves continue being characterised by a resonance peak. However, the peak drifts to a lower reduced wavelength as the angle of attack of waves increases. For quartering or following seas, the resistance even flips its sign and thus becomes an effective thrust.

This is also confirmed by several studies ([Duan and Li, 2013], [Lang and Mao, 2021]). For example, DTC (typical modern containership hull) has been tested in deep water at MARINTEK (scaling factor $1:63$) for experimental measurements of added resistance at head seas with a speed of $6kn$ and $16kn$, and oblique seas with a speed of $6kn$. It was found that the highest forces have been measured in head seas and bow quartering seas (waves $60°$ off the bow). In shorter waves $\lambda/L_{pp} < 0.3$, the added resistance does not change much for headings from $0°$ to $60°$. At $120°$, the observed added resistance is small, changing sign at $\lambda/L_{pp} = 0.25$. From $150°$ to $180°$ (stern quartering to following seas), the added resistance becomes negative, i.e. the vessel undergoes a pushing effect rather than a resistance caused by the presence of the waves[Sprenger et al., 2016] (Fig. 3.5 panel c).

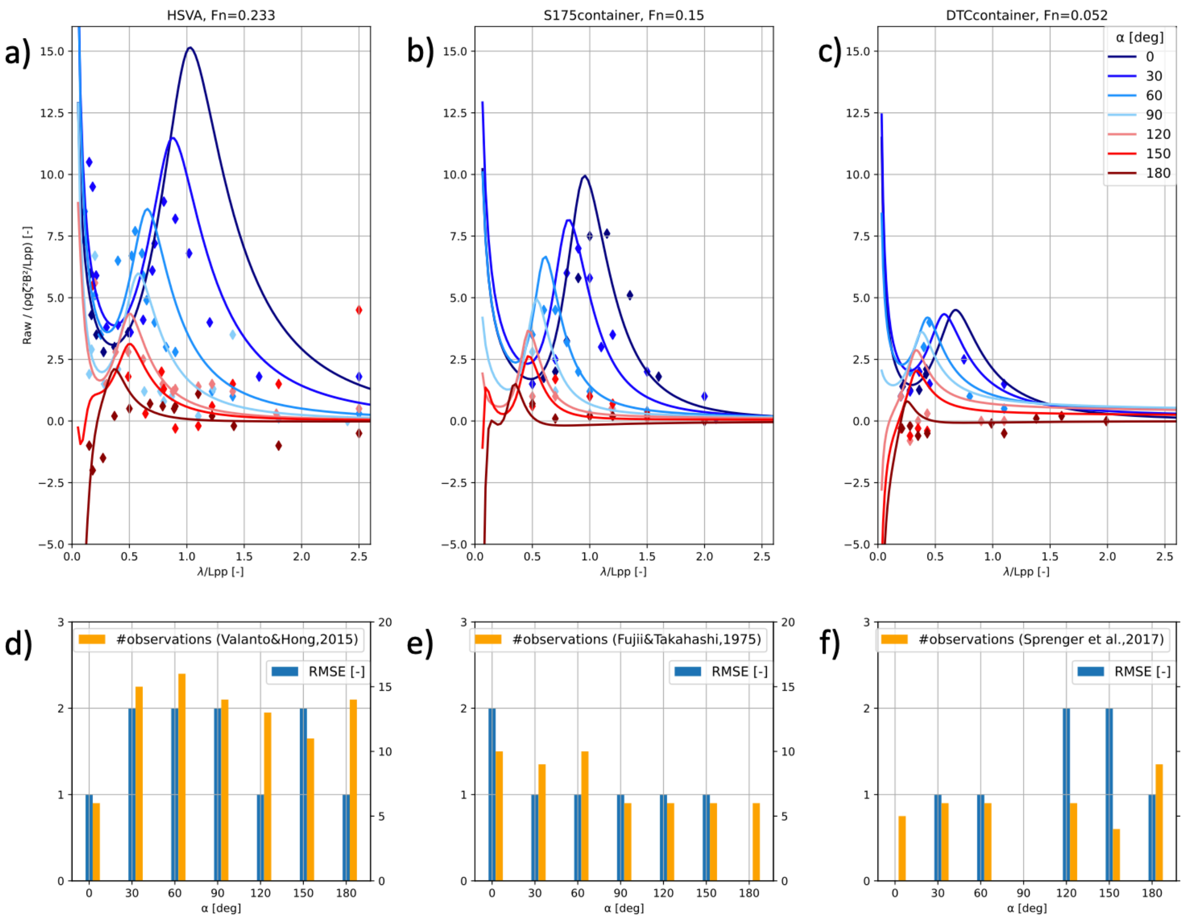

Figure 3.5: Normalised wave-added resistance from CTH formula vs observations for: a) HSVA at Fn=0.233, b) S175 containership at Fn=0.15, c) DTC containership at Fn=0.052. a-c) panels: colours refer to wave angle of attack, markers are observations. d-f) panels: number of observations available at various angles of attack (right y axis) and RMSE of model vs. observations (left y axis)

Dimensionless form of wave-added resistance $C_{aw}(\lambda/L_{pp})$ helps in comparing numerical results to experimental ones, but it neglects some unknown wave charateristics such as wave steepness H_s/λ. The magnitude of dimensional R_{aw} depends on H_s/λ, and this affects the estimation of the sustained speed. In the next section, an investigation on this sensitivity is shown.

Sensitivity of wave-added resistance on wave steepness

Based on [Lee et al., 2019], five values of wave steepness (1/10, 1/20, 1/40, 1/80, and 1/160) were used to compute the peak of wave-added resistance and the wave height resonance. The tests were done for the 800feeder containership at $Fn = 0.2$.

Fig. 3.6 shows an increase of the peak and shift of the resonance towards longer H_s as the steepness increases. This means that the choice of wave steepness has a crucial impact in predicting the sustained speed later.

A linear relationship is noted between the resonance and the steepness. Generally, all the tested formulae have a similar behavior towards the change of wave steepness.

The effect of wave steepness on ship resistance has rarely been addressed in the literature despite its importance. Recently, [Mittendorf et al., 2022] pointed out the lack of publicly available information on wave steepness. The paper mentioned that a correction approach based on steepness could improve the performance of the semi-empirical formula, particularly in short waves and for slender hulls. [Lee et al., 2019] found that as the wave steepness increases, the quadratic dependency of added resistance due to waves becomes weaker. [Sigmund and el Moctar, 2018] observed a dependence of wave-added resistance on wave steepness especially in short waves ($\lambda/L_{PP} < 0.5$) and for blunt hulls. The paper found that the slope of the wave-added resistance coefficient as wave frequency increases gets larger with higher wave steepness.

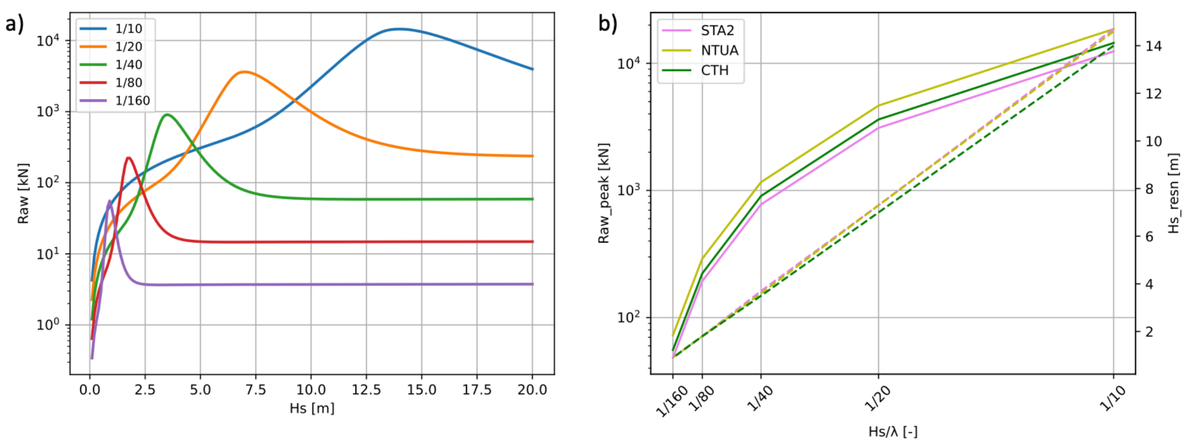

Figure 3.6: a) Wave-added resistance for various values of wave steepness for the feeder at $Fn = 0.2$ using CTH formula. b) Peak and resonance of wave-added resistance. Colours refer to various methods as shown in the legend. The continuous line corresponds to the peak and the dashed one to the resonance.

Sensitivity of wave-added resistance on speed

Container ships are most concerned with speed management as they sail with higher speed than tankers and bulkers. Therefore, a container ship was chosen as a test case, namely the DTC, which is a typical hull design of a modern 14,000 TEU post-panamax container carrier, developed at the Institute of Ship Technology, Ocean Engineering and Transport Systems in Duisburg [Moctar et al., 2012]. In Fig. 3.7, the wave-added resistance for various service speeds is shown. The variation of the added resistance as function of the speed using STA2, for the DTC container ship, shows a drift of the resonance towards higher λ/Lpp as the speed increases, accompanied with a rise in its amplitude. A large increase of resistance with increasing speed values is found especially in long waves and this is due to ship motions.

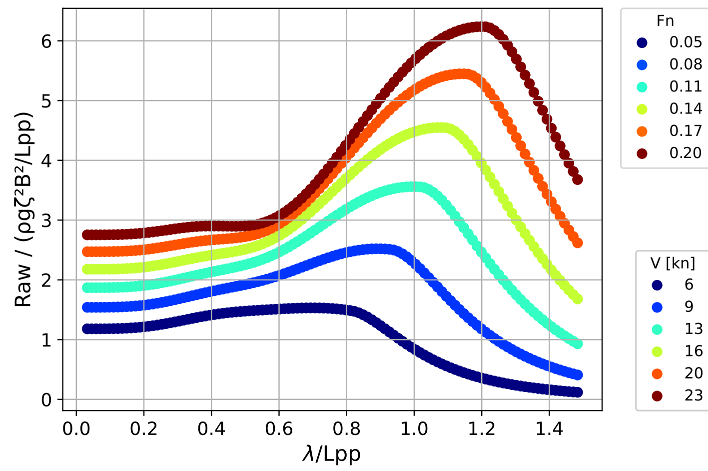

Figure 3.7: Variation of the normalized wave-added resistance as a function of speed for the DTC containership using STA2

Further numerical experiments with *bateau* were carried out to investigate the effect of speed on resistance for various ship types. In Fig. 3.8, the resonance amplitude and location is compared for various ships, at different Froude Number. The results confirm that higher peak and resonance are associated with high speeds. It is also noted that the blunt ships (bulkCarrier, 66k DWT bulk carrier, KVLCC2) have the highest peak resistance compared to slender ships (KCS, S175, DTC). This is consistent with what was found in the literature ([Hirota et al., 2005], [Kuroda et al., 2012]).

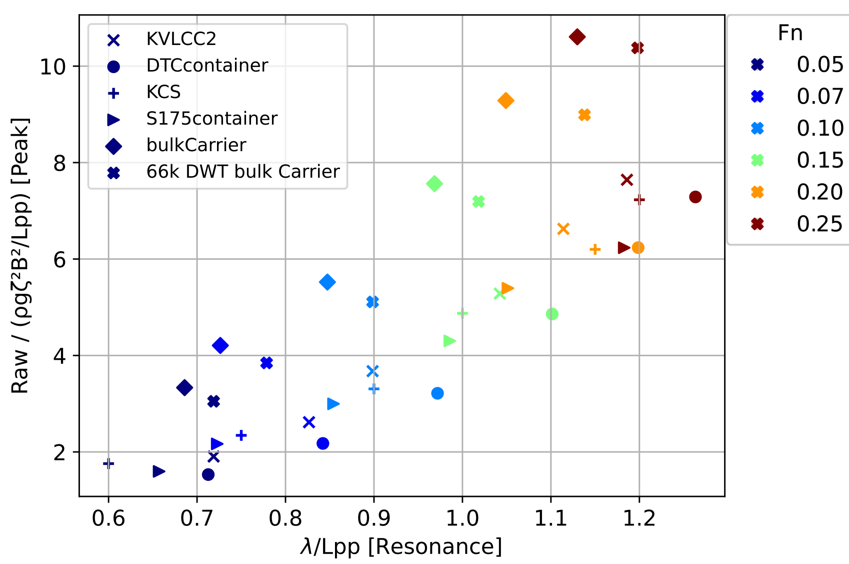

Figure 3.8: Variation of the peak and resonance of the wave-added resistance for different ships and speed.

3.3.3 Wind-added resistance

The wind-added resistance R_{wind} is estimated using [ITTC, 2017e] formula, and [Fujiwara et al., 2005] regression formula for the drag coefficient as explained in Sect. 2.2.3. In the numerical experiments, the mean wind speed V_{wind} is calculated as a function of significant wave height according to the one-parameter Pierson-Moskowitz spectrum [Stewart, 2008], and expressed as:

$$V_{wind} = \sqrt{g_0 H_s / 0.22} \tag{3.4}$$

In this study, it is assumed that wave and wind have the same direction, so that $\psi_{WR} = \alpha$. A wave height of $H_s = 5m$ was selected to test the variation of the wind-added resistance R_{wind} for various ships as a function of the apparent wind angle α when the ships sail at dimensionless speed $0.05 \leq Fn \leq 0.2$.

The results in Fig. 3.9 show that a lateral wind around 90° has no significant effect. An additional resistance is noted at head or bow ($\alpha \leq 45°$) wind especially for the tankers (KVLCC2 and S-VLCC), container ships (DTC) and bulk carriers with a large front area. The quartering or following ($120° \leq \alpha \leq 180°$) wind has a net thrust effect on the ship.

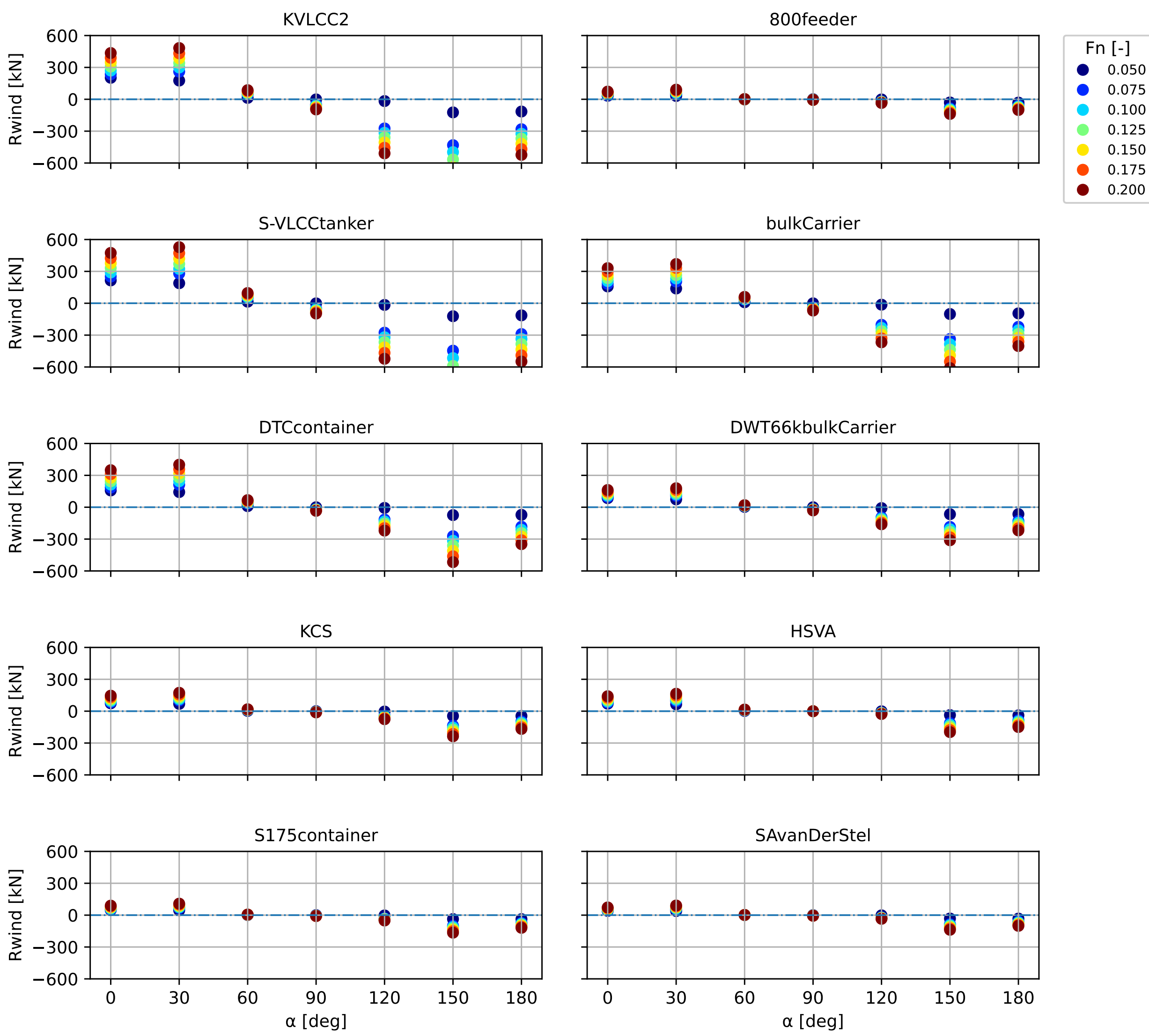

Figure 3.9: Wind-added resistance at $Hs = 5m$ for various ships

As the wind-added resistance was of greater magnitude for the DTC containership, it was selected to evaluate the dependence on Froude Number also at $H_s = 4m$ and $7m$ at various wind apparent angle and ship speed. Fig. 3.10 shows first a linear dependence on the ship's Froude number Fn. The absolute value of the slope increases with wind intensity, and for quartering and following winds, the resistance turns to a net thrust.

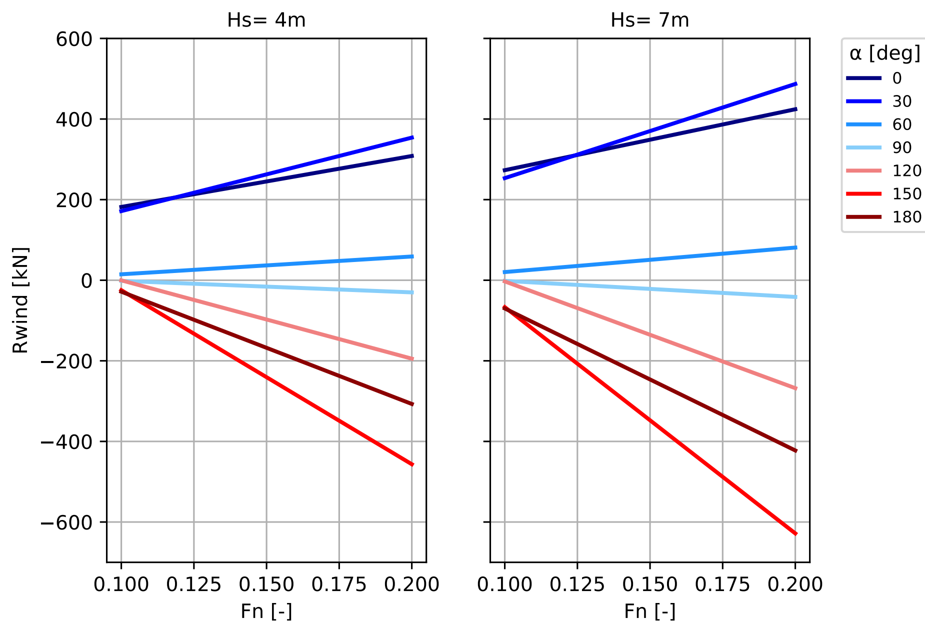

Figure 3.10: Wind-added resistance for the DTC container ship at various speeds and Hs

Wind-added resistance R_{wind} vs R_{aw} and R_c

Fig. 3.12 shows a slight impact of wind on the ship, with a magnitude of resistance similar to the calm water at high sea states.

In the case of this feeder, the calm water resistance is relevant in short waves where $\lambda/L_{pp} < 0.5$. However, wave-added resistance becomes of higher magnitude than calm water resistance especially in long waves ($\lambda/L_{pp} > 0.5$) induced by ship motions. Therefore, the greatest speed loss and the lowest sustained speed are expected to coincide with this relevant added resistance due to waves.

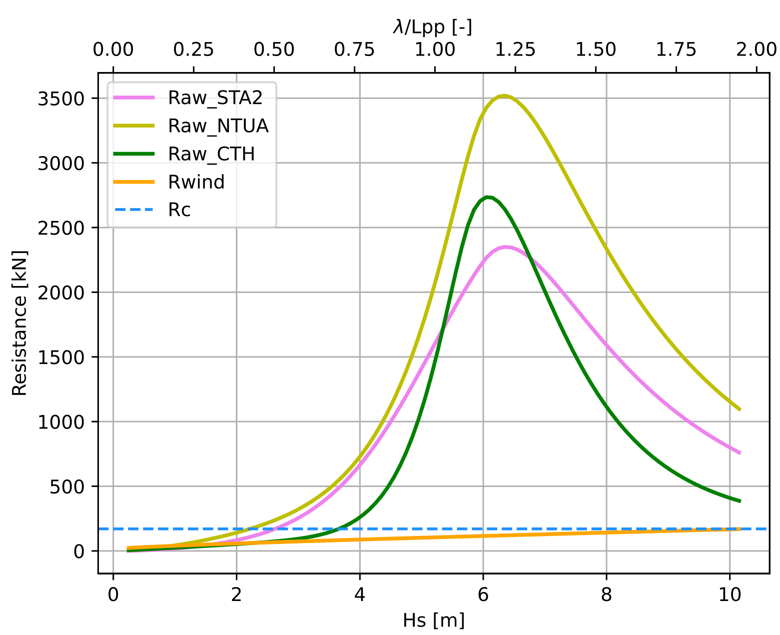

Figure 3.11: Calm water, wave- and wind-added resistance in head seas for the 800feeder at $Fn = 0.2$

3.4 Sustained speed in rough seas

This section presents the outcome of the implementation of Sect. 2.3.2 to compute the relative speed loss and the subsequent sustained speed in rough seas. The latter is computed through a speed-power procedure. We assume that the vessel is sailing at fixed engine load, which is given by the engine performance data as explained in Sect. 2.1.4. Then, for a given sea state, *bateau* estimates the sustained speed in a such an environmental and operational condition. The calm water resistance was computed through [Holtrop and Mennen, 1982] formula as in Sect. 2.2.1. In head seas, three formulae of wave-added resistance were tested (STA2, NTUA and CTH), mentioned in Sect. 2.2.2. In oblique seas, the CTH formula for R_{aw} is used. For power computation, both methods DPM and RTIM (Sect. 2.3.1) are tested. The sustained speed is obtained by solving the power balance non-linear equation as given by Eq. 2.73. The numerical solution involves either bracketing it or proving a first guess of its location. The latter depends on wave height and direction in a vessel-specific way. Thus, a machine learning model based on DecisionTreeRegressor[7] from the sklearn python library was used.

3.4.1 Head seas

Fig. 3.12 shows the curve of the required delivered power in calm water and four sea states in head seas $\alpha = 0°$ for an 800feeder container ship.

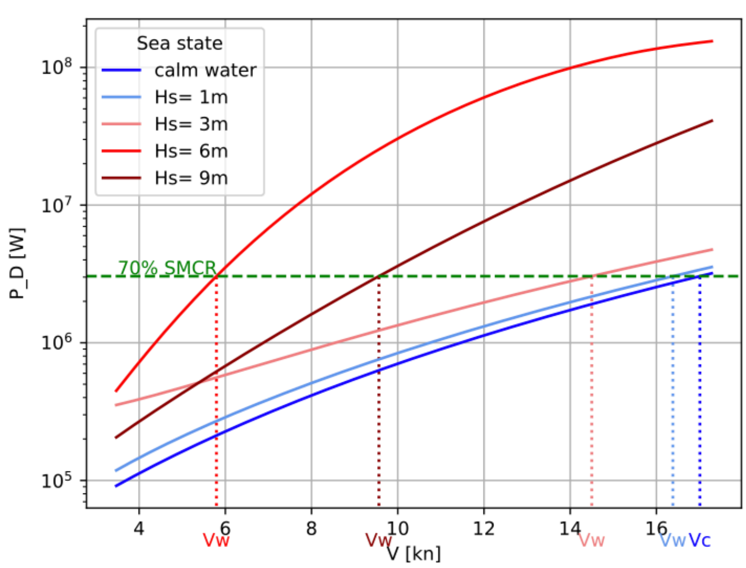

Figure 3.12: Roots computation for the 800feeder at 70% engine load in head seas. CTH method is used for R_{aw} and DPM for power computation

It is clear from Fig. 3.12 that when the vessel sails at increasing wave height, it requires additional power to reach same speed, and it looses its speed when sailing at fixed delivered

[7] https://scikit-learn.org/stable/modules/generated/sklearn.tree.DecisionTreeRegressor.html

power by the engine. The latter balanced with the required delivered power in a specific wave height gives the sustained speed.

Three methods of wave-added resistance in head seas were tested in the case of the feeder ship, to compute the sustained speed in rough seas at 70% engine load. Fig. 3.13 shows a consistent profile of sustained speed versus H_s across the various computational methods for wave-added resistance. The maximum drop of V_w (about $70\%V_c$) is reached at about $H_s = 4.5m$ which coincides with the resonance of wave-added resistance.

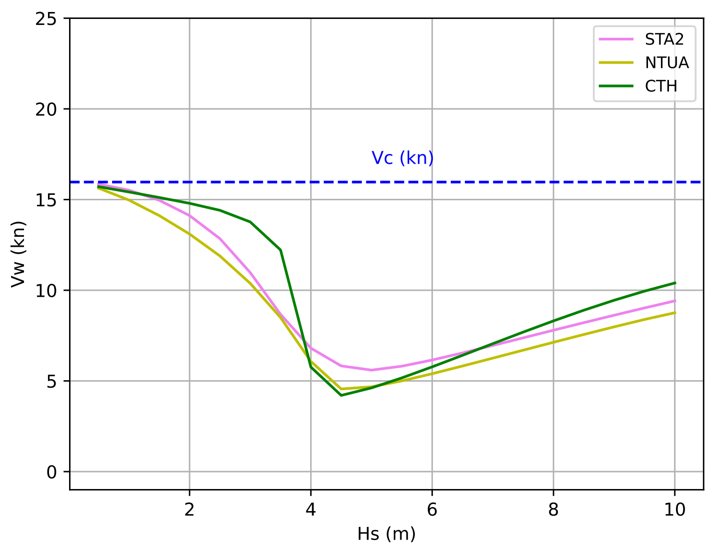

Figure 3.13: Sustained speed in head seas for the 800feeder

Further numerical experiments were performed to examine the variation of the sustained speed V_w as a function of wave height H_s. The NTUA formula for wave-added resistance and DPM in power computation were used.

The results in Fig. 3.14 shows that V_w decreases up to a specific significant wave height value (about $H_s = 5m$) beyond which it rises again. The same for the rate of revolutions of the propeller n (Eq. 2.19) and the propulsive efficiency η_p (Eq. 2.60). The reason is the wave-added resistance which increases up to its peak then falls again.

The results also show, for a given sea state, a more limited role of the engine load on sustained speed.

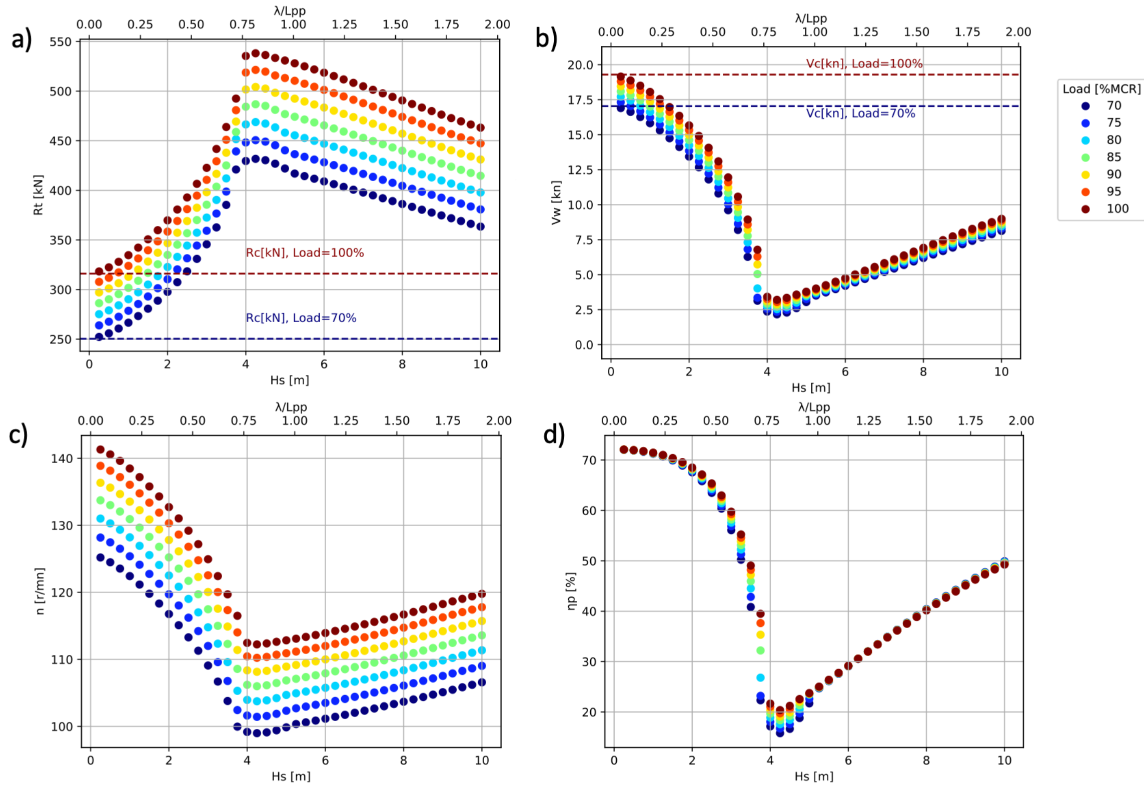

Figure 3.14: a) ship resistance R_t given as coloured markers and R_c as dashed line for two different engine loads, b) sustained speed V_w given as coloured markers and V_c as dashed line for two different engine loads, c)rate of revolutions n, and d) propulsive efficiency η_p at various engine loads for the 800feeder

Numerical experiments were done for four ships (800feeder, DTC containership, KVLCC2, c2591 Bulk Carrier) for which propeller open-water characteristics (POW) are available. One wave angle of attack is considered $\alpha = 0°$. The DPM is used in power computation and STA2 to estimate the wave-added resistance R_{aw}.

The results in Fig. 3.15 show a variation of V_w's trend depending on hull geometry for the same range of wave height and direction. This is due to the dependence of R_{aw} on λ/L_{pp} which varies according to the length of each ship.

Thus, waves affect the vessel performance under the form of speed loss with various magnitude depending on hull dimensions.

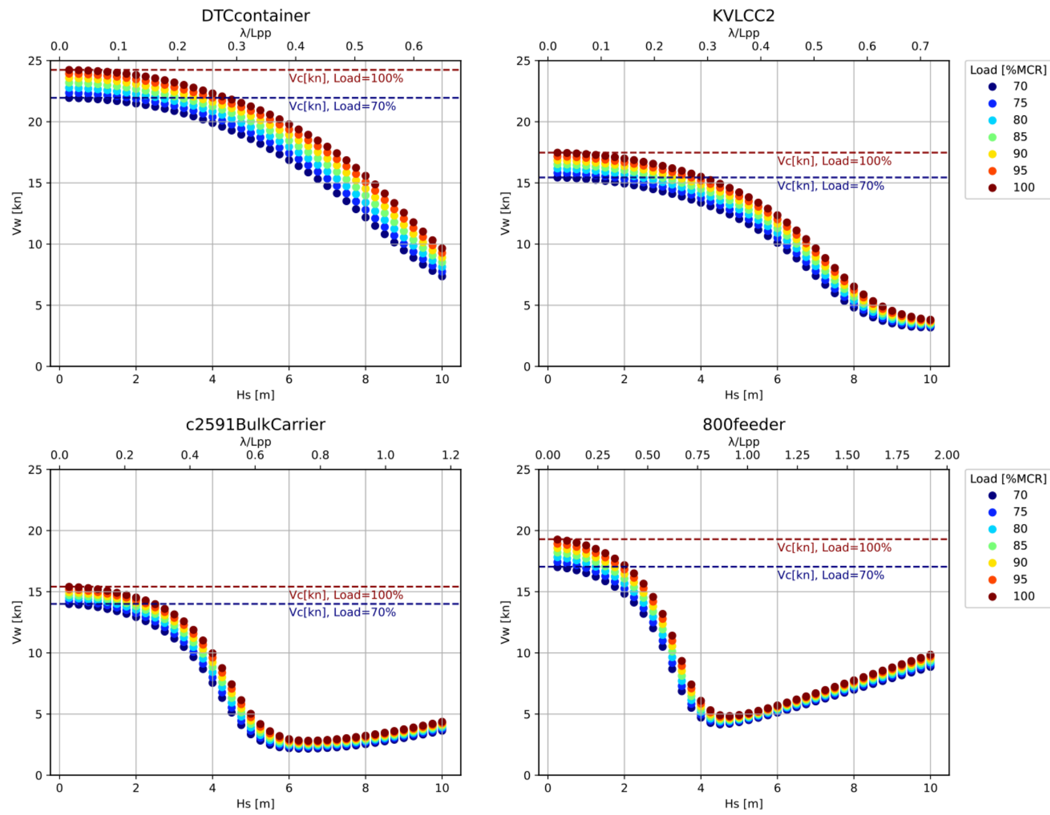

Figure 3.15: Sustained speed at various engine loads for four ships using the DPM in power computation and STA2 to estimate the wave-added resistance Raw

3.4.2 Oblique seas

The previous section presented the results of sustained speed when one angle of attack was considered ($\alpha = 0°$). Instead, this section shows the numerical tests using *bateau* for different angles of attack (oblique seas). The CTH formula (Eq. 2.46) is the unique formula delivering wave-added resistance in oblique seas, hence it is used in these experiments. However, the speed correction factor a_2 causes a discontinuity at $Fn = 0.12$. To address this, it is patched as $a_2 = 0.0072 + 0.24Fn$ also for $Fn \leq 0.12$.

For delivered power estimation, both DPM and RTIM in Sect. 2.3.1 are tested.

Sustained speed

Initial numerical tests were done to investigate the role of DPM and RTIM on sustained speed. Results in Fig. 3.16 show a slight impact of the power prediction method on sustained speed. This is could be due to the fact that the DPM takes into account the propulsive efficiency. Instead, the approach of RTIM is based on the dimensionless power estimation.

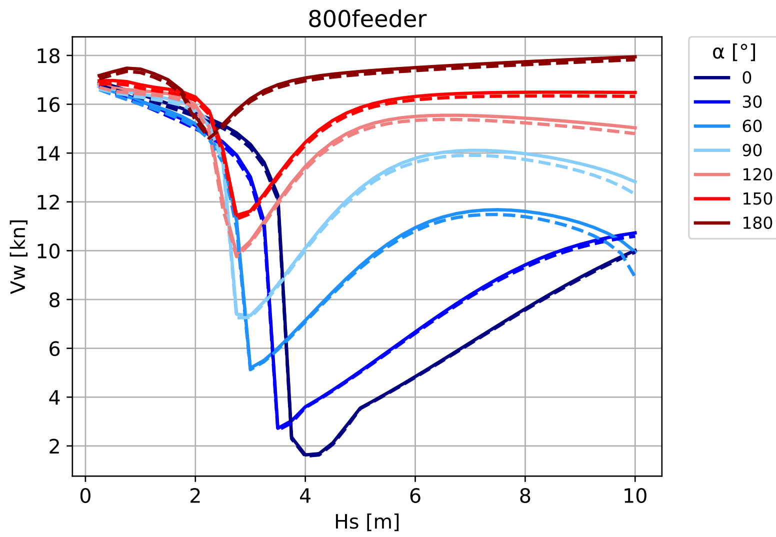

Figure 3.16: Sustained speed for 800feeder. Continuous line refers to DPM method and dashed one for RTIM.

Further numerical experiments were performed for other ships as shown in Fig. 3.17. The results show that for all vessels and angles of attack α, the sustained speed initially decreases with H_s. Above an angle-dependent $H_s(p)$, the speed generally increases. Depending on vessel type, $H_s(p)$ either decreases or increases with alpha.

As noted previously, the trend of V_w varies significantly for each ship. Additionally, the wave height and direction cause a tremendous drop of ship performance.

Results show that both ships in panels c) and d) lose their speeds at high wave heights $(6-10m)$ at $\alpha < 60°$, where ships face the highest resistance.

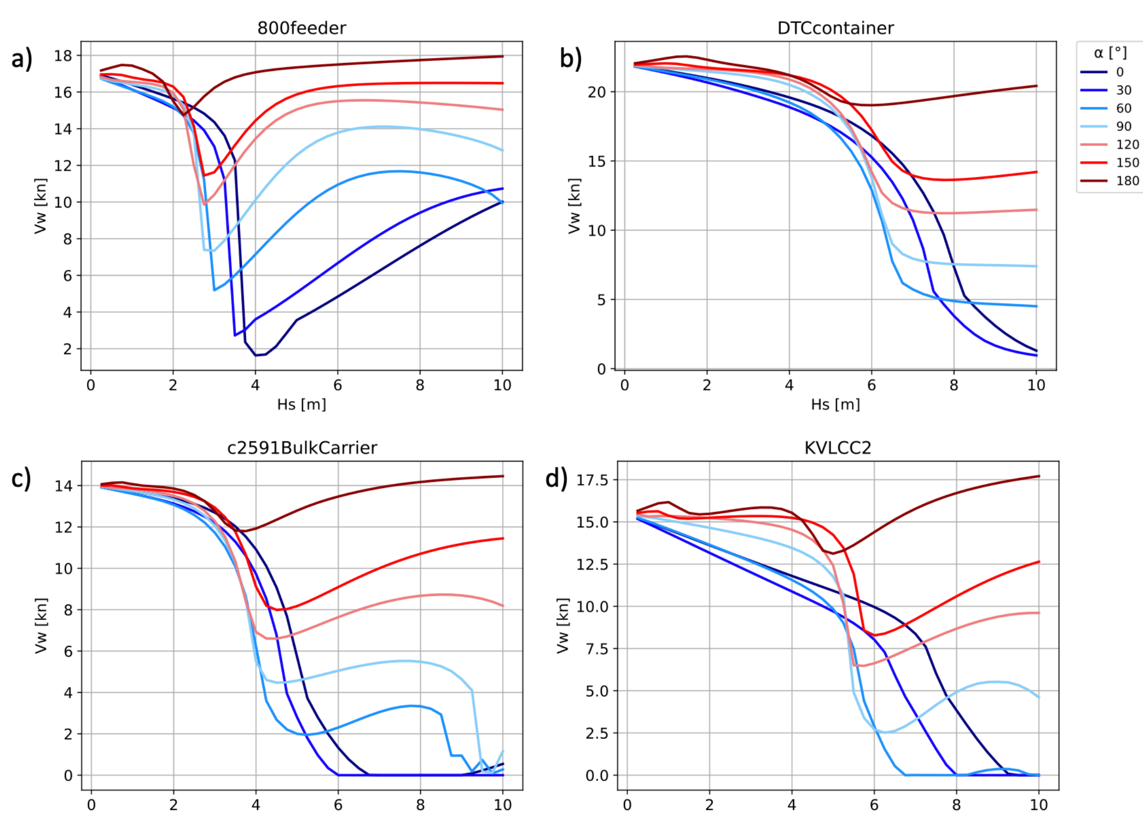

Figure 3.17: Sustained speed at different heading and wave height for: a) 800feeder, b) DTCcontainership, c) c2591bulkcarrier, d) KVLCC2. CTH oblique seas formula is used for resistance. DPM method used for power.

Ship total resistance

bateau also provides the total resistance R_t which correspondS to the predicted sustained speed V_w in Fig. 3.17.

The results in Fig. 3.18 confirm the cause-effect relationship between R_t and V_w: The resistance $R_t(H_s)$ increases towards a peak leading to the highest speed loss, and thus to the lowest sustained speed V_w. $R_t(\alpha)$ decreases with increasing angle of attack α, which leads to a rise of speed V_w.

An interruption of the curves of R_t in panels c) and d) coincide with null values of V_w in Fig. 3.17. This is due to negative roots given by the solver.

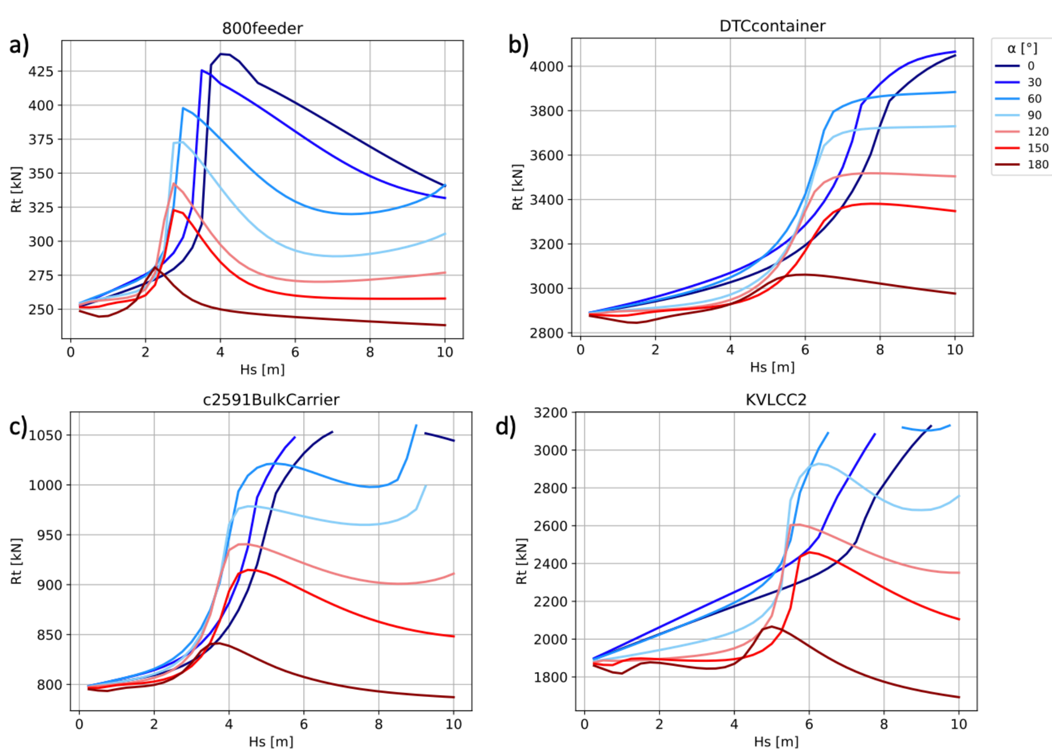

Figure 3.18: Corresponding ship resistance to sustained speed in Fig. 3.17

3.5 CO_2 emissions rate

Besides the sustained speed, the CO_2 emissions rate is also needed for the simulation of the least-CO_2 routes via VISIR. The CO_2 emission rate is computed for each potential leg of the voyage to be optimised, as it will be shown in Chap. 4. Usually, it depends on both the specific fuel consumption and power. However, in this study the specific value of SFOC depends only on the engine load. This means that the CO_2 emissions rate is independent of the sea state.

Four main engines were tested with both versions in dual fuels (HFO as pilot fuel and LNG as alternative fuel) or only HFO fuel. For each ship type, the engine is selected based on its main hull dimensions as explained in Sect. 2.1.4. The type of the propeller chosen is the fixed pitch propeller (FPP), the most commonly used in large ships. The engine names, the corresponding specified maximum continuous rating power MCR and speed V_{SMCR} are shown in Tab. 3.2.

In the case of HFO fuel, the CO_2 emission rate is computed as in Eq. 2.74 considering an emission factor $E_f = 3.114g/g$ as shown in Tab. 2.4. Instead for dual-fuel engine, the CO_2 rate is estimated as following:

$$\frac{dCO_2}{dt} = P_B \cdot (\text{SFOP} \cdot E_f(HFO) + \text{SGC} \cdot E_f(LNG)) \tag{3.5}$$

where SFOP and SGC refer to the specific fuel and gas consumption. $E_f(HFO)$ and $E_f(LNG)$ are the mass-based emission factor for HFO and LNG as shown in Tab. 2.4.

Fig. 3.19 shows notably high CO_2 emissions in the case of the DTC container ship. This is due to its high speed V_{SMCR} and large hull. Compared to the other ships the emissions decrease for smaller hulls.

Depending on the fuel, also CO_2 emissions vary: the dual fuel engine induces less CO_2 emissions than the HFO fuel engine, and the gap between both engines grows with increasing engine load.

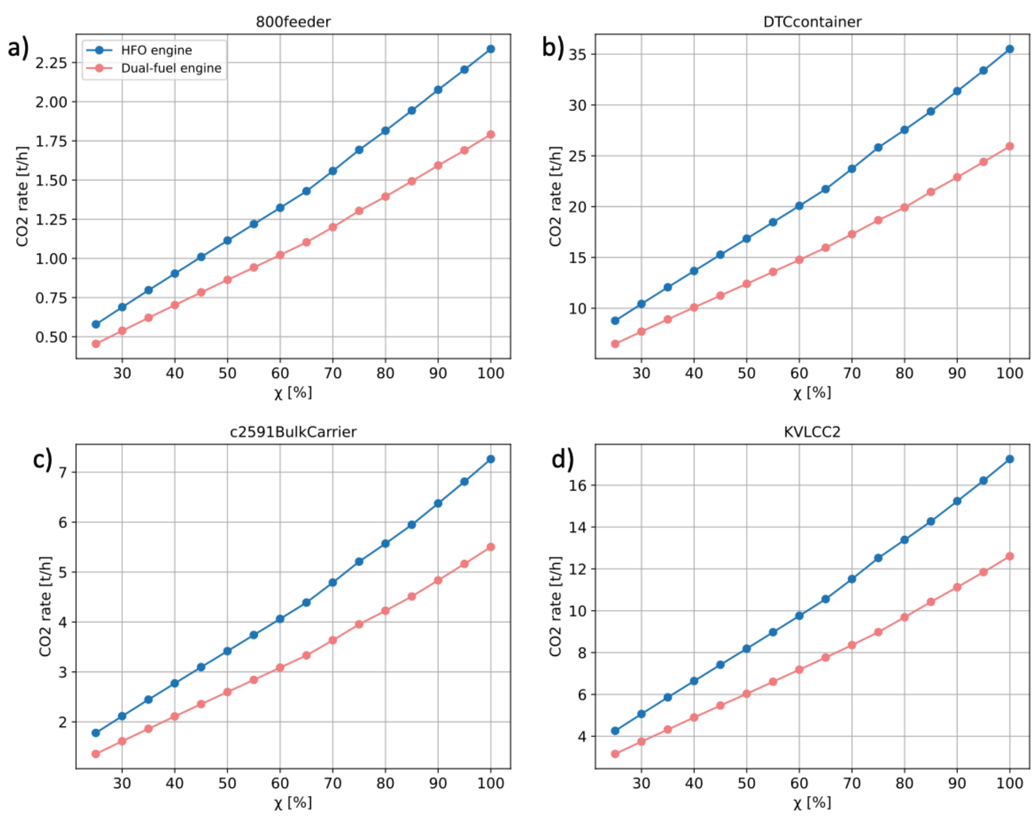

Figure 3.19: CO_2 emissions rate of dual-fuel and HFO engines for four ships: a) 800feeder, b) DTCcontainership, c) c2591bulkcarrier, d) KVLCC2

Chapter 4

Route optimization numerical experiments

bateau was developed to describe the performance of large vessels in a seaway through the sustained speed and the CO_2 emissions rate. This module is used in the ship weather model VISIR to simulate the optimal routes in the presence of dynamic ocean fields.

In this present study, the *bateau* -VISIR coupling is done "offline": Firstly, *bateau* is run for a specific vessel in idealized sea conditions. Then, the resulting database of sustained speeds is converted into an interpolating function to be ingested by VISIR. The latter runs with realistic ocean fields from data-assimilative models to return various types of optimal routes and their metrics.

This chapter begins by describing the setting of *bateau* and VISIR-2 for the case study in Sect. 4.1. Then, the outcome of the optimal routes simulations is presented in Sect. 4.2 with a focus on the role of significant wave height and direction.

4.1 Setting for the case study

This section is dedicated to showing the parametrization of ship resistance and power computation set in *bateau* for the vessel case study in Sect. 4.1.1. The simulations set-up in VISIR-2 regarding the domain, the graph, various selected harbours, and metocean conditions are described in Sect. 4.1.2. Then, the coupling procedure of both VISIR-2 and *bateau* is shown in Sect. 4.1.3.

4.1.1 *bateau* setting

Vessel case study

Containerships are cargo ships that carry manufactured goods, usually sold directly to end consumers that may want to reduce the passthrough costs. Consumer pressure to abate GHG emissions from ships is particularly felt in this vessel type segment, unlike bulkers and tankers [LR, 2022b].

The feeder containerships (they 'feed' larger cargo ships with containers) is one of the main ship types crossing the Asian waters. A bottom up study conducted by Lloyd's Register based on the analysis of AIS data, found that a feeder fleet of 222 vessels operating regionally between Singapore and other Asian countries consume about 1.4 million tons of fuel oil equivalent corresponding to 4.7 million tons of CO_2 emitted per year (0.4% of global shipping CO_2 emissions in 2018) [LR, 2022b]. Thus, the ship chosen for evaluating its response function via *bateau* and its optimal routes via VISIR is a feeder container ship of 800TEU (S05). Its main hull dimensions are presented in Tab. 3.1 and propulsion parameters in Tab. 3.2.

Sustained speed parametrization

The total ship resistance is taken into account in the estimation of the sustained speed as shown previously in Sect. 2.2.6. The calm water resistance is computed using the [Holtrop and Mennen, 1982] formula. The wave-added resistance considering various encountered wave direction is parametrized using the CTH formula for oblique seas (Eq. 2.46).
The Direct Power Method is used for the required power computation set-up. Then, assuming that the ship sails at a fixed engine load of 70% in wave height up to $10m$, the sustained speed is estimated according to the procedure shown in Sect. 2.3.2 for various relative wave directions.
The CO_2 emissions rate is computed as shown in Sect. 2.4 considering a dual-fuel engine of specified maximum continuous rating power $P_{SMCR} = 13,750kW$. The fuel-based emission factors E_f used correspond to the pilot fuel oil HFO and the gas LNG.

4.1.2 VISIR-2 setting

This section deals with setting up of the VISIR model for the case study simulations regarding the case study domain and the various harbours between voyages. In addition, the static environmental datasets (bathymetry), the metocean conditions namely waves, and wave climate are described.

Domain and graph

In VISIR, the whole graph is used to ensure that no suboptimal routes are found. However, this could significantly increase the computing time. This issue can be limited by using two or more smaller graphs, whose domains are carefully chosen to include all possible diversions of the optimal routes.
In this study, two domains encompassing the Maritime Silk Road[1] are selected to demonstrate the joint outcome of *bateau* and VISIR: North Indian Ocean and South China Sea (Tab. 4.1). The graph used in the route optimization is characterized by a grid spacing $\Delta x = 1/8°$. which means a linear resolution of 7.5 nmi in the meridional direction for both NIO and SCS. Moreover, the graph nodes are linked by up to four-hop edges which implies a level of

[1] `https://en.wikipedia.org/wiki/Maritime_Silk_Road`

connectivity equal to four [Mannarini et al., 2019c].

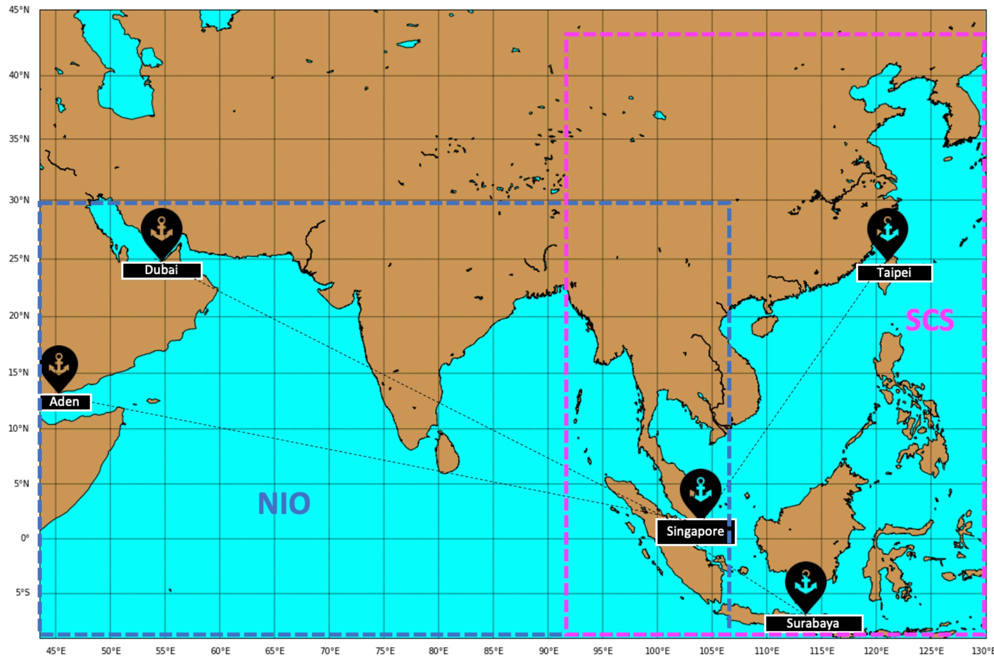

Figure 4.1: Domains and harbours selected

Table 4.1: NIO and SCS domains geographic coordinates

Domain	**Min latitude** [°]	**Max latitude** [°]	**Min longitude** [°]	**Max longitude** [°]
NIO	-5	30	43.5	106
SCS	-9	30	92	130

Harbours

Five of the main ports in NIO and SCS were considered for running VISIR: Singapore, Dubai, Aden, Surabaya, and Taipei. The port of Singapore has a strategic location. It is ranked as the top maritime capital of the world since 2015 and the world's second busiest port in term of total shipping tonnage[2]. In NIO, Dubai harbour in the United Arab Emirates and the port of Aden located in the northern coast of the Gulf of Aden were chosen. Surabay port is the second busiest sea port in Indonesia[3]. In SCS, Taipei port is considered the biggest container facility in the north of Taiwan[4].

As seen from Fig. 4.1, the NIO domain includes Aden, Dubai and Singapore harbours. The SCS also covers Singapore, besides Surabaya and Taipei harbours. The geographic coordinates are shown in Tab. 4.2.

[2] `https://en.wikipedia.org/wiki/Port_of_Singapore`
[3] `https://en.wikipedia.org/wiki/Port_of_Tanjung_Perak`
[4] `https://www.marineinsight.com/know-more/8-major-ports-of-taiwan/`

Table 4.2: Harbours geographic coordinates

Harbour name	**Harbour code**	**Latitude** [°]	**Longitude** [°]
Aden	YEADE	12.800	45.033
Dubai	AEDXB	25.278	55.294
Singapore	SGSIN	1.264	103.840
Surabaya	IDSUB	-7.120	112.733
Taipei	TWTPE	25.251	121.376

Static parameters and metocean conditions

VISIR-2 considers both static (bathymetry) and dynamic (currents, waves) environmental fields. The present study takes into account the bathymetry, the derived shoreline, and waves.

- Bathymetry

  The bathymetry serves to ensure that the sailing operation does not occur in shallow water. Furthermore, if it is accurate enough it can also be used for obtaining an approximation of the shoreline. In VISIR, the EMODnet bathymetric database[5] is used with a high spatial resolution of 1/16 arc minute or about $120m$ in the meridional direction following a specific procedure: An under keel clearance map $UKC = z - T$ is computed considering the bathymetry map (z) and the vessel draught (T). The contour line at $UKC = 0$ defines a pseudo-shoreline, which is used in VISIR to avoid the crossing of landmass [Mannarini et al., 2021].

- Waves

  Sea state analysis fields are obtained through CMEMS (Copernicus Marine Environment Monitoring Service)[6] from the operational global ocean analysis and forecast system of Météo-France. It is based on the wave model MFWAM which is a third-generation wave model using the assimilation of wave height. The product is identified as GLOBAL_ANALYSIS_FORECAST_WAV_001_027[7].
  Significant wave height and direction fields (VHM0 and VHM0_DIR) are obtained from the daily analyses of 1/12 degree spatial resolution and 3-hourly-instantaneous temporal resolution.

Wave climate

The North Indian Ocean is divided into two semi-enclosed seas: the Arabian Sea (AS) and the Bay of Bengal (BoB).
[Anoop et al., 2015] analyzed the European Centre for Medium-Range Weather Forecasts

[5] https://www.emodnet-bathymetry.eu/data-products
[6] http://marine.copernicus.eu/
[7] https://resources.marine.copernicus.eu/product-detail/GLOBAL_ANALYSIS_FORECAST_WAV_001_027/INFORMATION

(ECMWF) global atmospheric reanalysis product (ERA-Interim) for the period 1979 – 2012 and found that the annual average significant wave height of the NIO ranges from 1.5 to 2.5m and the seasonal average is the highest ($3-3.5m$) during the monsoon period [June-September]. During the summer monsoon, the average wave height reaches its maximum ($3-3.5m$) in the western AS due to the strong cross-equatorial winds of the Somali jet [Findlater, 1969]. Wave height is lower in the BoB especially in the western part due to the weaker wind in the monsoon and the sheltering effect of Sri Lanka's orography [Anoop et al., 2015].

South China Sea is also affected by seasonal monsoons. The northeast monsoon happening in winter leads to the rise of the significant wave height compared to the southwest monsoon in summer [Zheng et al., 2014].

4.1.3 VISIR-*bateau* coupling

As shown in Fig. 3.1, *bateau* provides the sustained speed in rough seas and the CO_2 emissions rate. The inclusion of the aforementioned outputs into VISIR-2 requires the transformation of this database into a function, to be evaluated at the specific sea conditions encountered along the route. This is realised through a B-spline[8] interpolation. Then, VISIR-2 uses metocean informations as described in Sect. 4.1.2, to provide the optimal routes for a specific set of graph parameters and environmental conditions.

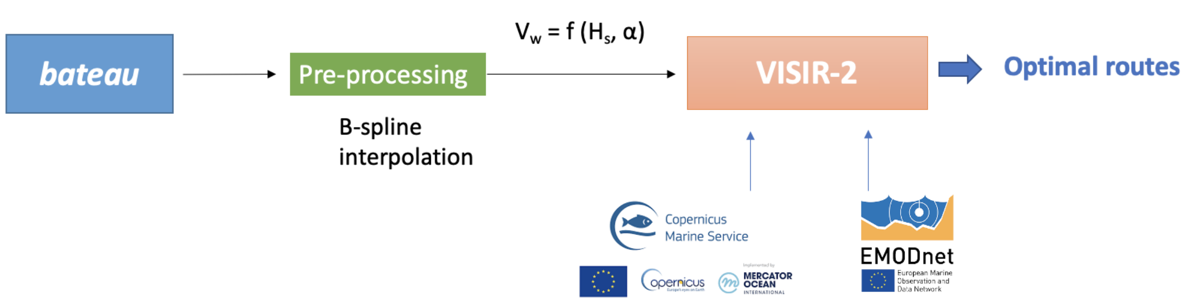

Figure 4.2: Architecture of VISIR-*bateau* coupling

4.2 Results

Numerical simulations of the optimal routes were performed for the sea conditions of both February and July 2020. The first day of each month was assumed to be the starting day of each voyage. Routes were chosen to either originate or end at Singapore, so that waves are encountered at different times during the voyage and from different angles relative to sailing direction.

The results of the optimal route simulations in the NIO and SCS domains are discussed in

[8] `https://docs.scipy.org/doc/scipy/reference/generated/scipy.interpolate.BSpline.html`

Sect. 4.2.1 and Sect. 4.2.2 respectively. More focus on the role of wave direction is provided in Sect. 4.2.3.

4.2.1 Optimal routes in NIO

Numerical simulations were done departing from Singapore and sailing to Dubai in NIO, in both February and July 2020.

In Fig. 4.3, the significant wave height H_s field and two optimal routes are shown. Following the new representation introduced in [Mannarini et al., 2021], the H_s field is displayed via grey tones at three-hourly timesteps, through concentric shells centred at the origin of the route (yellow star). Every 24 hours an isoline (red dashed line) joining all locations reachable from the origin after a navigation time of an additional 24 hours with respect to the previous isochrone is also displayed. The optimal routes shown on the map are: the least-distance one or geodetic route (in blue) and the least-CO_2 route (in green).

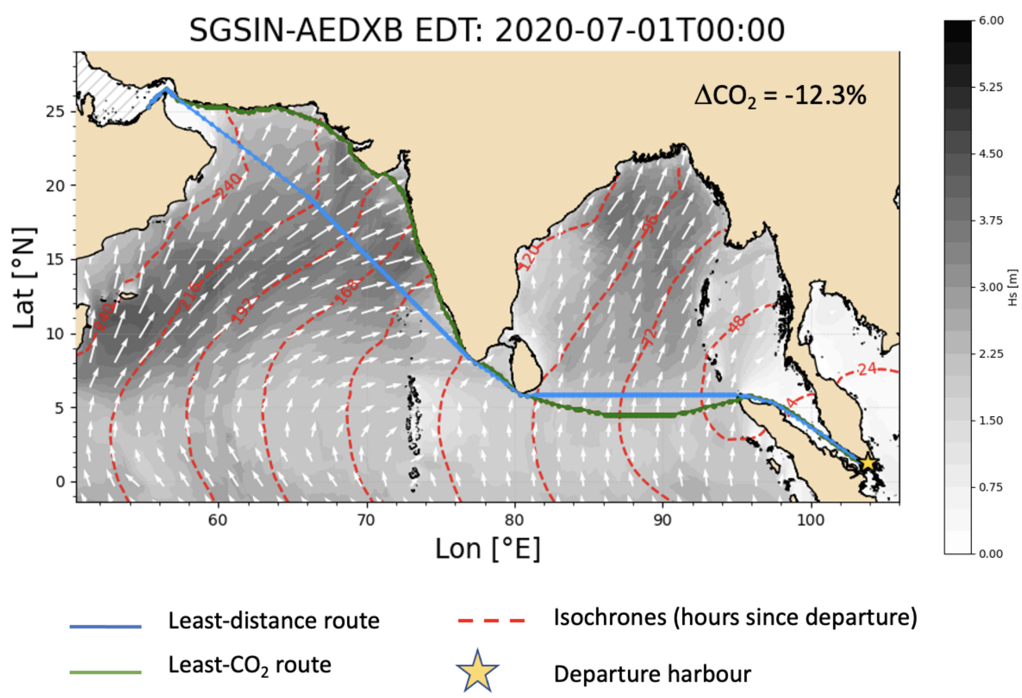

Figure 4.3: Optimal routes and significant wave height field for departure at Singapore at 00 UTC of July 1st, 2020 and destination Dubai. The CO_2 saving of the green with respect to the blue route is also given.

In order to obtain greater insight into the results shown in Fig. 4.3, the H_s and SOG profiles along the optimal routes are displayed in Fig. 4.4. First, it is noted that the least-CO_2 route sails into calmer seas, especially in the AS, where the Hs is up to one meter lower. As seen from Fig. 4.4, this leads to larger sustained speeds, about two knots more, than along the least-distance route. This follows from the lower wave-added resistance experienced (panel a) in Fig. 3.17). However, the vessel response does not only depend on significant wave height but also on relative wave direction, and this will be investigated later, in Sect. 4.2.3.

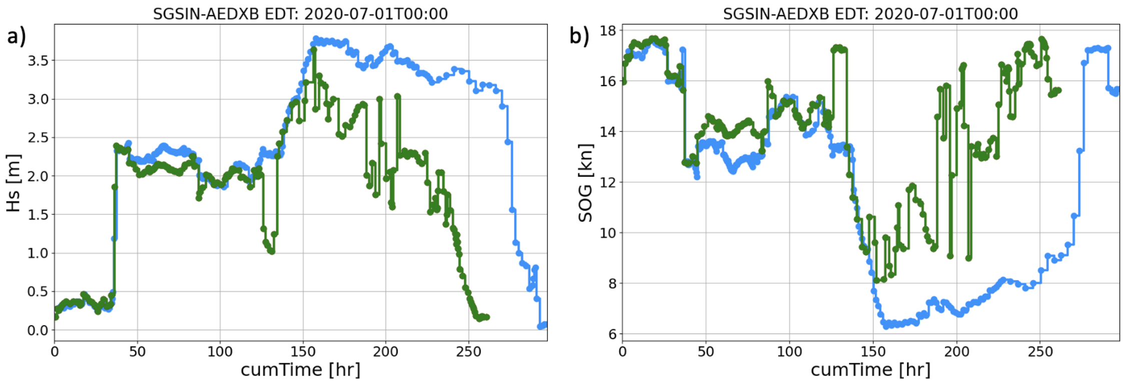

Figure 4.4: Corresponding significant wave height profile (panel a) and Speed Over Ground (panel b) to the optimal routes in Fig. 4.3

Further numerical experiments were performed from Singapore to Aden, and compared to the previous simulations from Singapore to Dubai. The results presented in Fig. 4.5 show more CO_2 saving in July than in February for both routes. The reason is that in the NIO, especially in the AS, the wave height is higher in summer than in winter reaching about $4m$, due to the summer monsoon and the Somali Jet. Moreover, the encountered wave at an angle $|\alpha| \leq 60°$ with respect to the sailing direction (panels c and d), make the optimal route diverge to avoid those waves. Indeed for $H_s \geq 3m$, head and bow seas cause high resistance thus lower sustained speed. This effect follows from the ship resistance values shown in the panels a) of Fig. 3.17 and Fig. 3.18.

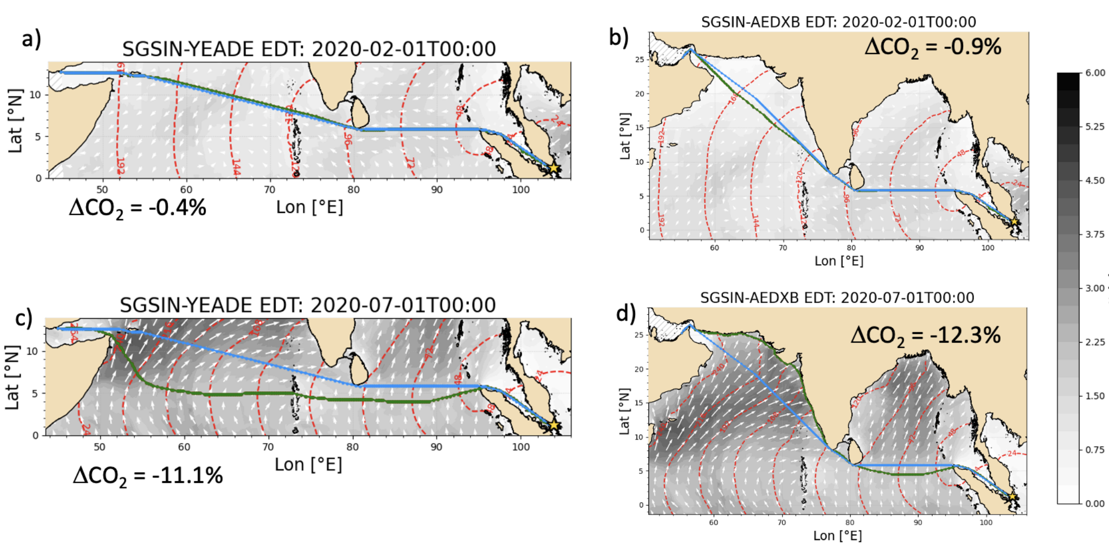

Figure 4.5: Least-CO_2 routes from Singapore to Aden in February (panel a) and July (panel c), and from Singapore to Dubai in February (panel b) and July (panel d). The blue line is the least-distance route; the green line refers to the least-CO_2 route.

More simulations were also performed departing from either Dubai or Aden back to Singapore as seen in Fig. 4.6 and Fig. 4.7. The results show a clear impact of the month of voyage on the simulated routes: In February, significant wave heights are notably lower than $2m$ which makes the least-CO_2 routes come closer to the geodetic routes. Instead, in July, the wave heights are higher and the effect of wave direction becomes more prominent.

Thus, a major CO_2 emissions saving up to 12% is noted with respect to the geodetic one and a diversion of the optimal route avoiding rougher seas.
The magnitude of CO_2 saving and the optimal route are different between voyages with swapped departing harbour. This is because waves are encountered by the vessel at different times and at different relative angles. More insight regarding the role of wave direction is shown in Sect. 4.2.3.

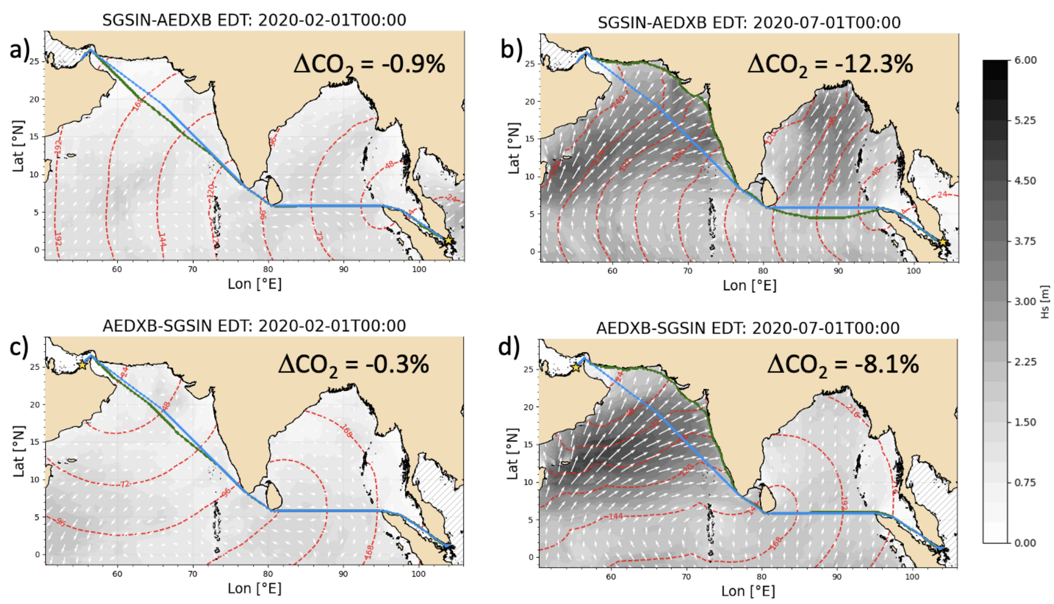

Figure 4.6: Least-CO_2 routes Singapore-Dubai in February (panel a) and July (panel b) and Dubai-Singapore in February (panel c) and July (panel d)

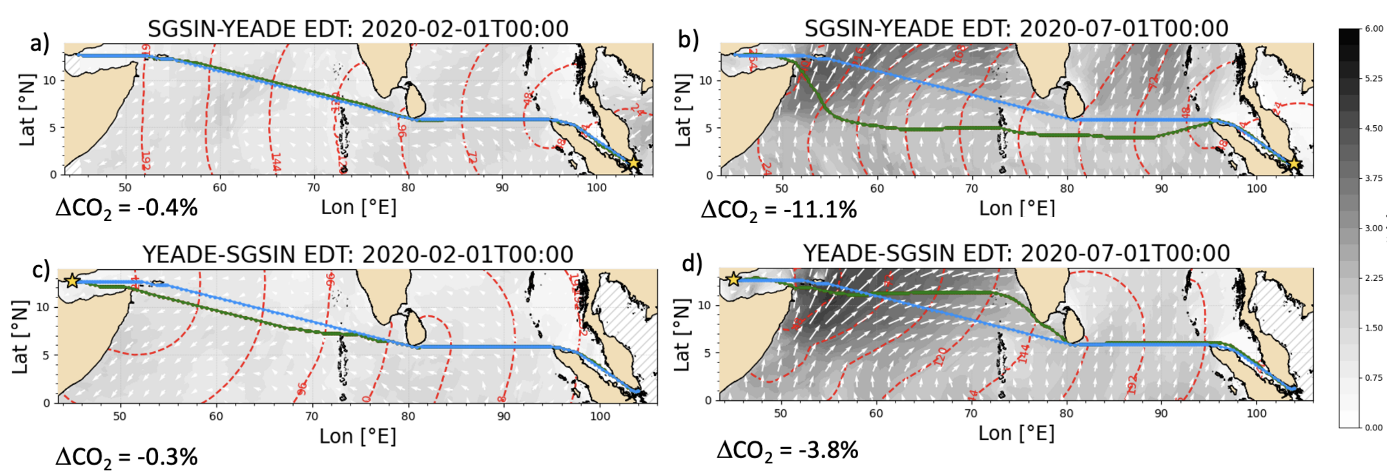

Figure 4.7: Least-CO_2 routes Singapore-Aden in February (panel a) and July (panel b) and Aden-Singapore in February (panel c) and July (panel d)

4.2.2 Optimal routes in SCS

In order to evaluate the impact of different ocean regions on the optimal routes, further numerical simulations were carried out from Singapore to Surabaya and Taipei in SCS domain. Generally, the routes presented in Fig. 4.8 lead to less CO_2 emissions saving than those in NIO shown previously in Fig. 4.5. In SCS, wave height values were higher in February than in July, and this leads to lower CO_2 emissions saving. An effect of wave directions is also noted for instance in the panel b) of Fig. 4.8 where the CO_2 saving reach about 2%. This is because the encountered head waves causing the major resistance so the VISIR's algorithm suggest a path to avoid those waves by increasing the angle between the sailing direction and the wave angle of attack. By contrast, the following waves encountered, seen in the panel d), are favourable to push towards the geodetic route.

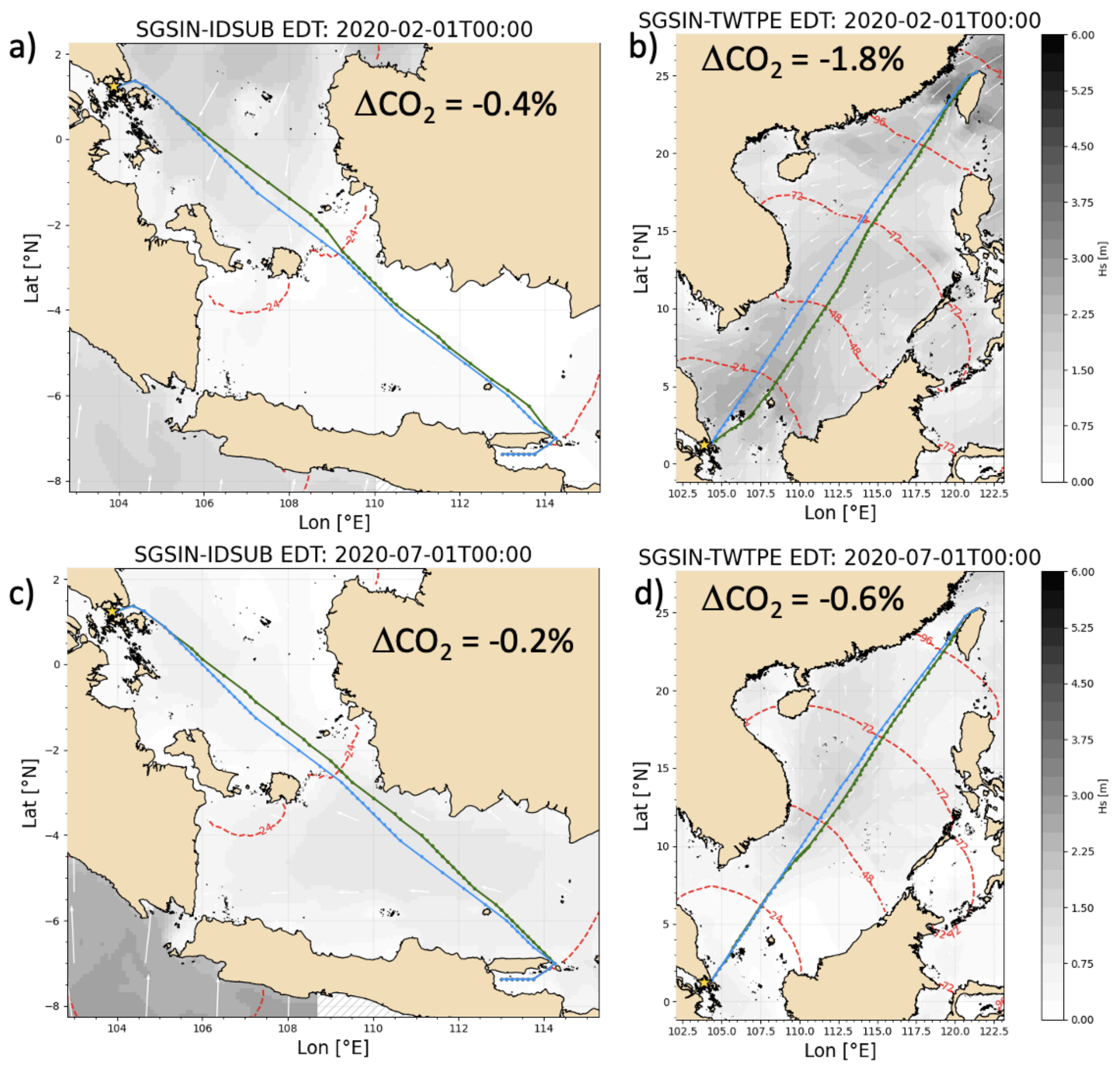

Figure 4.8: Least-CO_2 routes from Singapore to Surabaya in February (panel a) and July (panel c). Singapore to Taipei in February (panel b) and July (panel d)

As for the routes in NIO, other numerical experiments were carried out from Surabaya and Taipei back to Singapore as seen in Fig. 4.9 and Fig. 4.10. Unlike NIO, in SCS domain the least-CO_2 routes did not vary significantly according to the month of voyage, especially for Singapore-Surabaya voyages where $H_s \leq 1m$. Swapping departure harbour in this domain does not show a relevant difference in terms of CO_2 saving.
The results show that the benefit deriving from ship weather routing depends on the route domain and its wave climate. However, more systematic runs are required to assess the role of metocean conditions on the route topology and CO_2 savings [Mannarini and Carelli, 2019a].

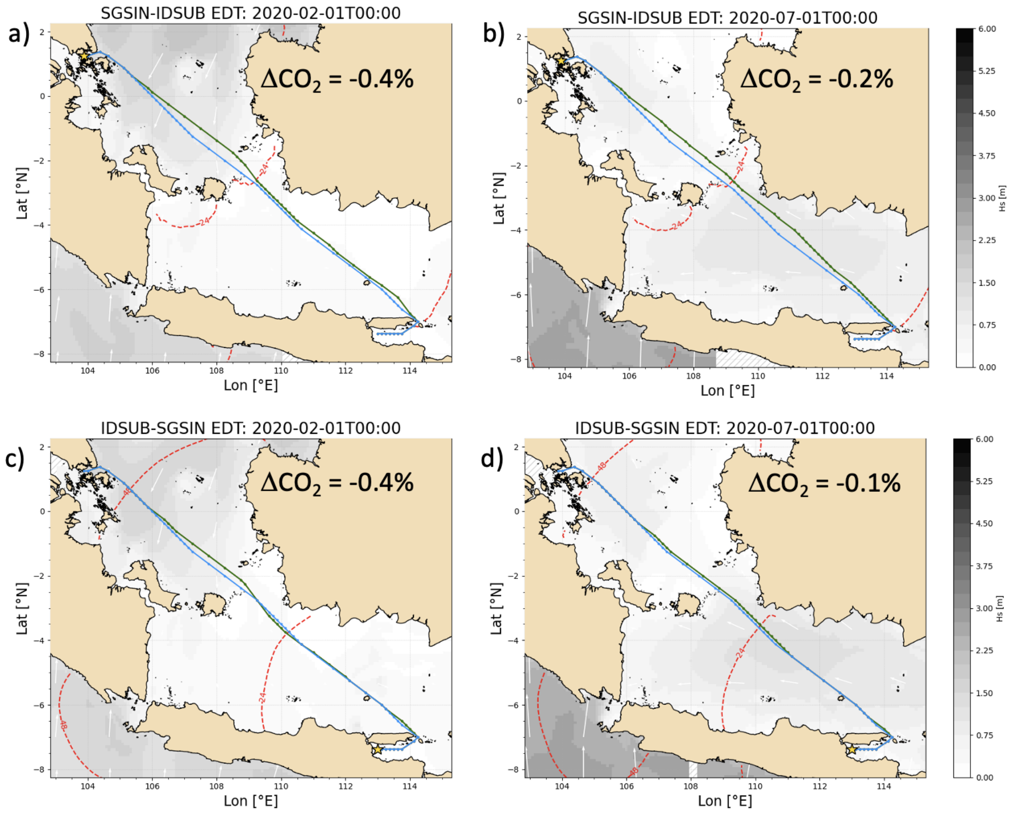

Figure 4.9: Least-CO_2 routes Singapore-Surabaya in February (panel a) and July (panel b) and Surabaya-Singapore in February (panel c) and July (panel d)

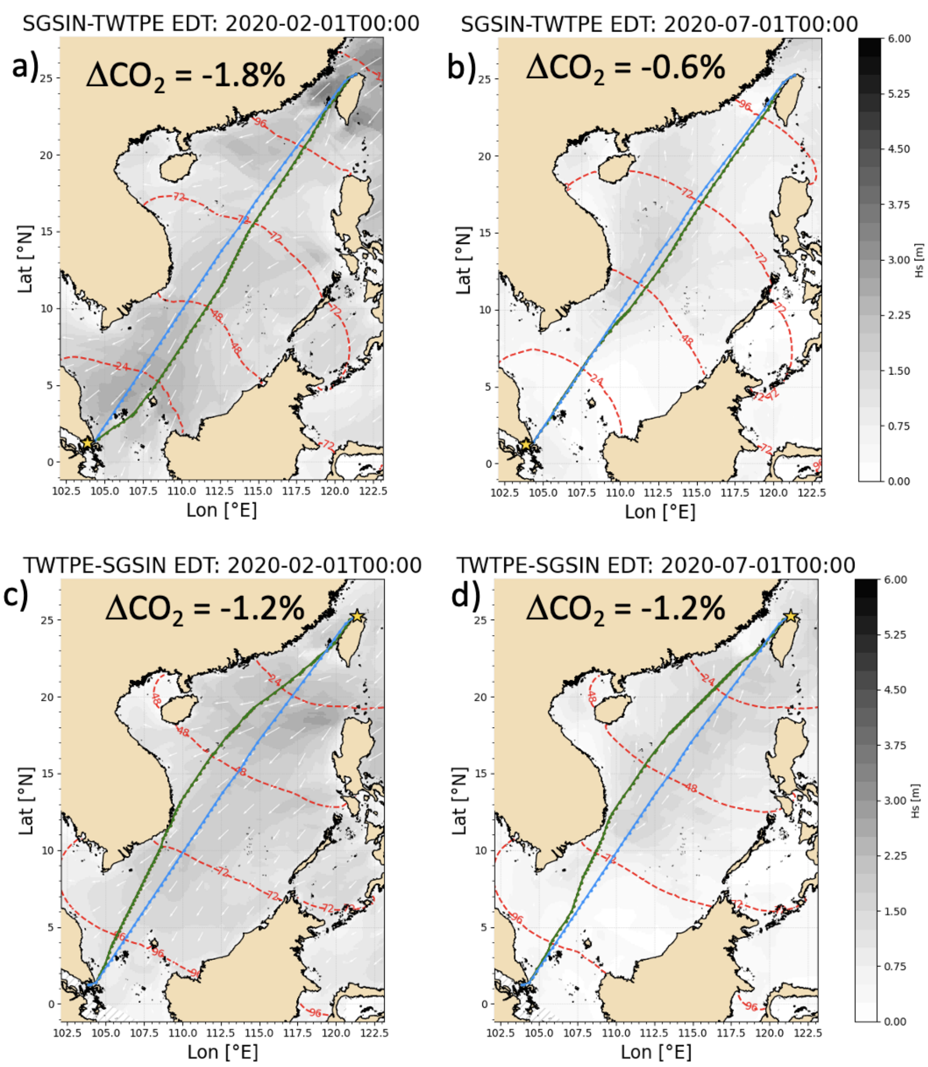

Figure 4.10: Least-CO_2 routes Singapore-Taipei in February (panel a) and July (panel b) and Surabaya-Taipei in February (panel c) and July (panel d)

4.2.3 Role of wave direction on least-CO_2 routes

In order to investigate the role of wave direction on least-CO_2 routes, numerical simulations were done with a fixed wave direction $\alpha = 0°$ (Fig. 4.11) and with wave directions from CMEMS fields (Fig. 4.12). Another departure day for the voyage starting from the 10th of February was considered.

As seen from the H_s and SOG profile in Fig. 4.11, while the green route (least-CO_2 route) is seeking lower wave height H_s where it can maintain as much as possible the maximum sustained speed, it diverges towards the geodetic route. This makes the CO_2 saving nearly zero.

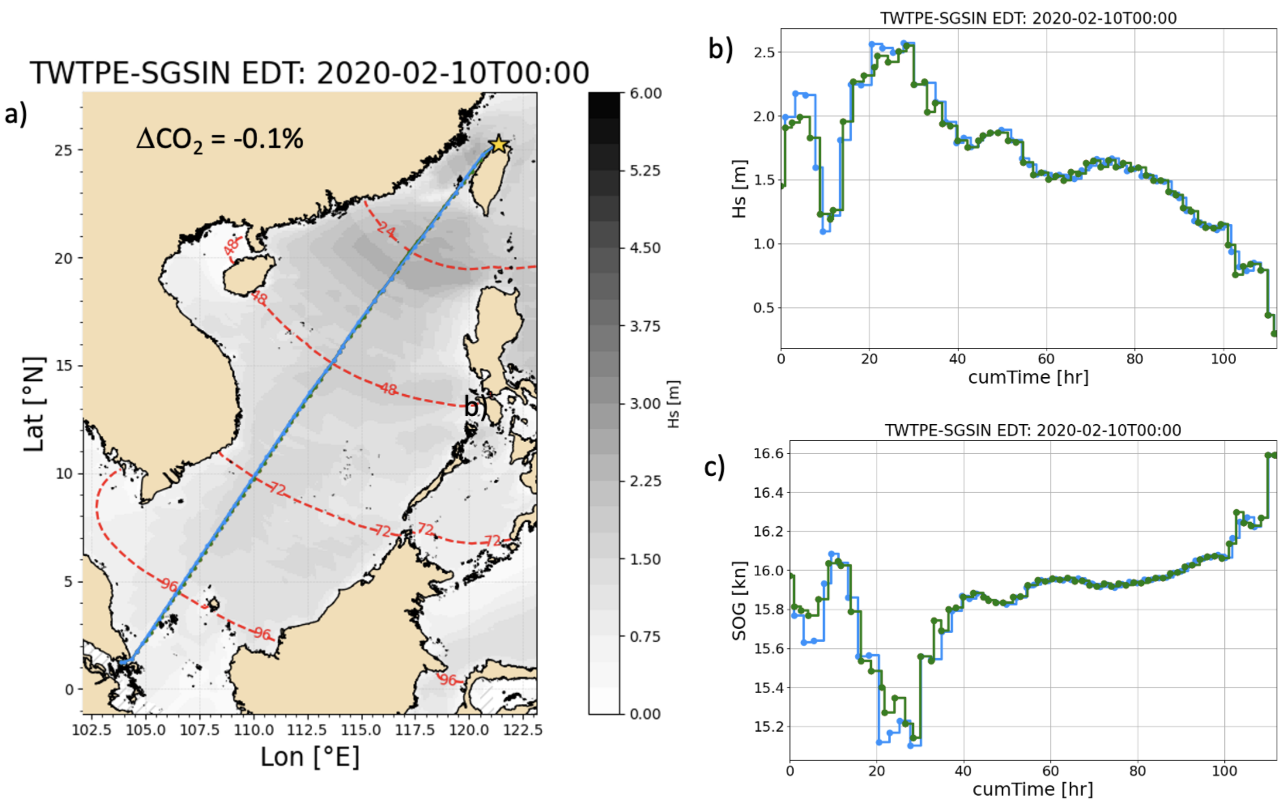

Figure 4.11: Least-CO_2 routes Taipei-Singapore in February in panel a). The corresponding significant wave height and speed over ground profiles are in panels b) and c) respectively

In Fig. 4.12, the results show that the optimal CO_2 route seeks to avoid the areas where the wave height and direction lead to higher resistance: For $H_s \leq 2m$ the feeder diverges towards lower wave angle of attack with respect to the geodetic route. Instead, for $H_s \geq 2m$, the vessel follows its green path towards larger α leading to higher sustained speed as seen in panel c) (lower speed loss and resistance also). This is consistent with the results shown in panel a) of Fig. 3.17, where a relevant effect of wave direction on the sustained speed for $H_s \geq 2m$ (greater effect of ship motions) can be seen.

The aforementioned results prove a dependence of the optimal CO_2 route on both wave height and direction especially in long waves. However, more numerical experiments for further voyages and vessels are needed to confirm this.

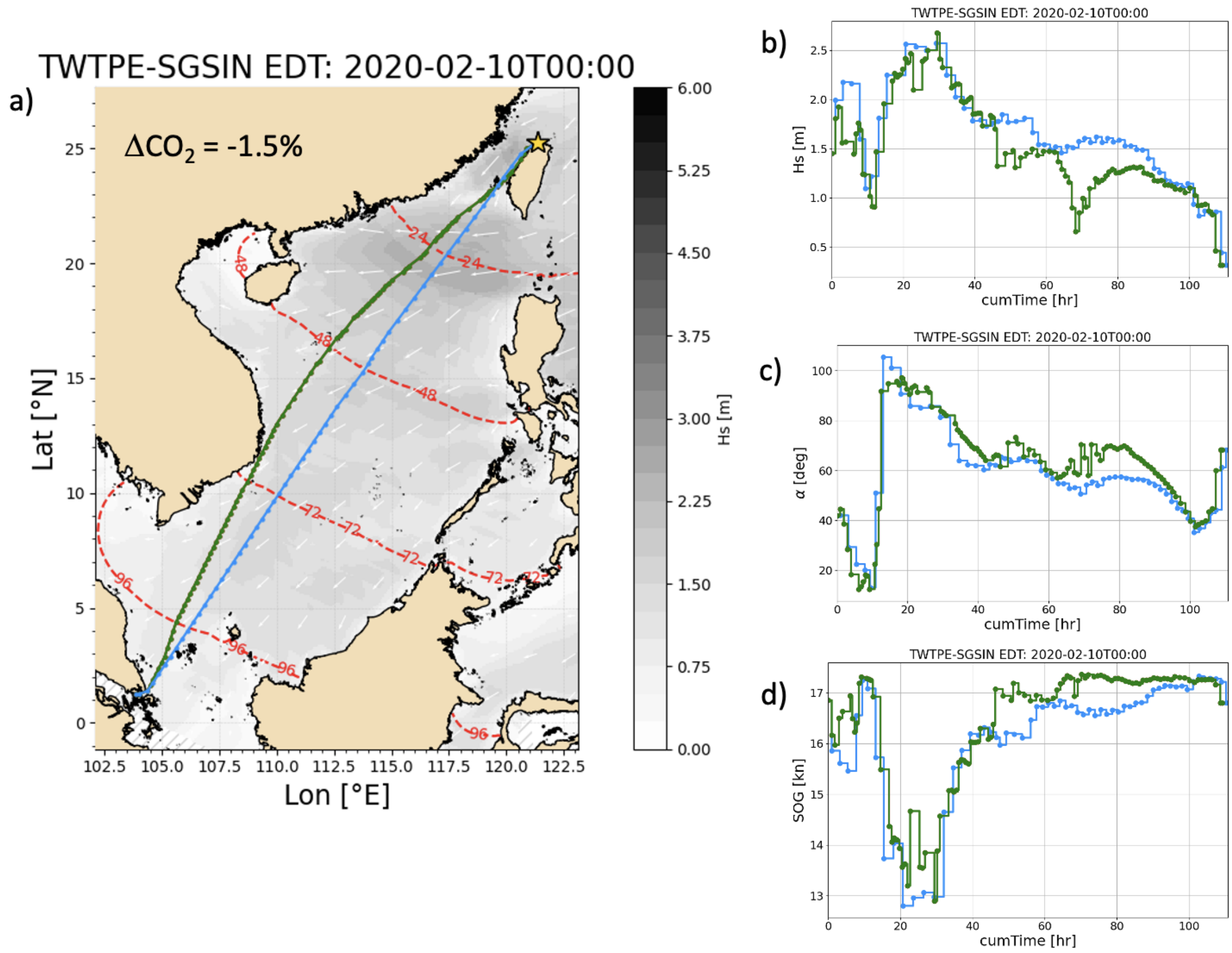

Figure 4.12: Least-CO_2 routes Taipei-Singapore in February in panel a). The corresponding wave height, wave direction and speed over ground profiles are in panels b), c) and d) respectively

Chapter 5

Conclusion and future prospects

5.1 Summary

With the climate crisis-but also the increasing pressure from regulatory institutions, moneylenders, and consumers to address it-reducing the carbon footprint of the maritime transport is now a priority.

The contribution of maritime transport to global GHG emissions and its potential on mitigating climate change was reviewed in Sect. 1.1. Then, delving into shipping decarbonization regulations and measurements in Sect. 1.2 and Sect. 1.3, ship weather routing is considered among the operational options available in the short-term decarbonisation roadmap. In this context, the VISIR ship routing model presented in Sect. 1.4 is a tool for computing optimal routes and saving CO_2 emissions. However, VISIR was missing a dedicated component to represent the speed loss of large ships taking into account the effect of waves directions. This thesis aims to fill this gap by developing a ship performance module called *bateau* .

First, a database of hull parameters for vessels of various type and size was built (Tab. 3.1 and Tab. 3.2). Parameters regarding the hull geometry and superstructure were collected from literature or computed through some approximations as noted in Sect. 2.1. A parametrization of the ship's longitudinal resistance deriving from several physical effects was carried out. Two formulae were tested for calm water resistance [Holtrop and Mennen, 1982] and [Kristensen and Bingham, 2017] (Sect. 2.2.3), several formulae for wave-added resistance in head seas, and the CTH formula in oblique seas (Sect. 2.2.4). The wind resistance was computed as recommended by [ITTC, 2017e] using [Fujiwara et al., 2005] regression formula (Sect. 2.2.5). The computation of the delivered power required in a specific environmental condition considered both the resistance and thrust identity method (RTIM) and the direct power method (DPM) which involves the propeller efficiency (Sect. 2.3.1). The power balance between the delivered power by the main engine and the power dissipated at the propeller, delivers the sustained speed (Sect. 2.3.2). The latter is needed in VISIR, in addition to the hourly CO_2 emissions rate. This way, a database of vessel speed as a function of significant wave height, angle of attack, and engine load factor, is prepared for four different vessels namely, as shown in Sect. 3.4.2: a bulk carrier, a feeder, the DTC containership and the tanker KLCC2.

Numerical simulations of least-distance and least-CO_2 routes through the VISIR model were carried out in the sea domains corresponding to the maritime silk road: South China Sea and the North Indian Ocean, as shown in Fig. 4.1. The numerical set-up for both *bateau* (resistance, power, sustained speed) and VISIR (domain, graph, metocean fields) were described in Sect. 4.1. The optimal routes were computed from Singapore to four other harbours namely Dubai, Aden, Surabaya and Taipei (Sect. 4.2) for February and July 2020. Then further numerical simulations were performed swapping the departure port. The role of wave direction on least-CO_2 routes was also assessed.

5.2 Findings

Numerical computation of ship resistance and sustained speed using *bateau* were performed in idealized conditions, i.e. assuming forcing by monochromatic plane waves. Testing several ship types, the results show higher calm water resistance for the blunt hulls (tankers and bulkers) compared to containerships with slender hulls (Sect. 3.3.1). It was found that [Holtrop and Mennen, 1982] formula delivers higher values than [Kristensen and Bingham, 2017] formula, and that the viscous component is dominant at low speeds.

Wave-added resistance was estimated in regular waves regime assuming a wave steepness $H_s/\lambda = 1/23$. The comparison with observations from literature show that the accuracy of each semi-empirical formula depends on hull geometry and speed, and whether the region of prediction is in short ($\lambda/Lpp < 0.5$) or long waves ($\lambda/Lpp > 0.5$) (Sect. 3.3.2). Generally, there is a lack of observations especially in oblique seas. Furthermore, little detail regarding wave steepness was found in the literature. So, further numerical tests were done using five values of steepness taken from [Lee et al., 2019]. An increase of the peak resistance due to waves with higher steepness and a linear dependence of the resonance was found. As the steepness affects ship resistance, it will also affect the sustained speed, thus it could be a source of uncertainty.

It was also found that a high vessel speed will increase the peak value of the wave-added resistance and shift its resonance to longer dimensionless wavelength λ/Lpp.

Besides the added resistance due to waves, wind could also be relevant especially for vessels with a high superstructure. This is seen in Sect. 3.3.3, where it was found a high wind-added resistance at a true relative direction ($\alpha \leq 45°$) was found, especially for large tankers and containerships. Instead, no effect was noted for the lateral wind, while a net thrust is produced from quartering and following wind ($120° \leq \alpha \leq 180°$).

The sustained speed in rough seas is based on solving a non-linear equation of power balance. The results show a drop of the sustained speed due to increasing wave height until a minimum which coincides with the resonance of wave-added resistance (Sect. 3.4.1). A consistent profile of sustained speed was found while testing several formulae of wave-added resistance (STA2, NTUA, and CTH). Numerical experiments using a feeder containership in head seas show that higher wave height decreases the sustained speed in rough seas compared to the one in calm water (Fig. 3.14). However, a minor impact of engine load on sustained speed was found. Four vessels (two containerships, one tanker and one bulker) were used for the numerical experiments, highlighting the dependence of the sustained speed's trend on the hull geometry. The sustained speed of the four vessels differs especially in the region of resonance, which is dominated by the heave and pitch motions. In oblique seas, the sustained speed is at the highest values in following waves, and decreases till head seas where the ship faces the highest resistance (Sect. 3.4.2). For very short wavelengths, wave-added resistance may turn and become negative in the presence of following waves.

For the aforementioned four vessels, the CO_2 emissions rate was computed considering two types of the same engine: HFO and dual-fuel engine.

A feeder containership was selected for the simulations of the optimal routes via VISIR model. The vessel response parametrized by *bateau* was then used for computing least-CO_2 routes using VISIR-2. The set-up of both *bateau* and VISIR-2, and their coupling were described in Sect. 4.1. Significant route diversions towards calmer waters were found for some routes in the North Indian Ocean, especially in northern-hemisphere summer and in the Arabian Sea Sect. 4.2.1. CO_2 savings up to 12% along the least-CO_2 route with respect to the geodetic one were computed.

This reveals the role of the season monsoon in NIO on the outcome of the ship weather model. It was also found that the role of wave direction becomes more prominent where the wave height exceeds $2m$. This is consistent with the sustained speed results computed via *bateau* in the panel a) of Fig. 3.17. On swapping the departure harbours in the voyage simulations, a difference in the optimal least-CO_2 route and the magnitude of of CO_2 emissions saving was noted. This was due to the waves encountered by the vessel at different times and at different relative directions.

The optimal routes simulated in SCS domain show a lower CO_2 saving compared to NIO. This is explained by the low wave height ($H_s \leq 2m$) in SCS especially in July (Sect. 4.2.2). The dependence of the sustained speed on wave direction within a semi-empirical parametrization was a new feature of this present work. To assess its role, further simulations of the optimal route from Singapore to Taipei were done at fixed wave direction and compared to the results while all wave directions from CMEMS fields were considered (Sect. 4.2.3). An impact of wave direction was found especially in long waves where ship motions are prominent.

The simulations results are specific to the chosen feeder and voyage domain, as well as *bateau* parametrization. Thus, more numerical experiments are needed to assess the generality of these findings.

5.3 Future prospects

So far, four ships were tested in the numerical experiments of sustained speed and a feeder containership in the simulation of optimal routes. However, further vessels and vessel types should be tested.

Moreover, an assessment of the uncertainty of the outputs of *bateau* is still missing. It is related to both the imperfect knowledge of the input parameters and to the approximations of the physical and mechanical processes.

According to the numerical results, the wind added resistance is relevant for ships with a high superstructure. However, its impact on sustained speed and on optimal routes computed via VISIR is still to be assessed.

So far, *bateau* was linked to VISIR offline through an interpolation function. A full integration of *bateau* into VISIR is therefore needed in the future work.

In this study, only waves were considered in the simulation of the optimal routes. Moreover, wind was just considered in *bateau* numerical experiments in idealized conditions but it was not yet used for computing least-CO_2 routes in VISIR. A step forward could be to include wind together with waves and currents, in the simulation of least-CO_2 routes.

Furthermore, numerical experiments using *bateau* and VISIR were done only in regular waves since the CMEMS waves product in the global domain does not provide the spectrum. Once the latter is available, more tests should be done also in irregular waves.

Finally, a consideration of the engine load diagram in *bateau* , could constrain the sustained speed within the heavy propeller limits.

Glossary

Table 5.1: List of acronyms

Acronym	**Name**
AIS	Automatic Identification System
AR6	Sixth Assessment Report of IPCC
AS	Arabian Sea
BoB	Bay of Bengal
CCS	Carbon Capture and Storage
CFD	Computational Fluid Dynamic
CII	Carbon Intensity Indicator
CMEMS	Copernicus Marine Environment Monitoring Service
CPP	Controllable pitch propeller
CTH	Chalmers Tekniska Högskola
DPM	Direct Power Method
EEA	European Economic Area
EEDI	Energy Efficiency Design Index
EEOI	Energy Efficiency Operational Indicator
EEXI	Energy Efficiency Existing Ship Index
EU	European Union
EU-ETS	European Trading System
FPP	Fixed pitch propeller
GHG	Greenhouse Gas
GT	Gross Tonnage
GWP	Global Warming Potential
HFO	Heavy fuel oil
IMO	International Maritime Organisation
IMO-DCS	IMO Data Collection System
IPCC	Intergovernmental Panel on Climate Change
ITTC	Interational Towing Tank Conference
LNG	Liquified Natural Gaz
MCR	Maximum Continous Rating
MDO	Marine diesel oil
MEPC	Marine Environment Protection Committee
MGO	Marine gas oil
NIO	North Indian Ocean
NMRI	National Maritime Research Institute of Japan
NMRI	National Maritime Research Institute
NO_x	Nitrogen oxides

NTUA	National Technical University of Athens
POW	Propeller-Open-Water characteristics
QNM	Torque and Revolution Method
RANS	Reynolds-averaged Navier-Stokes
RAO	Response Amplitude Operator
RSL	Relative speed loss
RTIM	Resistance and Thrust Identity Method
SCS	South china Sea
SDGs	Sustainable Developmental Goals
SEEMP	Ship Energy Efficiency Management Plan
SGC	Specific gas consumption
SFOC	Specific fuel oil consumption
SFOP	Specific pilot fuel oil consumption
SMCR	specific maximum continuous rating
SO_x	Sulphur oxides
SOG	speed over ground
STA-JIP	Sea Trial Analysis-Joint Industry Project
STW	speed through water
SZEF	Scalable Zero Emission Fuels
TEU	Twenty-foot equivalent
TRL	Technology Readiness Level
TRM	Thrust and Revolution Method
VLCC	Very large crude carrier
ZEV	zero emission vessel

Table 5.2: List of variables

Symbol	**Parameter**	**Unit**
ω	wave frequency	rad/s
α	angle of attack	deg
χ	engine load factor	%
Δ	displacement volume	mˆ3
η_H	hull efficiency	-
η_O	open water efficiency	-
η_R	relative rotative efficiency	-
η_S	shaft efficiency	-
λ	wavelength	m
μ	kinematic viscosity	mˆ2/s
ν	dynamic viscosity	N s/mˆ2

ψ_{WR}	apparent wind direction	deg
ρ	water density	kg/mˆ3
τ	propeller load factor	-
ζ_a	wave amplitude	m
A_{BT}	transverse bulb area	mˆ2
A_{OD}	lateral projected area of superstructure	mˆ2
A_{WP}	waterplane area	mˆ2
A_{XV}	maximum transverse area or frontal area	mˆ2
A_{YV}	lateral projected area above the waterline	mˆ2
A_e/A_o	blade area ratio	-
A_M	midship area	mˆ2
A_T	transom area	mˆ2
B	beam	m
C_{aa}	air resistance coefficient	-
C_{aw}	normalized added resistance	-
C_{MC}	centre of lateral projected area	-
C_{WP}	waterplane coefficient	-
C_a	incremental resistance coefficient	-
C_B	block coeffcient	-
C_D	wind drag coefficient	-
C_f	frictional resistance coefficient	-
C_M	midship coefficient	-
C_P	prismatic coefficient	-
C_r	residual resistance coefficient	-
C_s	calm water resistance coefficient	-
D_p	propeller diameter	m
D	ship depth	m
DWT	deadweight	teu
E_f	emission factor	-
F	deduction thrust force	N
F_g	gravitational forces	N
F_i	inertia forces	N
F_v	viscous forces	N
f_w	weather factor	-
g_0	gravitational acceleration	m/sˆ2
h	accommodation height	m
H_{BR}	height of top of superstructure	m
h_B	center of bulb area above keel line	m
H_C	height from waterline to centre of lateral projected area	m
H_s	wave height	m

i_E	angle of entrance	deg
J	advance speed ratio	-
k_1	form factor	-
k	wave number	-
k_{yy}	pitch radius of gyration	-
k_e	encountered wave number	-
K_Q	dimensionless torque	-
K_T	dimensionless thrust	-
L_{oa}	length overall	m
L_{pp}	length between perpendicular	m
L_{wl}	waterline length	m
L_E	length of entrance	m
L_M	model length	m
L_R	length of run	m
lcb	longitudinal center of buoancy	%
n	rate of revolution	rpm
n_{SMCR}	rate of revolution at SMCR	rpm
P_B	brake power	kW
P_0	power in calm water	kW
P_D	delivered power	kW
P_E	effective power	kW
P_s	power in rough seas	kW
P_T	thrust power	kW
P_w	power in waves	kW
P/D	pitch ratio	-
Q	torque	kN
R_{app}	resistance of appendages	kN
R_{aw}	wave-added resistance in regular seas	kN
R_{awm}	added resistance due to motions	kN
R_{awr}	added resistance due to reflection	kN
R_{tr}	additional pressure resistance of immersed transom stern	kN
R_{wind}	wind-added resistance	kN
R_a	model ship correlation resistance	kN
R_b	additional pressure resistance of bulbous bow	kN
R_c	calm water resistance	kN
R_f	rictional resistance	kN
R_w	wave making and breaking resistance	kN
Re	Reynolds number	-
S_w	surface watted area	mˆ2
T	draught	m

t	thrust deduction fraction	-
T_M	midship draught	m
T_r	temperature	deg
T_w	peak wave period	s
T_h	thrust	kN
V_{SMCR}	design speed at SMCR	knots
V_{wind}	wind speed	m/s
V_{WR}	relative wind speed	m/s
V_0	sustained speed in calm water	m/s
V_a	advance speed	m/s
V_F	full scale speed	m/s
V_k	effective wake velocity	m/s
V_M	model speed	m/s
V_w	sustained speed in rough sea	m/s
w	wake fraction	-
Z	number of blades	-

Table 5.3: List of units

Unit symbol	**Name**
deg	degree
kn	knots
m	meter
N	newton
nmi	nautical mile
rad	radian
s	second
W	watt

Bibliography

[Abbasov et al., 2022] Abbasov, F., Ambel, C. C., Earl, T., Buffet, L., Decock, G., and Marahrens, M. (2022). Fueleu maritime: Transport and environment analysis and recommendations how to drive the uptake of sustainable fuels in european shipping. Technical report, Transport and Environment.

[Adland et al., 2020] Adland, R., Cariou, P., and Wolff, F.-C. (2020). Optimal ship speed and the cubic law revisited: Empirical evidence from an oil tanker fleet. *Transportation Research Part E: Logistics and Transportation Review*, 140:101972.

[Alexandersson, 2009] Alexandersson, M. (2009). A study of methods to predict added resistance in waves. Master's thesis, KTH Centre for Naval Architecture.

[Amini-Afshar and Bingham, 2021] Amini-Afshar, M. and Bingham, H. B. (2021). Added resistance using salvesen–tuck–faltinsen strip theory and the kochin function. *Applied Ocean Research*, 106:102481.

[Anoop et al., 2015] Anoop, T. R., Kumar, V. S., Shanas, P. R., and Johnson, G. (2015). Surface wave climatology and its variability in the north indian ocean based on era-interim reanalysis. *Journal of Atmospheric and Oceanic Technology*, 32(7):1372 – 1385.

[Bertram, 2012] Bertram, V., editor (2012). *Practical Ship Hydrodynamics*. Butterworth-Heinemann, Oxford, second edition edition.

[Bradley, 2020] Bradley, B. (2020). Decarbonisation and shipping: International maritime organization ambitions and measures. https://www.hilldickinson.com/insights/articles/decarbonisation-and-shipping-international-maritime-organization-ambitions-and.

[Bullock et al., 2020] Bullock, S., Mason, J., Broderick, J., and Larkin, A. (2020). Shipping and the paris climate agreement: a focus on committed emissions. *BMC Energy*, 2(1):5.

[Bullock et al., 2022] Bullock, S., Mason, J., and Larkin, A. (2022). The urgent case for stronger climate targets for international shipping. *Climate Policy*, 22(3):301–309.

[Carlton, 2019] Carlton, J. (2019). Chapter 12 - resistance and propulsion. In Carlton, J., editor, *Marine Propellers and Propulsion (Fourth Edition)*, pages 313–365. Butterworth-Heinemann, fourth edition edition.

[Charchalis, 2013] Charchalis, A. (2013). Designing constraints in evaluation of ship propulsion power. *Journal of KONES. Powertrain and Transport*, 20:29–34.

[Cheng et al., 2021] Cheng, L., Abraham, J., Trenberth, K., Fasullo, J., Boyer, T., Locarnini, R., Zhang, B., Yu, F., Wan, L., Chen, X., Song, X., Liu, Y., Mann, M., Franco, R., Simoncelli, S., Gouretski, V., Chen, G., Mishonov, A., Reagan, J., and Zhu, J. (2021). Upper ocean temperatures hit record high in 2020. *Advances in Atmospheric Sciences*, 38:1–8.

[Diez and Peri, 2010] Diez, M. and Peri, D. (2010). Robust optimization for ship conceptual design. *Ocean Engineering*, 37(11):966–977.

[DNV, 2022a] DNV (2022a). https://www.dnv.com/expert-story/maritime-impact/How-newbuilds-can-comply-with-IMOs-2030-CO2-reduction-targets.html.

[DNV, 2022b] DNV (2022b). EEXI - Energy Efficiency Existing Ship Index. https://www.dnv.com/maritime/insights/topics/eexi/index.html.

[Du et al., 2019] Du, Y., Meng, Q., Wang, S., and Kuang, H. (2019). Two-phase optimal solutions for ship speed and trim optimization over a voyage using voyage report data. *Transportation Research Part B: Methodological*, 122:88–114.

[Duan and Li, 2013] Duan, W. and Li, C. (2013). Estimation of added resistance for large blunt ship in waves. *Journal of Marine Science and Application*, 12(1):1–12.

[EP, 2022] EP, E.-P. (2022). Sustainable maritime fuels 'fit for 55' package: The fueleu maritime proposal. Technical report, EPRS — European Parliamentary Research Service.

[EU, 2015] EU (2015). Regulation 2015/757 of 29 April 2015 on the monitoring, reporting and verification of carbon dioxide emissions from maritime transport, and amending Directive 2009/16/EC. Technical report, European Parliament and the Council.

[European-Commission, 2022] European-Commission (2022). Reducing emissions from the shipping sector. https://ec.europa.eu/clima/eu-action/transport-emissions/reducing-emissions-shipping-sector.

[European-Council, 2022] European-Council (2022). Council agrees on the carbon border adjustment mechanism (CBAM). https://www.consilium.europa.eu/en/press/press-releases/2022/03/15/carbon-border-adjustment-mechanism-cbam-council-agrees-its-negotiating-mandate/.

[Faltinsen, 1990] Faltinsen, O. (1990). *Sea loads on ships and offshore structures*. Cambridge University Press.

[Faltinsen, 1980] Faltinsen, O. M. (1980). Prediction of resistance and propulsion of a ship in a seaway. In *Proceedings of the 13th symposium on naval hydrodynamics, Tokyo, 1980.*

[Fang et al., 2019] Fang, S., Xu, Y., Li, Z., Ding, Z., Liu, L., and Wang, H. (2019). Optimal sizing of shipboard carbon capture system for maritime greenhouse emission control. *IEEE Transactions on Industry Applications*.

[Fanjul et al., 2022] Fanjul, E. A., Ciliberti, S., and Bahurel, P. (2022). Implementing operational ocean monitoring and forecasting systems. Technical report, GOOS, IOC-UNESCO and Mercator Ocean International.

[Feng et al., 2021] Feng, P., Liu, S., Shang, B., and Papanikolaou, A. (2021). Minimum propulsion power assessment of a vlcc to maintain the maneuverability in adverse conditions. *Journal of Marine Science and Engineering*, 9.

[Findlater, 1969] Findlater, J. (1969). A major low-level air current near the indian ocean during the northern summer. *Quarterly Journal of the Royal Meteorological Society*, 95(404):362–380.

[Forum, 2021] Forum, G. M. (2021). The next wave green corridors. Technical report, Global Maritime Forum.

[Friedlingstein et al., 2022] Friedlingstein, P., Jones, M. W., O'Sullivan, M., Andrew, R. M., Bakker, D. C. E., Hauck, J., Le Quéré, C., Peters, G. P., Peters, W., Pongratz, J., Sitch, S., Canadell, J. G., Ciais, P., Jackson, R. B., Alin, S. R., Anthoni, P., Bates, N. R., Becker, M., Bellouin, N., Bopp, L., Chau, T. T. T., Chevallier, F., Chini, L. P., Cronin, M., Currie, K. I., Decharme, B., Djeutchouang, L. M., Dou, X., Evans, W., Feely, R. A., Feng, L., Gasser, T., Gilfillan, D., Gkritzalis, T., Grassi, G., Gregor, L., Gruber, N., Gürses, O., Harris, I., Houghton, R. A., Hurtt, G. C., Iida, Y., Ilyina, T., Luijkx, I. T., Jain, A., Jones, S. D., Kato, E., Kennedy, D., Klein Goldewijk, K., Knauer, J., Korsbakken, J. I., Körtzinger, A., Landschützer, P., Lauvset, S. K., Lefèvre, N., Lienert, S., Liu, J., Marland, G., McGuire, P. C., Melton, J. R., Munro, D. R., Nabel, J. E. M. S., Nakaoka, S.-I., Niwa, Y., Ono, T., Pierrot, D., Poulter, B., Rehder, G., Resplandy, L., Robertson, E., Rödenbeck, C., Rosan, T. M., Schwinger, J., Schwingshackl, C., Séférian, R., Sutton, A. J., Sweeney, C., Tanhua, T., Tans, P. P., Tian, H., Tilbrook, B., Tubiello, F., van der Werf, G. R., Vuichard, N., Wada, C., Wanninkhof, R., Watson, A. J., Willis, D., Wiltshire, A. J., Yuan, W., Yue, C., Yue, X., Zaehle, S., and Zeng, J. (2022). Global carbon budget 2021. *Earth System Science Data*, 14(4):1917–2005.

[Fujii and Takahashi, 1975] Fujii, H. and Takahashi, T. (1975). Experimental Study on the Resistance Increase of a Large Full Ship in Regular Oblique Waves. *Journal of the Society of Naval Architects of Japan*, 1975(137):132–137.

[Fujiwara et al., 2005] Fujiwara, T., Ueno, M., and Ikeda, Y. (2005). A new estimation method of wind forces and moments acting on ships on the basis of physical component models. *Journal of the Japan Society of Naval Architects and Ocean Engineers*, 2:243–255.

[Gerritsma and Beukelman, 1972] Gerritsma, J. and Beukelman, W. (1972). Analysis of the resistance increase in waves of a fast cargo ship. *International Shipbuilding Progress*, 19(217):285–293.

[Gilbert et al., 2018] Gilbert, P., Walsh, C., Traut, M., Kesieme, U., Pazouki, K., and Murphy, A. (2018). Assessment of full life-cycle air emissions of alternative shipping fuels. *Journal of Cleaner Production*, 172:855–866.

[GloMEEP, 2020] GloMEEP, P. C. U. (2020). Just in time arrival guide barriers and potential solutions. Technical report, International Maritime Organization IMO.

[Grifoll et al., 2022] Grifoll, M., Borén, C., and Castells-Sanabra, M. (2022). A comprehensive ship weather routing system using cmems products and A* algorithm. *Ocean Engineering*, 255:111427.

[Guldhammer and Harvald, 1974] Guldhammer and Harvald (1974). Ship resistance - effect of form and principal dimensions. Technical report, Akademisk Forlag, Copenhagen.

[GUO and STEEN, 2011] GUO, B. and STEEN, S. (2011). Evaluation of added resistance of kvlcc2 in short waves. *Journal of Hydrodynamics, Ser. B*, 23(6):709–722.

[Hagiwara, 1989] Hagiwara, H. (1989). Weather routing of (sail-assisted) motor vessels. *PhD Thesis, Technical University of Delft.*

[Hans-O. Pörtner, 2022] Hans-O. Pörtner, D. C. R. (2022). Climate change 2022: Impacts, adaptation and vulnerability, summary for policymakers. Technical report, IPCC. www.ipcc.com.

[Hanssen and James, 1960] Hanssen, G. L. and James, R. W. (1960). Optimum ship routing. *The Journal of Navigation*, 13(3):253–272.

[Healy, 2020] Healy, S. (2020). Greenhouse gas emissions from shipping: waiting for concrete progress at imo level. Technical report, Oeko-Institut.

[Heller, 2012] Heller, V. (2012). 8.04 - development of wave devices from initial conception to commercial demonstration. In Sayigh, A., editor, *Comprehensive Renewable Energy*, pages 79–110. Elsevier, Oxford.

[Hirota et al., 2005] Hirota, K., Matsumoto, K., Takagishi, K., Yamasaki, K., Orihara, H., and Yoshida, H. (2005). Development of bow shape to reduce the added resistance due to waves and verification on full scale measurement. In *Proceedings of the International Conference on Marine Research and Transportation, Ischia, Italy*, pages 19–21.

[Hoegh-Guldberg et al., 2019] Hoegh-Guldberg, O., Caldeira, K., Chopin, T., Gaines, S., Haugan, P., Hemer, M., Howard, J., Konar, M., Krause-Jensen, D., Lindstad, E., Lovelock, C., Michelin, M., Nielsen, F., Northrop, E., Parker, R., Roy, J., Smith, T., Some, S., and

Tyedmers, P. (2019). *The Ocean as a Solution to Climate Change: Five Opportunities for Action*. World Resources Institute.

[Holt and Nielsen, 2021] Holt, P. and Nielsen, U. D. (2021). Preliminary assessment of increased main engine load as a consequence of added wave resistance in the light of minimum propulsion power. *Applied Ocean Research*, 108:102543.

[Holtrop, 1977] Holtrop, I. (1977). A statistical analysis of performance test results. *Netherlands Ship Model Basin, NSMB, Wageningen, Publication No. 540, Published in: International Shipbuilding Progress, ISP, Volume 24, Number 270, February 1977.*

[Holtrop, 1984] Holtrop, J. (1984). A statistical re-analysis of resistance and propulsion data. *International shipbuilding progress*, 31:272–276.

[Holtrop and Mennen, 1982] Holtrop, J. and Mennen, G. (1982). An approximate power prediction method. *International Shipbuilding Progress*, 29(335):166–170.

[Hwang, 2013] Hwang (2013). Experimental study on the effect of bow hull forms to added resistance in regular head waves. *PRADS2013*, 1(1):39–44.

[Hwang et al., 2020] Hwang, S., Gil, S., Lee, G., Lee, J., Park, H., Jung, K., and Suh, S. (2020). Life cycle assessment of alternative ship fuels for coastal ferry operating in republic of korea. *Journal of Marine Science and Engineering*, 8:660.

[ICCT, 2021] ICCT (2021). Zero-emission shipping and the paris agreement: Why the imo needs to pick a zero date and set interim targets in its revised ghg strategy. https://theicct.org/zero-emission-shipping-and-the-paris-agreement-why-the-imo-needs-to-pick-a-zero-date-and-set-interim-targets-in-its-revised-ghg-strategy/.

[IISD, 2020] IISD (2020). Imo advances measures to reduce emissions from international shipping. https://sdg.iisd.org/news/imo-advances-measures-to-reduce-emissions-from-international-shipping/.

[IMO, 2009] IMO (2009). MEPC.1/circ.684 guidelines for voluntary use of the ship Energy Efficiency Operational Indicator (EEOI). Technical report, International Maritime Organization, London, UK.

[IMO, 2012] IMO (2012). Resolution mepc.213(63) 2012 guidelines for the development of a ship energy efficiency management plan (seemp). Imo doc mepc 63/23 annex 9, IMO, London, UK.

[IMO, 2016] IMO (2016). MEPC.278(70) Amendments to MARPOL Annex VI (Data collection system for fuel oil consumption of ships). Technical report, International Maritime Organization, London, UK.

[IMO, 2018] IMO (2018). MEPC.304(72) Initial IMO strategy on reduction of GHG emissions from ships. Technical Report Annex 11, International Maritime Organization, London, UK.

[IMO, 2020a] IMO (2020a). MEPC 75/7/15 (Annex 2) "Fourth IMO GHG Study 2020". Technical report, International Maritime Organization.

[IMO, 2020b] IMO (2020b). MEPC 75/WP1/Rev.1 Draft Report Of The Marine Environment Protection Committee On Its Seventy-Fifth Session . Technical report, International Maritime Organization, London, UK.

[IMO, 2021] IMO (2021). Imo moves ahead on ghg emissions, black carbon and marine litter. https://www.imo.org/en/MediaCentre/PressBriefings/pages/MEPC77.aspx.

[IMO, 2022] IMO (2022). Marine environment protection committee (mepc 76), 10 to 17 june 2021 (remote session). https://www.imo.org/en/MediaCentre/MeetingSummaries/Pages/MEPC76meetingsummary.aspx.

[IPCC, 2018] IPCC (2018). Global warming of 1.5 °c an ipcc special report on the impacts of global warming of 1.5 °c above pre-industrial levels and related global greenhouse gas emission pathways, in the context of strengthening the global response to the threat of climate change, sustainable development, and efforts to eradicate poverty. Technical report, IPCC. www.ipcc.com.

[IPCC, 2022a] IPCC (2022a). Climate change 2022 mitigation of climate change summary for policymakers. working group iii. Technical report, IPCC. www.ipcc.com.

[IPCC, 2022b] IPCC (2022b). Ipcc press release. www.ipcc.ch.

[IPCC, 2022c] IPCC (2022c). Keynote address by the ipcc chair hoesung lee at the opening of the first technical dialogue of the global stocktake. https://www.ipcc.ch/2022/06/10/keynote-address-hoesung-lee-technical-dialogue-global-stocktake/.

[IPCC, 2022d] IPCC (2022d). Sixth assessment report. Working Group III. Chapter 10. Technical report, IPCC. www.ipcc.com.

[ISO, 2015] ISO (2015). Marine Technology—Guidelines for the Assessment of Speed and Power Performance by Analysis of Speed Trial Data; ISO15016. *International Organization for Standardization (ISO): Geneva, Switzerland.*

[(ISO), 1998] (ISO), I. S. O. (1998). Iso 14041: Environmental management-life cycle assessment-goal and scope definition and inventory analysis. Technical report, International Standard Organization (ISO), London, UK.

[ITTC, 1957] ITTC (1957). *Subjects 2 and 4 Skin Friction and Turbulence Stimulation.* ITTC.

[ITTC, 2011a] ITTC (2011a). *Practical guidelines for ship CFD applications*. Recommended Procedures and Guidelines 7.5-03-02-03 Revision 01.

[ITTC, 2011b] ITTC (2011b). Prediction of power increase in irregular waves from model test. Technical report, International Towing Tank Conference.

[ITTC, 2014] ITTC (2014). *Prediction of Power Increase in Irregular Waves from Model Test*. Recommended Procedures and Guidelines 7.5-02-07-02.2 Revision 05.

[ITTC, 2017a] ITTC (2017a). Calculation of the weather factor fw for decrease of ship speed in waves. Technical report, International Towing Tank Conference, 7.5-02-07-02.8.

[ITTC, 2017b] ITTC (2017b). *Calculation of the weather factor fw for decrease of ship speed in waves*. Recommended Procedures and Guidelines 7.5-02-07-02.8 Revision 00.

[ITTC, 2017c] ITTC (2017c). *Preparation, conduct and analysis of Speed/Power Trials*. Recommended Procedures and Guidelines 7.5-04-01-01.1 Revision 05.

[ITTC, 2017d] ITTC (2017d). *Resistance test*. Recommended Procedures and Guidelines 7.5-02-02-01 Revision 04.

[ITTC, 2017e] ITTC (2017e). *Seakeeping Experiments, Recommended Procedures and Guidelines 7.5-04-01-01.2*. Revision 06.

[Jalkanen et al., 2012] Jalkanen, J.-P., Johansson, L., Kukkonen, J., Brink, A., Kalli, J., and Stipa, T. (2012). Extension of an assessment model of ship traffic exhaust emissions for particulate matter and carbon monoxide. *Atmospheric Chemistry and Physics*, 12(5):2641–2659.

[James, 1957] James, R. W. (1957). *Application of wave forecasts to marine navigation*. New York University.

[Jaouen et al., 2011] Jaouen, F., Koop, A., Vaz, G., and Crepier, P. (2011). Rans predictions of roll viscous damping of ship hull sections. In *A: . CIMNE, 2011, p. 76-93.*

[Jimenez et al., 2022] Jimenez, V. J., Kim, H., and Munim, Z. H. (2022). A review of ship energy efficiency research and directions towards emission reduction in the maritime industry. *Journal of Cleaner Production*, 366:132888.

[Jinkine and Ferdinande, 1974] Jinkine, V. and Ferdinande, V. (1974). A method for predicting the added resistance of fast cargo ships in head waves. *International Shipbuilding Progress*, 21:149–167.

[Johansson et al., 2017] Johansson, L., Jalkanen, J.-P., and Kukkonen, J. (2017). Global assessment of shipping emissions in 2015 on a high spatial and temporal resolution. *Atmospheric Environment*, 167:403–415.

[JSTRA, 2020] JSTRA (2020). Roadmap to zero emission from international shipping. Technical report, Japan Ship Research Association (JSTRA).

[Kashiwagi, 2013] Kashiwagi, M. (2013). Hydrodynamic Study on Added Resistance Using Unsteady Wave Analysis. *Journal of Ship Research*, 57(04):220–240.

[Kim and Roh, 2020] Kim, K.-S. and Roh, M.-I. (2020). Iso 15016:2015-based method for estimating the fuel oil consumption of a ship. *Journal of Marine Science and Engineering*, 8(10).

[Koza et al., 1996] Koza, J. R., Bennett, F. H., Andre, D., and Keane, M. A. (1996). *Automated Design of Both the Topology and Sizing of Analog Electrical Circuits Using Genetic Programming*, pages 151–170. Springer Netherlands, Dordrecht.

[Kristensen and Bingham, 2017] Kristensen and Bingham (2017). *Prediction of Resistance and Propulsion Power of Ships*. Technical University of Denmark.

[Kuroda et al., 2012] Kuroda, M., Tsujimoto, M., Sasaki, N., Ohmatsu, S., and Takagi, K. (2012). Study on the bow shapes above the waterline in view of the powering and greenhouse gas emissions in actual seas. *Proceedings of the Institution of Mechanical Engineers, Part M: Journal of Engineering for the Maritime Environment*, 226(1):23–35.

[Lackenby, 1962] Lackenby, H. (1962). The thirty-fourth thomas lowe gray lecture: Resistance of ships, with special reference to skin friction and hull surface condition. *Proceedings of the Institution of Mechanical Engineers*, 176(1):981–1014.

[Landrini, 2001] Landrini, M. (2001). Lotto a - revisione critica dello stato dell'arte. Technical report, INSEAN.

[Lang and Mao, 2020] Lang, X. and Mao, W. (2020). A semi-empirical model for ship speed loss prediction at head sea and its validation by full-scale measurements. *Ocean Engineering*, 209:107494.

[Lang and Mao, 2021] Lang, X. and Mao, W. (2021). A Practical Speed Loss Prediction Model at Arbitrary Wave Heading for Ship Voyage Optimization. *Journal of Marine Science and Application*, 20(3):410–425.

[Lee et al., 2019] Lee, C.-M., Seo, J.-H., Yu, J.-W., Choi, J.-E., and Lee, I. (2019). Comparative study of prediction methods of power increase and propulsive performances in regular head short waves of kvlcc2 using cfd. *International Journal of Naval Architecture and Ocean Engineering*, 11(2):883–898.

[Lewis, 1988] Lewis, E. V. (1988). Principles of naval architecture second revision. *Jersey: SNAME*, 2.

[Lin et al., 2013] Lin, Y.-H., Fang, M.-C., and Yeung, R. W. (2013). The optimization of ship weather-routing algorithm based on the composite influence of multi-dynamic elements. *Applied Ocean Research*, 43:184–194.

[Lindstad, 2013] Lindstad, H. (2013). *Strategies and Measures for Reducing Maritime CO2 Emissions*. PhD thesis, NTNU.

[Liu and Papanikolaou, 2016a] Liu, S. and Papanikolaou, A. (2016a). Fast approach to the estimation of the added resistance of ships in head waves. *Ocean Engineering*, 112:211–225.

[Liu and Papanikolaou, 2016b] Liu, S. and Papanikolaou, A. (2016b). On the prediction of the added resistance of large ships in representative seaways. *Ships and Offshore Structures*, 12(5):690–696.

[Liu and Papanikolaou, 2020] Liu, S. and Papanikolaou, A. (2020). Prediction of the side drift force of full ships advancing in waves at low speeds. *Marine Science*.

[Liu et al., 2015] Liu, S., Papanikolaou, A., and Zaraphonitis, G. (2015). Practical approach to the added resistance of a ship in short waves. In *Proceedings of the Twenty-fifth (2015) International Ocean and Polar Engineering Conference Kona, Big Island, Hawaii, USA, June 21-26, 2015*.

[Lloyd, 1998] Lloyd, A. R. (1998). Seakeeping: Ship behaviour in rough weather. In *Seakeeping: Ship Behaviour in Rough Weather*.

[LR, 2022a] LR (2022a). Lloyd's register and partners unveil 'silk alliance' green corridor project. https://www.lr.org/en/latest-news/silk-alliance-green-corridor/.

[LR and UMAS, 2019] LR and UMAS (2019). "zero-emission vessels transition pathways.". Technical report, Lloyd's Register and University Maritime Advisory Services.

[LR, 2022b] LR, L. R. (2022b). First movers in shipping's decarbonisation.a framework for getting started. Technical report, The Lloyd's Register Maritime Decarbonisation Hub.

[LR, 2022c] LR, L. R. (2022c). Zero carbon fuel monitor. Technical report, The Lloyd's Register Maritime Decarbonisation Hub.

[Mallouppas and Yfantis, 2021] Mallouppas, G. and Yfantis, E. A. (2021). Decarbonization in shipping industry: A review of research, technology development, and innovation proposals. *Journal of Marine Science and Engineering*, 9(4).

[MAN, 2011] MAN (2011). Basic principles of ship propulsion. Technical report, MAN Energy Solutions.

[MAN, 2018] MAN (2018). Basic principles of ship propulsion. Technical report, MAN Energy Solutions.

[Mannarini and Carelli, 2019a] Mannarini, G. and Carelli, L. (2019). VISIR-1.b: ocean surface gravity waves and currents for energy-efficient navigation. *Geoscientific Model Development*, 12(8):3449–3480.

[Mannarini et al., 2021] Mannarini, G., Carelli, L., Orović, J., Martinkus, C. P., and Coppini, G. (2021). Towards least-co2 ferry routes in the adriatic sea. *Journal of Marine Science and Engineering*, 9(2).

[Mannarini et al., 2019b] Mannarini, G., Carelli, L., Zissis, D., Spiliopoulos, G., and Chatzikokolakis, K. (2019a). Preliminary inter-comparison of AIS data and optimal ship tracks. *TransNav*, 13(1):53–61.

[Mannarini et al., 2015] Mannarini, G., Lecci, R., and Coppini, G. (2015). Introducing sailboats into ship routing system visir. In *2015 6th International Conference on Information, Intelligence, Systems and Applications (IISA)*, pages 1–6. IEEE.

[Mannarini et al., 2016] Mannarini, G., Pinardi, N., Coppini, G., Oddo, P., and Iafrati, A. (2016). VISIR-I: small vessels – least-time nautical routes using wave forecasts. *Geoscientific Model Development*, 9(4):1597–1625.

[Mannarini et al., 2019c] Mannarini, G., Subramani, D., Lermusiaux, P., and Pinardi, N. (2019b). Graph-Search and Differential Equations for Time-Optimal Vessel Route Planning in Dynamic Ocean Waves. *IEEE Transactions on Intelligent Transportation Systems*, 21(8):3581–3593,.

[Maruo, 1960] Maruo, H. (1960). On the increase of the resistance of a ship in rough seas. *Journal of Zosen Kiokai*, 1960(108):5–13.

[Mermaid, 2022] Mermaid (2022). Ship resistance calculation. https://www.mermaid-consultants.com/ship-resistance-calculation.html.

[Mittendorf et al., 2022] Mittendorf, M., Nielsen, U. D., Bingham, H. B., and Liu, S. (2022). Towards the uncertainty quantification of semi-empirical formulas applied to the added resistance of ships in waves of arbitrary heading. *Ocean Engineering*, 251:111040.

[Moctar et al., 2012] Moctar, O., Shigunov, V., and Zorn, T. (2012). Duisburg test case: Post-panamax container ship for benchmarking. *Ship Technology Research*, 59:50–64.

[Molland, 2008] Molland, A. F. (2008). Chapter 1 - the marine environment. In Molland, A. F., editor, *The Maritime Engineering Reference Book*, pages 1–42. Butterworth-Heinemann, Oxford.

[Molland et al., 2011] Molland, A. F., Turnock, S. R., and Hudson, D. A. (2011). *Ship Resistance and Propulsion: Practical Estimation of Ship Propulsive Power*. Cambridge University Press, Cambridge, 2 edition.

[Nakamura, 1975] Nakamura, N. (1975). Propulsive performance of a container ship in waves. *Osaka University, Reprinted from: Royal Architecture and Ocean Engineering, Volume 15, Published by: The Society of Naval Architects of Japan.*

[Newman, 1977] Newman, J. N. (1977). *Marine Hydrodynamics*. The MIT Press.

[NOAA, 2022] NOAA (2022). Climate change: Atmospheric carbon dioxide. https://www.climate.gov/news-features/understanding-climate/climate-change-atmospheric-carbon-dioxide.

[Park et al., 2016] Park, D.-M., Kim, Y., Seo, M.-G., and Lee, J. (2016). Study on added resistance of a tanker in head waves at different drafts. *Ocean Engineering*, 111:569–581.

[Park et al., 2015] Park, D.-M., Lee, J., and Kim, Y. (2015). Uncertainty analysis for added resistance experiment of kvlcc2 ship. *Ocean Engineering*, 95:143–156.

[Park et al., 2019] Park, D.-M., Lee, J.-H., Jung, Y.-W., Lee, J., Kim, Y., and Gerhardt, F. (2019). Experimental and numerical studies on added resistance of ship in oblique sea conditions. *Ocean Engineering*, 186:106070.

[Psaraftis, 2019] Psaraftis, H. N. (2019). Speed optimization vs speed reduction: the choice between speed limits and a bunker levy. *Sustainability*, 11(8).

[Rakke, 2016] Rakke, S. G. (2016). Ship emissions calculation from ais. In *Ship emissions calculation from AIS*.

[Sadat-Hosseini et al., 2015] Sadat-Hosseini, H., Toxopeus, S., Kim, D.-H., Castiglione, T., sanada, Y., Stocker, M., Simonsen, C., Otzen, J., Toda, Y., and Stern, F. (2015). Experiments and computations for kcs added resistance for variable heading. In *Experiments and Computations for KCS Added Resistance for Variable Heading*.

[Sadat-Hosseini et al., 2013] Sadat-Hosseini, H., Wu, P.-C., Carrica, P. M., Kim, H., Toda, Y., and Stern, F. (2013). Cfd verification and validation of added resistance and motions of kvlcc2 with fixed and free surge in short and long head waves. *Ocean Engineering*, 59:240–273.

[Salvesen et al., 1970] Salvesen, N., Tuck, E. O., and Faltinsen, O. M. (1970). Ship motions and sea load. In *Ship motions and sea load*.

[Seo et al., 2014] Seo, M.-G., Yang, K.-K., Park, D.-M., and Kim, Y. (2014). Numerical analysis of added resistance on ships in short waves. *Ocean Engineering*, 87:97–110.

[Serra and Fancello, 2020] Serra, P. and Fancello, G. (2020). Towards the imo's ghg goals: A critical overview of the perspectives and challenges of the main options for decarbonizing international shipping. *Sustainability*, 12(8).

[Shao et al., 2012] Shao, W., Zhou, P., and Thong, S. K. (2012). Development of a novel forward dynamic programming method for weather routing. *Journal of Marine Science and Technology*, 17(2):239–251.

[Shigunov, 2013] Shigunov, V. (2013). 2013 interim guidelines for determing minimum propulsion power to maintain the manoeuvrability of ships in adverse conditions. Technical report, IMO.

[Sigmund and el Moctar, 2018] Sigmund, S. and el Moctar, O. (2018). Numerical and experimental investigation of added resistance of different ship types in short and long waves. *Ocean Engineering*, 147:51–67.

[Simonsen et al., 2013] Simonsen, C. D., Otzen, J. F., Joncquez, S., and Stern, F. (2013). Efd and cfd for kcs heaving and pitching in regular head waves. *Journal of Marine Science and Technology*, 18(4):435–459.

[Smith, 2019] Smith, T. (2019). Definition of zero carbon energy sources. Technical report, UCL Energy Institute.

[Söding and Shigunov, 2015] Söding, H. and Shigunov, V. (2015). Added resistance of ships in waves†. *Ship Technology Research*, 62(1):2–13.

[Sprenger et al., 2016] Sprenger, F., Hassani, V., Maron, A., Delefortrie, G., Van Zwijnsvoorde, T., Cura-Hochbaum, A., and Lengwinat, A. (2016). Establishment of a validation and benchmark database for the assessment of ship operation in adverse conditions. In *Establishment of a Validation and Benchmark Database for the Assessment of Ship Operation in Adverse Conditions*.

[Sprenger et al., 2017] Sprenger, F., Maron, A., Delefortrie, G., van Zwijnsvoorde, T., Cura-Hochbaum, A., Lengwinat, A., and Papanikolaou, A. (2017). Experimental Studies on Seakeeping and Maneuverability of Ships in Adverse Weather Conditions. *Journal of Ship Research*, 61(03):131–152.

[Steen, 2014] Steen, S. (2014). *Experimental Methods in Marine Hydrodynamics*. Marine technology centre Trondheim.

[Stewart, 2008] Stewart, R. H. (2008). *Introduction to physical oceanography*. Robert H. Stewart.

[Ström-Tejsen et al., 1973] Ström-Tejsen, J., Hugh, Y., and Moran, D. (1973). Added resistance in waves. In *Society of Naval Architects and Marine Engineers, Transactions*, volume 81, pages 109–143.

[Strom-Tejsen et al., 1973] Strom-Tejsen, J., Yeh, H., Moran, D., of Naval Architects, S., and Meeting, M. E. U. (1973). *Added Resistance in Waves*. Paper (Society of Naval Architects and Marine Engineers). Society of Naval Architects and Marine Engineers.

[Szlapczynska and Smierzchalski, 2007] Szlapczynska, J. and Smierzchalski, R. (2007). Adopted isochrone method improving ship safety in weather routing with evolutionary approach. *International Journal of Reliability, Quality and Safety Engineering*, 14(06):635–645.

[Tanaka, 2018] Tanaka, Y. (2018). Active vibration compensator on moving vessel by hydraulic parallel mechanism. *International Journal of Hydromechatronics*, 1:350.

[Taskar and Andersen, 2020] Taskar, B. and Andersen, P. (2020). Benefit of speed reduction for ships in different weather conditions. *Transportation Research Part D: Transport and Environment*, 85:102337.

[Terziev et al., 2022] Terziev, M., Tezdogan, T., and Incecik, A. (2022). Scale effects and full-scale ship hydrodynamics: A review. *Ocean Engineering*, 245:110496.

[Tsujimoto et al., 2008] Tsujimoto, M., Shibata, K., Kuroda, M., and Takagi, K. (2008). A Practical Correction Method for Added Resistance in Waves. *Journal of the Japan Society of Naval Architects and Ocean Engineers*, 8:177–184.

[UMAS, 2022] UMAS (2022). With decisive and strategic action, south africa can become africa's first zero-carbon bunkering hub. https://www.u-mas.co.uk/with-decisive-and-strategic-action-south-africa-can-become-africas-first-zero-carbon-bunkering-hub/.

[UN, 2022] UN, U. N. (2022). Causes and effects of climate change. https://www.un.org/en/climatechange/science/causes-effects-climate-change.

[UNCTAD, 2019] UNCTAD (2019). Review of maritime transport. Technical report, United Nations Conference On Trade And Development (UNCTAD).

[UNCTAD, 2021] UNCTAD (2021). Review of maritime transport 2021. Technical report, UNITED NATIONS CONFERENCE ON TRADE AND DEVELOPMENT.

[UNFCCC, 2015] UNFCCC (2015). Decision 1/cp.21 adoption of the paris agreement. https://unfccc.int/resource/docs/2015/cop21/eng/10a01.pdf.

[Ursell, 1947] Ursell, F. (1947). The effect of a fixed vertical barrier on surface waves in deep water. *Mathematical Proceedings of the Cambridge Philosophical Society*, 43(3):374–382.

[USNA, 2020] USNA (2020). Resistance and powering of ships. www.usna.edu.

[Valanto and Hong, 2015] Valanto, P. and Hong, Y. (2015). Experimental investigation on ship wave added resistance in regular head, oblique, beam, and following waves. *Proceedings of the Twenty-fifth (2015) International Ocean and Polar Engineering Conference Kona, Big Island, Hawaii, USA, June 21-26, 2015.*

[von Schuckmann et al., 2021] von Schuckmann, K., Traon, P.-Y. L., (Chair), N. S., Pascual, A., Djavidnia, S., Gattuso, J.-P., Grégoire, M., Aaboe, S., Alari, V., Alexander, B. E., Alonso-Martirena, A., Aydogdu, A., Azzopardi, J., Bajo, M., Barbariol, F., Batistić, M., Behrens, A., Ismail, S. B., Benetazzo, A., Bitetto, I., Borghini, M., Bray, L., Capet, A., Carlucci, R., Chatterjee, S., Chiggiato, J., Ciliberti, S., Cipriano, G., Clementi, E., Cochrane, P., Cossarini, G., D'Andrea, L., Davison, S., Down, E., Drago, A., Druon, J.-N., Engelhard, G., Federico, I., Garić, R., Gauci, A., Gerin, R., Geyer, G., Giesen, R., Good, S., Graham, R., Grégoire, M., Greiner, E., Gundersen, K., Hélaouët, P., Hendricks, S., Heymans, J. J., Holt, J., Hure, M., Juza, M., Kassis, D., Kellett, P., Knol-Kauffman, M., Kountouris, P., Kõuts, M., Lagemaa, P., Lavergne, T., Legeais, J.-F., Traon, P.-Y. L., Libralato, S., Lien, V. S., Lima, L., Lind, S., Liu, Y., Macías, D., Maljutenko, I., Mangin, A., Männik, A., Marinova, V., Martellucci, R., Masnadi, F., Mauri, E., Mayer, M., Menna, M., Meulders, C., Møgster, J. S., Monier, M., Mork, K. A., Müller, M., Nilsen, J. E. Ø., Notarstefano, G., Oviedo, J. L., Palerme, C., Palialexis, A., Panzeri, D., Pardo, S., Peneva, E., Pezzutto, P., Pirro, A., Platt, T., Poulain, P.-M., Prieto, L., Querin, S., Rabenstein, L., Raj, R. P., Raudsepp, U., Reale, M., Renshaw, R., Ricchi, A., Ricker, R., Rikka, S., Ruiz, J., Russo, T., Sanchez, J., Santoleri, R., Sathyendranath, S., Scarcella, G., Schroeder, K., Sparnocchia, S., Spedicato, M. T., Stanev, E., Staneva, J., Stocker, A., Stoffelen, A., Teruzzi, A., Townhill, B., Uiboupin, R., Valcheva, N., Vandenbulcke, L., Vindenes, H., von Schuckmann, K., Vrgoč, N., Wakelin, S., and Zupa, W. (2021). Copernicus marine service ocean state report, issue 5. *Journal of Operational Oceanography*, 14(sup1):1–185.

[Walther et al., 2016] Walther, L., Rizvanolli, A., Wendebourg, M., and Jahn, C. (2016). Modeling and optimization algorithms in ship weather routing. *International Journal of e-Navigation and Maritime Economy*, 4:31–45.

[Wang et al., 2022] Wang, X., Zhang, R., Zhao, J., and Cao, P. (2022). Study on wave added resistance of ships in oblique waves based on panel method. *Journal of Ocean University of China*, 21(3):773–781.

[Wei and Zhou, 2012] Wei, S. and Zhou, P. (2012). Development of a 3d dynamic programming method for weather routing. *TransNav, the International Journal on Marine Navigation and Safety of Sea Transportation*, 6(1):79–85.

[Xing et al., 2020] Xing, H., Spence, S., and Chen, H. (2020). A comprehensive review on countermeasures for co2 emissions from ships. *Renewable and Sustainable Energy Reviews*, 134:110222.

[Yamamoto, 1986] Yamamoto, O. (1986). Study on an approximate calculation method of resistance increase in oblique regular waves. *Journal of the Kansai Society of Naval Architects*.

[Yang et al., 2018] Yang, K.-K., Kim, Y., and Jung, Y.-W. (2018). Enhancement of asymptotic formula for added resistance of ships in short waves. *Ocean Engineering*, 148:211–222.

[Yu et al., 2017] Yu, J.-W., Lee, C.-M., Lee, I., and Choi, J.-E. (2017). Bow hull-form optimization in waves of a 66,000 dwt bulk carrier. *International Journal of Naval Architecture and Ocean Engineering*, 9(5):499–508.

[Zheng et al., 2014] Zheng, C. W., Zhou, L., Jia, B. K., Pan, J., and Li, X. (2014). Wave characteristic analysis and wave energy resource evaluation in the china sea. *Journal of Renewable and Sustainable Energy*, 6(4):043101.

[Zheng et al., 2019] Zheng, J., Zhang, H., Yin, L., Liang, Y., Wang, B., Li, Z., Song, X., and Zhang, Y. (2019). A voyage with minimal fuel consumption for cruise ships. *Journal of Cleaner Production*, 215:144–153.

[Zis and Psaraftis, 2019] Zis, T. and Psaraftis, H. N. (2019). Operational measures to mitigate and reverse the potential modal shifts due to environmental legislation. *Maritime Policy & Management*, 46(1):117–132.

[Zis et al., 2020] Zis, T. P. V., Psaraftis, H. N., and Ding, L. (2020). Ship weather routing: A taxonomy and survey. *Ocean Engineering*, 213:107697.